LIGHT IN COMPLEX DIELECTRICS

Cover: Sunrise over Boya Lake, BC, Canada; fall of 1995
(photo taken by the author)
ISBN: 90-577-6032-0

LIGHT IN COMPLEX DIELECTRICS

ACADEMISCH PROEFSCHRIFT

ter verkrijging van de graad van doctor
aan de Universiteit van Amsterdam
op gezag van de Rector Magnificus
prof. dr. J.J.M. Franse
ten overstaan van een door het college voor promoties ingestelde
commissie, in het openbaar te verdedigen in de Aula der Universiteit
op donderdag 2 december 1999, te 13.00 uur

door

FRANK JEROEN PIETER SCHUURMANS

geboren te Eindhoven

Promotor:	Prof. Dr. A. Lagendijk
Commissie:	Prof. Dr. H.M. van Driel Prof. Dr. Ir. H.B. van Linden van den Heuvell Dr. R. Sprik Prof. Dr. J.T.M. Walraven Prof. Dr. J.P. Woerdman
Paranimfen:	Wim Koops Johan van de Ridder

Faculteit Wiskunde, Informatica, Natuurkunde en Sterrenkunde (WINS)

The work described in this thesis has been supported by the
"Stichting voor Fundamenteel Onderzoek der Materie (FOM)",
which is financially supported by the
"Nederlandse Organisatie voor Wetenschappelijk Onderzoek (NWO)"
and was carried out at the

Van der Waals-Zeeman Instituut
Universiteit van Amsterdam
Valckenierstraat 65
1018 XE Amsterdam
The Netherlands

where a limited number of copies of this thesis is available.

"If a man will begin with certainties, he shall end in doubts;
but if he will be content to begin with doubts, he shall end in certainties."

Francis Bacon; 1561-1626;
The advancement of learning, I, v, 8.

CONTENTS

CHAPTER 1

Introduction

The red-orange hues of sunrise and sunset are intimately related to clear blue skies. Both originate from scattering of sunlight off small aerosols present in the atmosphere, much smaller than the wavelength of visible light, and air molecules [1]. For these small particles, light scattering is more efficient towards the blue end of the solar spectrum. So when we look at the clear sky, mainly single-scattered blue light of the sun reaches our eyes. For the same reason, the sun appears to be yellow-orange, as while the white beam of sunlight traverses the atmosphere predominantly the blue part of its spectrum is scattered out. This effect is enhanced at sunrise and sunset, since then the path length through the atmosphere is largest, resulting in the red hues.

On a hazy day, the sun does not look orange, but whitish instead. In this case, sunlight is mostly scattered by the water droplets in the air associated with haze. These droplets are much larger than the wavelength of light, and hence diffract all colors equally well, producing the white appearance [2].

In the intermediate regime, in which the scattering particles have sizes of about the wavelength of light, unusual effects may be observed. The blue sun or moon is a rare, but beautiful example [3]. Such "bluing" only occurs when just the right size of particles, about 1 micrometer across, are in the air. Then, red light resonates inside these particles, whereas blue light does not, effectively rising the scattering efficiency by about a factor of 2 for red light [2] – just the opposite of the case of red-orange sunsets. There have been few recordings in history of the resulting blue hues of the sun and moon, one of which was after the giant eruptions of the volcano Krakatoa in 1883 [4]. Obviously, the frequency of occurrence is related to the saying "it happens only once in a blue moon".

These and many more optical peculiarities in the atmosphere are described in the book by Minnaert [5].

In all examples presented above, light scatters from randomly positioned particles, but regular structures occur in nature too. For instance, the wings of butterflies and

moths are periodically structured on length scales on the order of the wavelength of visible light [6], generating the beautiful iridescent colors known to us all. The scattering of light in such periodically organized structures is dominated by interference: only wavelengths that "fit" to the period of the structure are reflected. Especially the blue and violet colors of butterfly wings are produced by this interference mechanism, whereas the red colors originate from more mundane absorption of light.

The above described natural phenomena are manifestations of "light in complex dielectrics", the subject of this thesis. What is meant by a complex dielectric? When looking in Webster's dictionary, one finds that the first definition of the entry "complex" is "composed of interconnected parts; compound; composite" [7]. So a complex dielectric is composed of several (interconnected) dielectric media, which is indeed the case for the systems studied. In addition, in chapter 2 it is shown that both spontaneous emission and scattering of light originate from the *complex* dynamic optical polarizability, which relates the two central topics of this thesis: "modification of spontaneous emission" and "Anderson localization of light."

1.1 Modification of spontaneous emission

In recent years, so-called photonic crystals [8], structures similar to the wings of butterflies, have gained much interest. Photonic crystals are three-dimensional ordered dielectric structures with a periodic variation of the refractive index on length scales comparable to the wavelength of light. These materials feature photonic bandgaps, frequency ranges for which light cannot propagate in the crystal due to multiple Bragg reflections. Probably the most interesting asset of photonic band gap materials is their ability to modify the spontaneous emission rate of excited atoms [8]; spontaneous emission is inhibited when the embedded atom has an emission frequency in the gap. The art of tailoring spontaneous emission is expected to lead to innovations, and may find its application in the opto-electronics industry, with as a promising example the laser without threshold [9].

In this thesis, a simple, yet fundamental, problem is addressed: spontaneous emission of an atom or molecule in an otherwise homogeneous dielectric. Merely placing an atom in a dielectric already modifies its spontaneous emission rate [10]. The rate is determined by the local electro-magnetic zero-point fluctuations [11], which are altered by the atoms or molecules of the dielectric. The influence of the surrounding refractive index on the spontaneous emission rate of an impurity can be captured in so-called local-field factors [12]. More specifically, the local-field factor is defined as the ratio of the local electric field at the site of the impurity to the macroscopic electric field far away. Macroscopic derivations of the local-field

correction often imply the use of a cavity around the radiating molecule, leading to the two limiting cases of the empty-cavity and Lorentz local-field factor [13]. However, the specific choice of the cavity is subtle matter, greatly complicating the interpretation [13]; until recently it was not clear which local-field correction should apply. In chapter 3, the difference between the two cases becomes apparent by identifying substitutional and interstitial impurities, which are modeled using the Onsager-Böttcher approach [14, 15], resulting in the empty-cavity and Lorentz local-field corrections [16], respectively.

A decisive experiment on the radiative lifetime of an atom in a dielectric, with varying refractive index, would settle the discussion on which local-field correction applies to spontaneous emission. Such an experiment requires a well selected combination of radiating molecule and dielectric host, as upon variation of the refractive index the electronic wavefunctions involved in the radiating transition and the luminescence quantum efficiency should not change. In chapter 4, the selection criteria are discussed, leading to the choice of an europium complex as the radiating molecule, dissolved in a series of simple alcohols serving as the dielectric host with variable refractive index. Luminescence experiments on two Eu^{3+} complexes, $Eu(hfc)_3$ and $Eu(fod)_3$, in alcohols are presented. Unfortunately, most of the local-field effect is blurred, as with changing the refractive index also the *type* of molecules constituting the dielectric changes. This problem is overcome in chapter 5, in which measurements are presented on the radiative lifetime of $Eu(fod)_3$ dissolved in a supercritical gas as a function of pressure [17]. Here, the refractive index varies because the *density* of molecules in the dielectric varies. The type of molecule, CO_2, remains the same for all refractive indices. It is found that the empty-cavity local-field factor applies to spontaneous emission, as also predicted by the theory of chapter 3.

1.2 Anderson localization of light

Apart from ordered structures like photonic crystals, also *disordered* dielectrics with a variation of the refractive index on wavelength scale exhibit interesting optical phenomena. In such structures light is randomly scattered. The scattering strength is characterized by the mean free path, the average distance light travels between two scattering events. For example in dense fog, this distance is some tens of meters. But what happens if the mean free path becomes comparable to, or smaller than the wavelength of light? For such extremely strong scattering systems, light cannot even propagate over the distance of its own wavelength, and the phenomenon of Anderson localization [18] sets in. Anderson localization and photonic bandgaps are closely related: both inhibit propagation of light due to interfer-

ence, not absorption. In order to localize light, not only should the random scattering material have a refractive index variation on length scales comparable to the wavelength of light, but the variation must also be large.

Exploiting the high refractive index of gallium phosphide of 3.3, a strongly scattering material for visible light, macroporous GaP, is prepared. In chapter 6, both the fabrication technique using photo-assisted electrochemical etching and the optical transmission properties are reported [19]. The three-dimensional random network of GaP is completely interconnected, with pore sizes of about 150 nm, comparable to the wavelength of light in the medium. As the network is mechanically stable, the pores can be filled with liquids of different refractive indices, allowing the investigation of the importance of the refractive index contrast for strongly photonic materials. Although the mean free path is very short, less than a micron, and comparable to the wavelength, the experiments on the transmission of light through the scattering material do not reveal Anderson localization.

In chapter 7, measurements are presented on enhanced backscattering of light from the strongly scattering macroporous GaP networks, which in contrast to the transmission measurements do show features indicative of Anderson localization [20]. Enhanced backscattering originates from constructive interference of time-reversed light scattering paths in the backscattering direction [21, 22]. The result is a triangular peak, the backscatter cone, superimposed on the diffuse backscattered intensity. Normally, the top of the cone is cusped, arising from interference of very long light scattering paths. Contrary, in the Anderson localization regime these long light paths do not exist, resulting in a rounded top [23]. Such rounding of the cone is indeed observed. However, a finite scattering volume and absorption of light can also lead to a rounded cone, but these possible sources of cone rounding are shown to be negligible for porous GaP. Accordingly, the observed rounding of the top of the cone is most likely the onset of Anderson localization for visible light.

CHAPTER 2

Macroscopic dielectric response of microscopic particles

This chapter serves as a concise tutorial on the interaction of light with dielectrics. It contains the necessary theoretical aspects for describing the experiments performed. Emphasis is put on the microscopic origin of the macroscopic dielectric function; several non-standard derivations including local-field corrections are presented. An extension is made to mixtures of dielectrics, treating several effective medium theories for the average dielectric constant. Scattering of light by such mixtures is captured in the quasi-static dielectric function.

2.1 The microscopic polarizable dipole

Light is generated by the acceleration of charged particles. The interaction of light with dielectric material is therefore a subtle interplay between absorption of light and the subsequent emission of it by the atoms or molecules, *i.e.* the microscopic polarizable dipoles, that constitute the dielectric. The interaction is complicated as each dipole not only feels the external electro-magnetic field, but also the fields produced by all the other dipoles. In order to understand the full macroscopic response of a collection of microscopic polarizable dipoles, first the description of one such dipole is presented.

Note that many of the elementary ingredients used in this chapter can be found in the excellent book by J.D. Jackson [24]. Throughout this chapter Heaviside-Lorentz units are used, as discussed in table 2 in the appendix of the book by Jackson [24].

The microscopic polarizable dipole can be modeled by a damped harmonic oscillator, with mass m and charge $-e$ that oscillates around a fixed charge $+e$ [11]. It is assumed that the amplitude of oscillation is small, so that the spatial variation of the time varying electric field $\mathbf{E}(t)$ can be neglected; the dipole approximation

is employed. The equation of motion for an oscillator with displacement **x** from its equilibrium position is

$$m\left[\frac{\partial^2 \mathbf{x}}{\partial t^2}+\Gamma\frac{\partial \mathbf{x}}{\partial t}+\omega_0^2\mathbf{x}\right]=-e\mathbf{E}(t), \tag{2.1}$$

where ω_0 is the resonance frequency of the oscillator and Γ a to be determined damping rate. If the electric field varies harmonically in time with frequency ω as $\mathrm{e}^{-i\omega t}$, *i.e.* monochromatic light with frequency ω, the induced dipole moment **p** of the oscillator is

$$\mathbf{p}=-e\mathbf{x}=\frac{e^2/m}{\omega_0^2-\omega^2-i\omega\Gamma}\mathbf{E}. \tag{2.2}$$

As can be seen from Eq. 2.2, the discussion presented here is restricted to linear and isotropic dielectrics, as **p** is linear with **E**. The (linear) dynamic polarizability $\alpha(\omega)$ is defined as $\mathbf{p}\equiv\alpha(\omega)\mathbf{E}$, giving

$$\alpha(\omega)=\alpha(0)\times\frac{\omega_0^2}{\omega_0^2-\omega^2-i\omega\Gamma}, \tag{2.3}$$

where $\alpha(0)=e^2/(m\omega_0^2)$ is the static polarizability. The dynamic polarizability displays the resonant structure of an absorbing atom or molecule with resonance frequency ω_0 and line width Γ.

In an oscillating dipole the charge $-e$ is accelerated sinusoidally, hence the dipole emits radiation. As a result, the amplitude of the oscillating dipole gradually decreases, since energy of motion is converted into radiant energy. This phenomenon is called radiation damping, and is the classical analogue of spontaneous emission in which an atom makes a transition from an excited state to a state of lower energy by emission of a photon. The decrease in amplitude is grasped in the damping rate Γ. In order to conserve energy, the power taken by the dipole from the incident electric field should equal the reradiated power, *i.e.* the optical theorem [25] should hold. As a result, the set $\{\Gamma,\alpha(0),\omega_0\}$ has only two independent parameters: Γ cannot be chosen independently. The optical theorem requires

$$\Gamma=\frac{\alpha(0)\omega^2\omega_0^2}{6\pi c_0^3}, \tag{2.4}$$

where c_0 is the speed of light in vacuo. It is convenient to remove the functional dependence of Γ on ω by introducing

$$\Gamma_0\equiv\Gamma(\omega_0^2/\omega^2)=\frac{\alpha(0)\omega_0^4}{6\pi c_0^3}, \tag{2.5}$$

the spontaneous emission rate or the Einstein A coefficient. The full mapping of our results on those of Fermi's golden rule [26] from quantum mechanics can be obtained by taking for the static polarizability $\alpha(0) = 2|\mathbf{D}|^2/(\varepsilon_0\hbar\omega_0)$ [16, 25], where $\mathbf{D}$ is the dipole matrix element of two atomic levels. In fact, this treatment of an atom is equivalent to the two-level atom approach in quantum mechanics, except that the induced dipole cannot be saturated. The full frequency dependency of the dynamic polarizability is thus given by

$$\alpha(\omega) = \alpha(0) \times \frac{\omega_0^2}{\omega_0^2 - \omega^2 - i(\Gamma_0\omega^3/\omega_0^2)}. \tag{2.6}$$

As mentioned above, the oscillating dipole radiates. The field felt by a dipole inside a dielectric is a summation of all fields from the other dipoles and the incident exciting field. In order to be able to perform such a summation, one needs to know the field of one such point dipole. This field $\mathbf{E}_{\rm dip}(\mathbf{r})$ at position $\mathbf{r}$ produced by an oscillating dipole positioned at the origin is given by

$$\begin{aligned}\mathbf{E}_{\rm dip}(\mathbf{p},k,\mathbf{r}) = k^2(\mathbf{n}\times\mathbf{p})\times\mathbf{n}\frac{e^{ikr}}{4\pi r} - \frac{1}{3}\mathbf{p}\,\delta^3(\mathbf{r}) \\ + \frac{1}{4\pi}\left[3\mathbf{n}(\mathbf{n}\cdot\mathbf{p}) - \mathbf{p}\right]\left(\frac{1}{r^3} - \frac{ik}{r^2}\right)e^{ikr}.\end{aligned} \tag{2.7}$$

Here $k = \omega/c_0$ is the wavevector, $r = |\mathbf{r}|$ the distance from the dipole, and $\mathbf{n} = \mathbf{r}/r$ the unit vector pointing from the dipole towards $\mathbf{r}$. Note that when the dipole is position at $\mathbf{r}_0$, $\mathbf{r}$ should be replaced by $(\mathbf{r} - \mathbf{r}_0)$. As can be guessed from Eq. 2.7, the summation of the contributions of all the dipoles at different positions is quite cumbersome. However, this complicated form can in some limits be simplified. In the far field, or radiation zone ($kr \to \infty$), this equation reduces to

$$\mathbf{E}^{\rm ff}_{\rm dip}(\mathbf{p},k,\mathbf{r}) = k^2(\mathbf{n}\times\mathbf{p})\times\mathbf{n}\frac{e^{ikr}}{4\pi r}. \tag{2.8}$$

Whereas in the near field, or static zone ($kr \downarrow 0$), the field approaches

$$\mathbf{E}^{\rm nf}_{\rm dip}(\mathbf{p},\mathbf{r}) = \frac{1}{4\pi}\left[3\mathbf{n}(\mathbf{n}\cdot\mathbf{p}) - \mathbf{p}\right]\frac{1}{r^3} - \frac{1}{3}\mathbf{p}\,\delta^3(\mathbf{r}), \tag{2.9}$$

which is, apart from its oscillations in time, just the static electric dipole field. Equation 2.9 will be used for dense dielectrics in which the dipoles are in each others near field.

The delta function term in Eqs. 2.7 and 2.9 *only* contributes to the dipole field at the position of the point dipole. Nevertheless, the delta function is essential to

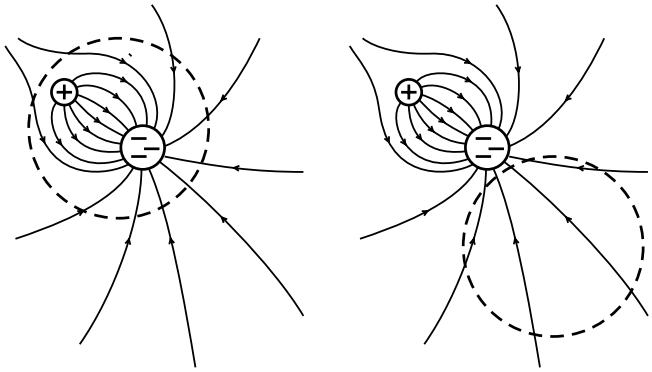

Figure 2.1 Two charge distributions: All charges are inside (left) or outside (right) the sphere within which the volume integral of the electric field is to be calculated, corresponding to Eqs. 2.10 and 2.11, respectively.

fulfill a general theorem by Maxwell: the volume integral of the static electric field over a sphere with radius R is

$$\int_{r<R} \mathbf{E}(\mathbf{r})\, d^3\mathbf{r} = -\frac{1}{3}\mathbf{p}. \tag{2.10}$$

Here $\mathbf{E}$ is the electric field produced by the charges, which are assumed to be all *inside* the sphere, and $\mathbf{p}$ the electric dipole moment of the charge distribution with respect to the center of the sphere, see Fig. 2.1. Note that this volume integral is independent of the size of the *spherical* region of integration provided that all the charge is inside. For a set of point dipoles $\{\mathbf{p}_i\}$, the total electric dipole moment with respect to the center of the sphere resides to a simple summation of all the individual dipole moments $\sum_i \mathbf{p}_i$, independent of the positional distribution of these dipoles. In fact, the delta function term in Eqs. 2.7 and 2.9 carries the essential information about the actual finite charge distribution of the dipole. The role of the delta function will be rediscussed when treating the small dielectric sphere, or point scatterer. Complementary, when all the charges are *outside* the sphere, see Fig. 2.1, the volume integral of $\mathbf{E}$ is

$$\int_{r<R} \mathbf{E}(\mathbf{r})\, d^3\mathbf{r} = \frac{4\pi}{3} R^3 \mathbf{E}(0). \tag{2.11}$$

In other words, the average value of the electric field over a spherical volume containing no charge is the value of the field at center of the sphere $\mathbf{E}(0)$. It should be stressed that Eqs. 2.10 and 2.11 only hold for static charge distributions.

2.2 Macroscopic quantities; spatial averaging

The fields introduced so far are *microscopic* electric fields produced by a microscopic charge distribution. However, for many *macroscopic* properties of dielectrics it is not essential, and actually far to complicated, to know the exact microscopic electric field. For any dielectric, except for extremely dilute gases, the number of microscopic polarizable dipoles within the optical volume $\rho\lambda^3$ is very large, where ρ is the number density of the dipoles and λ the wavelength of (visible) light. As a result, the microscopic fields produced by these dipoles vary extremely rapidly in space and time. On length scales Λ, with $\lambda \gg \Lambda \gg \rho^{-1/3}$, these microscopic fluctuations average out, giving relatively smooth and slowly varying macroscopic quantities.

To obtain such macroscopic quantities, it is necessary to perform a spatial averaging procedure. The spatial average of a microscopic quantity $S(\mathbf{r},t)$ with respect to a test function $f(\mathbf{r})$ is defined as

$$\langle S(\mathbf{r},t)\rangle = \int d^3\mathbf{r}' f(\mathbf{r}') S(\mathbf{r}-\mathbf{r}',t), \tag{2.12}$$

where $f(\mathbf{r})$ is real, nonzero in the neighborhood of $\mathbf{r}=0$, and normalized to unity over all space. The often used spherical averaging volume with radius R ($R \simeq \Lambda$) is represented by

$$f(\mathbf{r}) = \frac{3}{4\pi R^3}\Theta(R^2 - |\mathbf{r}|^2), \tag{2.13}$$

where $\Theta(x)$ is the step function, with $\Theta(x)=1$ for $x \geq 0$ and $\Theta(x)=0$ for $x<0$.

Using the spatial averaging procedure, the macroscopic electric field $\mathbf{E}_{\rm mac}(\mathbf{r},t)$ becomes

$$\mathbf{E}_{\rm mac}(\mathbf{r},t) = \langle \mathbf{E}(\mathbf{r},t)\rangle, \tag{2.14}$$

where $\mathbf{E}(\mathbf{r},t)$ is the microscopic electric field. Likewise, the macroscopic polarization $\mathbf{P}(\mathbf{r},t)$ for a set of induced point dipoles $\{\mathbf{p}_i\}$ at positions $\{\mathbf{r}_i\}$ is

$$\mathbf{P}(\mathbf{r},t) = \langle \sum_i \mathbf{p}_i \delta^3(\mathbf{r}-\mathbf{r}_i)\rangle. \tag{2.15}$$

For linear, isotropic, homogeneous dielectrics the macroscopic polarization $\mathbf{P}$ and the macroscopic electric field $\mathbf{E}_{\rm mac}$ are related through

$$\mathbf{P} = \chi(\omega)\mathbf{E}_{\rm mac} \equiv (\varepsilon(\omega)-1)\mathbf{E}_{\rm mac}, \tag{2.16}$$

where $\chi(\omega)$ is the electric susceptibility and $\varepsilon(\omega)$ the dielectric function, for $\omega=0$ known as the dielectric constant $\varepsilon(0)$. Equation 2.16 is the macroscopic analogon

of $\mathbf{p} = \alpha(\omega)\mathbf{E}$. The macroscopic response of a homogeneous dielectric is completely captured in $\chi(\omega)$, or equivalently $\varepsilon(\omega)$. This macroscopic response originates from the microscopic one: $\chi(\omega)$, $\varepsilon(\omega)$, depends on how the dipoles are spatially arranged, the density of the dipoles ρ, and their polarizability $\alpha(\omega)$.

2.3 The small dielectric sphere

In order to further clarify the properties of a point dipole, the small dielectric sphere is discussed. The two, the point dipole and the small dielectric sphere, are shown to be analogous.

Consider a small dielectric sphere with radius a and dielectric constant ε in a homogeneous external electric field $\mathbf{E}_0$. Small means that a is much smaller than the wavelength λ, so that electrostatic approach is applicable (also known as the long wavelength limit or dipole approximation). The dielectric sphere is polarized by the external electric field $\mathbf{E}_0$. As a result, the total electric field is different from the external field. The electric field $\mathbf{E}_{\text{in}}$ *inside* the dielectric is homogeneous and given by

$$\mathbf{E}_{\text{in}} = \frac{3}{\varepsilon+2}\mathbf{E}_0 \equiv \mathbf{E}_0 + \mathbf{E}_{\text{depol}}, \tag{2.17}$$

where $\mathbf{E}_{\text{depol}}$ is the depolarization field produced by the dielectric sphere. *Outside* the sphere, the total field is the sum of $\mathbf{E}_0$ and the field of an electric dipole (see Eq. 2.9) at the center of the sphere with dipole moment

$$\mathbf{p}_{\text{sph}} = 4\pi\frac{\varepsilon-1}{\varepsilon+2}a^3\mathbf{E}_0 = 3\frac{\varepsilon-1}{\varepsilon+2}\Omega\mathbf{E}_0, \tag{2.18}$$

where $\Omega = 4\pi a^3/3$ is the volume of the sphere. The dipole moment $\mathbf{p}_{\text{sph}}$ can be interpreted as the volume integral of polarization $\mathbf{P}$, as the polarization is (see Eq. 2.16),

$$\mathbf{P} = (\varepsilon-1)\mathbf{E}_{\text{in}} = 3\frac{\varepsilon-1}{\varepsilon+2}\mathbf{E}_0. \tag{2.19}$$

Combining Eqs. 2.17 and 2.18 gives for the depolarization field

$$\mathbf{E}_{\text{depol}} = -\frac{1}{3\Omega}\mathbf{p}_{\text{sph}} = -\frac{1}{3}\mathbf{P}, \tag{2.20}$$

baring close resemblance to the delta function term in Eqs. 2.7 and 2.9. In fact, in the limit $a \downarrow 0$ the dielectric sphere, or *point scatterer*, is equivalent to a point

dipole in the quasi-static regime ($\omega \ll \omega_0$). The analogy is complete when the static polarizability in Eq. 2.6 is identified as

$$\alpha(0) = 3\Omega\frac{\varepsilon - 1}{\varepsilon + 2}. \tag{2.21}$$

The dynamic polarizability $\alpha(\omega)$ also depends on ω_0 and Γ_0. The exact value for ω_0 is irrelevant, as long as $\omega_0 \gg \omega$. The damping rate Γ_0 follows from the optical theorem, as *elastic* point scatterers are considered, see Eq. 2.5. Contrary to the quasi-static regime, the analogy in the resonant regime is more complicated [27].

Particles much smaller than the wavelength of light λ are also called Rayleigh scatterers [2]. The present treatment breaks down when the size s of the scatterer becomes comparable or larger than λ. The regime $s \simeq \lambda$ is governed by Mie scattering, whereas for $s \gg \lambda$ geometrical scattering is important [2].

2.3.1 The small dielectric cavity

The properties of a small dielectric cavity with radius a inside an otherwise homogeneous dielectric with dielectric constant ε are very similar to the above described dielectric sphere. The macroscopic field outside the cavity can be represented by the sum of the macroscopic applied field $\mathbf{E}_{\text{mac}}$ and the field of a dipole placed at the center of the cavity with dipole moment

$$\mathbf{p}_{\text{cav}} = 3\varepsilon\frac{1-\varepsilon}{2\varepsilon+1}\Omega\mathbf{E}_{\text{mac}}, \tag{2.22}$$

where of course Ω is the volume of the cavity. Note that $\mathbf{p}_{\text{cav}}$ is oppositely directed to $\mathbf{E}_{\text{mac}}$ for $\varepsilon > 1$. It should also be emphasized that the field produced by $\mathbf{p}_{\text{cav}}$ is the field of a dipole in a host medium with dielectric constant ε. The electric field $\mathbf{E}_{\text{in}}$ inside the cavity is homogeneous and given by

$$\mathbf{E}_{\text{in}} = \frac{3\varepsilon}{2\varepsilon+1}\mathbf{E}_{\text{mac}} = \mathbf{E}_{\text{mac}} + \mathbf{E}_{\text{depol}} \equiv L_{\text{emp}}\mathbf{E}_{\text{mac}}. \tag{2.23}$$

Here $\mathbf{E}_{\text{depol}} = -1/(3\varepsilon\Omega)\mathbf{p}_{\text{cav}}$, similar to Eq. 2.20, and the empty cavity factor L_{emp} is defined for later convenience.

2.4 The dielectric function

As already mentioned, the dielectric function $\varepsilon(\omega)$ of a homogeneous dielectric depends on the density ρ and polarizability $\alpha(\omega)$ of the dipoles that constitute the dielectric. For simplicity it assumed that the dielectric consists of only *one* type of polarizable dipoles, with a density that is independent of position. Here several derivations for $\varepsilon(\omega)$ are presented.

2.4.1 Linear response

First the linear response approach is discussed. The dipoles are polarized by a homogeneous external field $\mathbf{E}_0$. In the approximation of the linear response model, the electric field produced by these dipoles is disregarded. As a result, the macroscopic electric field $\mathbf{E}_{\rm mac}$ equals the microscopic one: $\mathbf{E}_{\rm mac} = \mathbf{E}_0$, as $\mathbf{E}_0$ is the only microscopic field present. The macroscopic polarization $\mathbf{P}$ is given by (see Eq. 2.15)

$$\mathbf{P} = \langle \sum_i \alpha(\omega)\mathbf{E}_0\, \delta^3(\mathbf{r}-\mathbf{r}_i)\rangle = \rho\alpha(\omega)\mathbf{E}_{\rm mac}, \tag{2.24}$$

using $\mathbf{p}_i = \mathbf{p} = \alpha(\omega)\mathbf{E}_0$, $\mathbf{E}_{\rm mac} = \mathbf{E}_0$, and

$$\rho = \langle \sum_i \delta^3(\mathbf{r}-\mathbf{r}_i)\rangle. \tag{2.25}$$

Hence, combining Eqs. 2.16 and 2.24, the dielectric function is found to be

$$\varepsilon(\omega) = 1 + \rho\alpha(\omega). \tag{2.26}$$

The linear response approximation is valid for ε close to 1, or equivalently $\rho\alpha \ll 1$.

2.4.2 A random collection of dipoles; fluids

For dense dielectrics, that is $\rho\alpha(\omega) \sim 1$, the linear response approximation breaks down: the dipolar electric fields may not be neglected. In general, the total static microscopic field $\mathbf{E}_{\rm mic}(\mathbf{r})$ for a collection of dipoles $\{\mathbf{p}_i\}$ at positions $\{\mathbf{r}_i\}$ is

$$\mathbf{E}_{\rm mic}(\mathbf{r}) = \mathbf{E}_0 + \sum_i \mathbf{E}^{\rm nf}_{\rm dip}(\mathbf{p}_i, \mathbf{r}-\mathbf{r}_i), \tag{2.27}$$

where again $\mathbf{E}_0$ is the homogeneous external electric field and $\mathbf{E}^{\rm nf}_{\rm dip}$ is given by Eq. 2.9. This summation over dipolar fields consists of two contributions: the scattered fields $\mathbf{E}_{\rm scat}$ and the depolarization fields $\mathbf{E}_{\rm depol}$, explicitly given by

$$\mathbf{E}_{\rm scat} = \sum_i \frac{1}{4\pi}\left[3\mathbf{n}_i(\mathbf{n}_i\cdot\mathbf{p}_i) - \mathbf{p}_i\right]\frac{1}{r_i^3} \tag{2.28}$$

and

$$\mathbf{E}_{\rm depol} = -\sum_i \frac{1}{3}\mathbf{p}_i\, \delta^3(\mathbf{r}-\mathbf{r}_i), \tag{2.29}$$

where the notation is used as explained below Eq. 2.7. For randomly positioned dipoles, as is the case for fluids, it is *assumed* that $\mathbf{E}_{\rm scat}$ averages out to zero. Later,

this will be shown explicitly for dipoles on a square lattice. Using this assumption, the total microscopic field resides to

$$\mathbf{E}_{\rm mic}(\mathbf{r}) = \mathbf{E}_0 - \sum_i \frac{1}{3}\mathbf{p}_i \delta^3(\mathbf{r}-\mathbf{r}_i). \tag{2.30}$$

As the discussion is concerned with homogeneous and isotropic media, all dipole moments are the same, that is $\mathbf{p}_i = \mathbf{p}$. Hence, the macroscopic electric field $\mathbf{E}_{\rm mac}$, using Eqs. 2.14 and 2.25, is given by

$$\mathbf{E}_{\rm mac} = \mathbf{E}_0 - \frac{1}{3}\rho\mathbf{p}. \tag{2.31}$$

Similarly, the macroscopic polarization $\mathbf{P}$ becomes, see Eq. 2.15,

$$\mathbf{P} = \rho\mathbf{p}. \tag{2.32}$$

The only unknown parameter left, is the dipole moment $\mathbf{p}$ that is induced by the microscopic field at the position of the dipole. This field is $\mathbf{E}_0 - (1/3)\mathbf{p}\,\delta^3(0)$, where the delta function represents an unphysical self interaction and will be neglected. Here, it is implicitly assumed that two or more dipoles are not on the same position. Consequently, $\mathbf{p} = \alpha(\omega)\mathbf{E}_0$. Combining Eqs. 2.16, 2.31, and 2.32, finally the desired result for the dielectric function is obtained

$$\varepsilon(\omega) = 1 + \frac{\rho\alpha(\omega)}{1 - \frac{1}{3}\rho\alpha(\omega)}. \tag{2.33}$$

It should be noted that this derivation is done in the static limit. However, it also holds for dynamic fields, under the assumption that the size of the sphere used in the spatial averaging procedure to obtain macroscopic quantities, see Eq. 2.13, is much smaller than the wavelength involved. Furthermore, it is clear that for $\rho\alpha(\omega) \ll 1$ the linear response result, Eq. 2.26, is regained.

2.4.3 A square lattice of dipoles; exact result for electrostatics

Consider a dielectric with the dipoles $\mathbf{p}$ placed on a square lattice. The positions of the dipoles are thus given by the set of coordinates $\{\mathbf{R}\}$, with components along the cartesian coordinate axes (ai, aj, ak), where a is the lattice spacing, and i, j, and k each take on positive and negative integer values. Hence, the total static microscopic field is, see Eq. 2.27,

$$\mathbf{E}_{\rm mic}(\mathbf{r}) = \mathbf{E}_0 + \sum_{\{\mathbf{R}\}} \mathbf{E}^{\rm nf}_{\rm dip}(\mathbf{p}, \mathbf{r}-\mathbf{R}). \tag{2.34}$$

Contrary to the treatment of fluids, where the dipoles were randomly positioned, it is now not assumed that the scattered fields of the dipoles average out to zero. Here, of course within the limits of the static approximation, the derivation will be *exact* using the explicit form of Eq. 2.34.

As the lattice of point dipoles is homogeneous, the macroscopic field is also homogeneous. Therefore, it is sufficient to calculate the macroscopic field at the origin

$$\mathbf{E}_{\mathrm{mac}}(0) = \frac{3}{4\pi R^3} \int_{r<R} d^3\mathbf{r} \left[\mathbf{E}_0 + \sum_{\{\mathbf{R}\}} \mathbf{E}^{\mathrm{nf}}_{\mathrm{dip}}(\mathbf{p}, \mathbf{r} - \mathbf{R}) \right], \tag{2.35}$$

where the spherical integration volume is centered at the origin and using Eqs. 2.12-2.14 and 2.34. As the external field $\mathbf{E}_0$ is independent of position, the contribution of this field is just (as always) $\mathbf{E}_0$. The other contribution to the microscopic field in the sphere is a superposition of fields from the dipoles both *in* and *outside* the sphere. The entire set of $\{\mathbf{R}\}$ dipoles can be divided into two subsets: the dipoles in the sphere $\{\mathbf{R}_{\mathrm{in}}\}$ and the dipoles outside the sphere $\{\mathbf{R}_{\mathrm{out}}\}$: $\sum_{\{\mathbf{R}\}} = \sum_{\{\mathbf{R}_{\mathrm{in}}\}} + \sum_{\{\mathbf{R}_{\mathrm{out}}\}}$.

First consider the contribution of $\{\mathbf{R}_{\mathrm{in}}\}$ to the macroscopic field. As all the dipoles are inside the sphere, Eq. 2.10 is applicable,

$$\int_{r<R} d^3\mathbf{r} \sum_{\{\mathbf{R}_{\mathrm{in}}\}} \mathbf{E}^{\mathrm{nf}}_{\mathrm{dip}}(\mathbf{p}, \mathbf{r} - \mathbf{R}_{\mathrm{in}}) = -\frac{1}{3} \sum_{\{\mathbf{R}_{\mathrm{in}}\}} \mathbf{p}. \tag{2.36}$$

Hence, the contribution to the macroscopic field of the dipoles inside the sphere is $-(1/3)\rho\mathbf{p}$, where ρ is identified as $(3/4\pi R^3)\sum_{\{\mathbf{R}_{\mathrm{in}}\}}$.

Similarly, for the dipoles outside the sphere Eq. 2.11 applies,

$$\int_{r<R} d^3\mathbf{r} \sum_{\{\mathbf{R}_{\mathrm{out}}\}} \mathbf{E}^{\mathrm{nf}}_{\mathrm{dip}}(\mathbf{p}, \mathbf{r} - \mathbf{R}_{\mathrm{out}}) = \frac{4\pi R^3}{3} \sum_{\{\mathbf{R}_{\mathrm{out}}\}} \mathbf{E}^{\mathrm{nf}}_{\mathrm{dip}}(\mathbf{p}, 0 - \mathbf{R}_{\mathrm{out}}). \tag{2.37}$$

Instead of the volume integral, the summation over $\{\mathbf{R}_{\mathrm{out}}\}$ of the dipole fields in the origin has to be performed. It will be proven at the end of this subsection that this summation adds up to zero, so that the macroscopic field $\mathbf{E}_{\mathrm{mac}}$ is

$$\mathbf{E}_{\mathrm{mac}} = \mathbf{E}_0 - \frac{1}{3}\rho\mathbf{p}, \tag{2.38}$$

which is identical to Eq. 2.31.

The microscopic field at the position of a dipole, or equivalently at the origin $\mathbf{E}_{\mathrm{mic}}(0)$, is given by Eq. 2.34, where the field of the dipole at the origin is excluded for reasons of the unphysical self interaction,

$$\mathbf{E}_{\mathrm{mic}}(0) = \mathbf{E}_0 + \sum_{\{\mathbf{R}\neq 0\}} \mathbf{E}^{\mathrm{nf}}_{\mathrm{dip}}(\mathbf{p}, 0 - \mathbf{R}). \tag{2.39}$$

Figure 2.2 Two spherically symmetric subsets of dipoles on a cubic lattice: Left the subset $\{\mathbf{R} \neq 0\}$, right $\{\mathbf{R}_{\text{out}}\}$, corresponding to Eqs. 2.39 and 2.37, respectively. Both subsets are captured by $\{\mathbf{R}'\}$.

It is clear that this summation resembles the second summation in Eq. 2.37, the only difference is the set of dipoles over which the summation runs. As will be proven, the summation in Eq. 2.39 is also zero. As a result, the microscopic electric field at the position of a dipole is $\mathbf{E}_0$. Consequently $\mathbf{p} = \alpha(0)\mathbf{E}_0$, where $\alpha(0)$ is used as the derivation is for the static limit. Similar as in the random case, combining Eqs. 2.16, 2.32, and 2.38 gives

$$\varepsilon(0) = 1 + \frac{\rho\alpha(0)}{1 - \frac{1}{3}\rho\alpha(0)}, \tag{2.40}$$

identical to the static limit of Eq. 2.33. It should be stressed that the derivation of Eq. 2.40 is exact, whereas in the derivation for randomly positioned dipoles it had to be assumed that the scattered fields, see Eq. 2.28, average out to zero. Nevertheless, this assumption seems valid as both the random system and the square lattice are highly symmetric positional realizations, and should therefore have the same dependence of ε on ρ and α , compare Eqs. 2.33 and 2.40.

Still left to prove is that the summations in Eq. 2.37 and 2.39 of the dipole fields in the origin are zero. Considering Eq. 2.9, it is clear that the delta function terms do not contribute to the sum, since the summation either runs over all dipoles excluding a sphere of many dipoles centered around the origin [Eq. 2.37] or all dipoles excluding the one positioned at the origin [Eq. 2.39], see Fig. 2.2. As a result, the summation $\mathbf{S}$ is explicitly given by, where the prefactor $1/(4\pi)$ is left out,

$$\mathbf{S} = \sum_{\{\mathbf{R}'\}} \frac{3\mathbf{R}(\mathbf{R}\cdot\mathbf{p}) - |\mathbf{R}|^2\mathbf{p}}{|\mathbf{R}|^{5/2}}. \tag{2.41}$$

Here the prime in $\{\mathbf{R}'\}$ denotes that the summation is constraint to a spherical symmetric subset of $\{\mathbf{R}\}$ centered around the origin, covering both Eqs. 2.37 and 2.39. The x component of $\mathbf{S}$, S_1, can be written in the form

$$S_1 = \sum_{(ijk)'} \frac{3(i^2 p_1 + ijp_2 + ikp_3) - (i^2+j^2+k^2)p_1}{a^3(i^2+j^2+k^2)^{5/2}}, \tag{2.42}$$

where $\mathbf{p} = (p_1, p_2, p_3)$. Since the indices run equally over positive and negative values, even when relaxing the spherical symmetrically constraint, the cross terms involving $(ijp_2 + ikp_3)$ vanish.

Consider a specific lattice vector (s,t,u), which has a length $|(s,t,u)| = \sqrt{s^2+t^2+u^2}$, where s, t, and u can have both positive and negative integer values. This vector is part of a subset of vectors, labeled as $\{(s,t,u)\}$, which can be generated from (s,t,u) by permutation of the components s, t, and u. Thus all the vectors in $\{(s,t,u)\}$ have the same length. Note that there are different subsets with vectors of the same length, but these subsets will be treated independently. For example, a vector from $\{(-s,-t,u)\}$ has the same length as a vector from $\{(s,t,u)\}$. It is sufficient to prove that summation over the subset $\{(s,t,u)\}$ yields zero in oder to prove that the entire sum Eq. 2.42 is zero, as $\{\mathbf{R}'\}$ is a superposition of many different $\{(s,t,u)\}$.

The subset $\{(s,t,u)\}$ contains six vector (six permutations). The first component of these vectors is twice s, twice t, and also twice u. The summation over this subset thus yields, see Eq. 2.42,

$$\frac{3\cdot 2(s^2+t^2+u^2)p_1 - 6|(s,t,u)|^2 p_1}{a^3|(s,t,u)|^{5/2}} = 0. \tag{2.43}$$

This completes the prove that the summation S_1 is zero. If the summation of one component of $\mathbf{S}$, S_1, is zero, then by symmetry this also holds for the other components, and thus $\mathbf{S} = 0$.

2.4.4 A square lattice of dipoles; virtual cavity approach

In this section a more generally employed derivation of Eqs. 2.33 and 2.40 is sketched. In this approach a sphere is imagined inside the dielectric, the virtual cavity, centered at a particular dipole. The dipoles nearby the central dipole, that is the dipoles *in* the sphere with dipole moment $\mathbf{p}$, are treated individually. The dipoles *outside* the sphere are considered in the continuum approximation described by the polarization $\mathbf{P}$. By use of the superposition principle the field at the central dipole, *i.e.* the *local field* $\mathbf{E}_{\text{loc}}$, can be derived. This local field is the sum of: i) the macroscopic field $\mathbf{E}_{\text{mac}}$, with corresponding polarization $\mathbf{P}$; ii) the field $\mathbf{E}_{\text{P}}$ inside a dielectric sphere with polarization $-\mathbf{P}$; iii) the total field $\mathbf{E}_{\text{near}}$ produced by the discrete

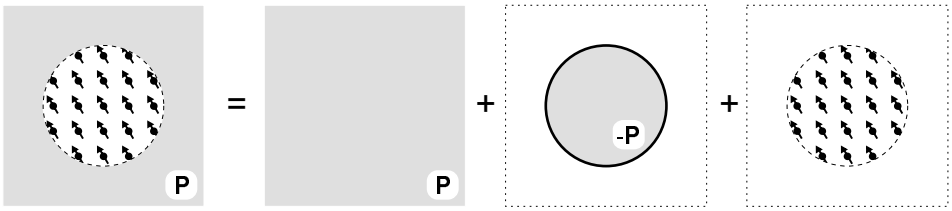

Figure 2.3 The field at the center of the virtual cavity can be found by using the superposition principle. The separation of the dielectric into an average polarization **P** outside the cavity and discrete dipoles inside is comprehended in the superposition of a homogeneous dielectric with polarization **P**, a dielectric sphere with the size of the virtual cavity and polarization $-\mathbf{P}$, and all the discrete dipoles in the cavity.

dipoles inside the cavity, see Fig 2.3. In fact, the homogeneous polarization **P** inside the cavity is replaced by the field of the individual dipoles. The field inside a polarized dielectric sphere $\mathbf{E}_{\mathrm{P}}$, without external field, is just given by the depolarization field $\mathbf{E}_{\mathrm{depol}}$, see Eqs. 2.17 and 2.20. The fields due to the discrete dipoles inside the cavity add up to zero, for the contribution of these fields is given by the summation of Eq. 2.41, that is $\mathbf{E}_{\mathrm{near}} = 0$. As a result, the local field, expressed in only macroscopic quantities, reduces to

$$\mathbf{E}_{\mathrm{loc}} = \mathbf{E}_{\mathrm{mac}} + \frac{1}{3}\mathbf{P}. \tag{2.44}$$

Combining $\mathbf{P} = \rho\alpha\mathbf{E}_{\mathrm{loc}} = \rho\alpha[\mathbf{E}_{\mathrm{mac}} + (1/3)\mathbf{P}]$ and $\mathbf{P} = (\varepsilon - 1)\mathbf{E}_{\mathrm{mac}}$ readily gives the by now well-known result of Eqs. 2.33 and 2.40. It should be stressed that the approach presented here resides on the use of macroscopic quantities that are not derived from microscopic ones, in contrast with the method of the previous sections. Note that the local field differs from the macroscopic field by the so called Lorentz local-field factor L_{Lor}:

$$\mathbf{E}_{\mathrm{loc}} \equiv L_{\mathrm{Lor}}\mathbf{E}_{\mathrm{mac}} = \frac{\varepsilon + 2}{3}\mathbf{E}_{\mathrm{mac}} \tag{2.45}$$

For $\varepsilon \simeq 1$, that is $\rho\alpha \ll 1$, the local field approximately equals the macroscopic field, establishing the applicability of the linear response approach in this regime.

2.4.5 The Onsager-Böttcher approach; the reaction field

In the Onsager-Böttcher approach an impurity dipole $\mathbf{p}_{\mathrm{I}}$ is considered to be at center of a real spherical cavity with radius a in an otherwise homogeneous dielectric with dielectric constant ε [14], see Fig. 2.4. The field at the site of the dipole $\mathbf{E}_{\mathrm{loc}}$ is given by the sum of the field inside the cavity $\mathbf{E}_{\mathrm{in}}$ [Eq. 2.23] due to an external

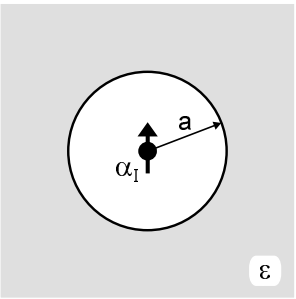

Figure 2.4 The Onsager-Böttcher treatment: An impurity dipole with polarizability α_I, the dipole in question, is placed at the center of a real spherical cavity (radius a) in a homogeneous medium with dielectric constant ε.

macroscopic field $\mathbf{E}_{\text{mac}}$ and the *reaction field* $\mathbf{R}$. The reaction field originates from the polarization of the surrounding dielectric induced by the central dipole. This field $\mathbf{R}$ is uniform throughout the cavity and proportional to the dipole moment $\mathbf{p}_I$ [14]:

$$\mathbf{R} = \frac{1}{3\Omega}\frac{2(\varepsilon-1)}{2\varepsilon+1}\mathbf{p}_I \equiv f\mathbf{p}_I, \tag{2.46}$$

where $\Omega = (4\pi a^3)/3$ is the volume of the cavity. The dipole moment $\mathbf{p}_I$ is induced by the total field at the center of the cavity $\mathbf{E}_{\text{loc}} = \mathbf{E}_{\text{in}} + \mathbf{R}$: $\mathbf{p}_I = \alpha_I \mathbf{E}_{\text{loc}}$. Hence, the reaction field is given by

$$\mathbf{R} = f\mathbf{p}_I = f\alpha_I(\mathbf{E}_{\text{in}} + \mathbf{R}), \tag{2.47}$$

from which it follows that

$$\mathbf{E}_{\text{loc}} = \frac{1}{1-f\alpha_I}\mathbf{E}_{\text{in}} = \frac{1}{1-f\alpha_I}\frac{3\varepsilon}{2\varepsilon+1}\mathbf{E}_{\text{mac}}, \tag{2.48}$$

where Eq. 2.23 is used. Rewriting this equation, using the explicit form for f, resides for the local field to

$$\mathbf{E}_{\text{loc}} = \frac{3\varepsilon}{2\varepsilon+1-\frac{2\alpha_I}{3\Omega}(\varepsilon-1)}\mathbf{E}_{\text{mac}} \equiv L_{\text{OB}}(\alpha_I/\Omega)\mathbf{E}_{\text{mac}}, \tag{2.49}$$

where $L_{\text{OB}}(\alpha_I/\Omega)$ is defined in analogy with L_{emp} and L_{Lor}. The field outside the cavity is given by the sum of $\mathbf{E}_{\text{mac}}$ and the field of a dipole embedded in a host material with dielectric constant ε with dipole moment

$$\mathbf{p}_{\text{tot}} = \left[\alpha_I L_{\text{emp}} L_{\text{OB}}(\alpha_I/\Omega) + (1-\varepsilon)L_{\text{emp}}\Omega\right]\mathbf{E}_{\text{mac}}, \tag{2.50}$$

where the first term presents the dipole field produced by the central impurity dipole and the second term corresponds to dipole field of an empty cavity, see Eq. 2.22. The volume of the cavity Ω is the only unknown parameter left. In contrast to the virtual cavity approach, two cases can be distinguished: the dipole inside the cavity is either equivalent to or different from the ones forming the dielectric. Considering the former case ($\alpha_{\rm I} = \alpha$, where α is the polarizability of the dipoles that form the dielectric), Eq. 2.33 and 2.40 are regained upon Onsager's assumption [15] that the volume of the cavity obeys $\rho\Omega = 1$ and realizing that $\mathbf{P} = \rho\alpha\mathbf{E}_{\rm loc} = (\varepsilon - 1)\mathbf{E}_{\rm mac}$. Here ρ is the density of the dipoles in the dielectric. In other words, the average polarization in the cavity, $\mathbf{p}_{\rm I}/\Omega = \rho\mathbf{p}$, equals the polarization of the dielectric, see for example Eq. 2.32. As a result, $\mathbf{p}_{\rm tot}$ in Eq. 2.50 is zero, as it should for a homogeneous medium.

In the case of an impurity dipole, the volume Ω is generally taken to be the real volume of the molecule or atom the dipole represents. Note that for impurity dipoles with a very low polarizability, $\alpha_{\rm I}/\Omega \ll 1$, the empty cavity result [Eq. 2.23] is obtained: $L_{\rm OB}(0) = L_{\rm emp}$.

2.4.6 Historical overview on local fields

The concept of local fields, the field experienced by a dipole in a dielectric medium, has been a subject of interest for over 150 years, see for reviews [28, 29, 30]. The first familiar results were obtained by Mossotti [31] who considered small metal particles in an 'ether' and by Clausius [32] who extended Mossotti's results to conducting particles in an insulating medium. In fact, to be more precise, they established that, for any given substance, $(\varepsilon - 1)/(\varepsilon + 2)$ should be proportional to the density of the substance. Rewriting Eqs. 2.33 and 2.40 indeed confirms such a relation:

$$\rho\alpha = 3\frac{\varepsilon - 1}{\varepsilon + 2}, \tag{2.51}$$

known as the *Clausius-Mossotti equation*. This equation can be generalized to the case of mixtures of different types of dipoles with polarizabilities α_i and densities ρ_i. It then reads

$$\frac{\varepsilon - 1}{\varepsilon + 2} = \frac{1}{3}\sum_i \rho_i\alpha_i, \tag{2.52}$$

which is the more familiar form.

Lorenz [33] studied dielectric particles surrounded by a medium with a different refractive index and solved the problem for optical vibrations. He was the first to introduce the idea that, in a cubic or random distribution, the contributions of

near neighbors to the local field sum to zero, although this was an assumption rather than a proven result. Lorentz [34] used the by now familiar method (see previous section) of cutting out a virtual sphere about the site in question. He was able to show that indeed the contribution of the neighbors within the sphere in a cubic lattice is zero. For dynamical fields, Eq. 2.52 is better known as the *Lorentz-Lorenz equation*.

Over the last century, several rederivations of Lorentz's original result have been given [15, 28, 35, 36]. All of these derivations, however, use the concept of a local field and apply the macroscopic Maxwell equations to achieve the result. Recently, an exact microscopic derivation for fluids has been presented by Lagendijk *et al.* using the formalism of multiple-scattering theory taking into account hard-sphere particle correlations to all orders of the density [37]. For static fields, a similar approach was adopted by Felderhof *et al.* [38]. It should be noted, that these correlations were implicitly included in the derivations of sections 2.4.2 and 2.4.3, as the field felt by a particular dipole is just the sum of the external field and the scattered fields of all the other dipoles, *excluding* the depolarization fields, see Eqs. 2.28 and 2.29. That is to say: the dipoles were not at the same position.

2.5 Wave propagation and the dielectric function

So far, only the dielectric function $\varepsilon(\omega)$ has been calculated from microscopic quantities. The implications of such a dielectric function on the properties of light wave propagation through dielectrics will be discussed now.

For homogeneous media and monochromatic light with frequency ω, the Helmholtz equation reads

$$\nabla^2 \mathbf{E}_{\text{mac}}(\mathbf{r}) - \varepsilon(\omega)\frac{\omega^2}{c_0^2}\mathbf{E}_{\text{mac}}(\mathbf{r}) = 0, \tag{2.53}$$

where it is understood that the time dependence of the macroscopic field is $\mathrm{e}^{-i\omega t}$. The solution of Eq. 2.53 is a transverse plane wave

$$\mathbf{E}_{\text{mac}}(\mathbf{r},t) = \mathbf{E}_0\,\mathrm{e}^{ik\mathbf{n}\cdot\mathbf{r}-i\omega t}, \tag{2.54}$$

where $\mathbf{E}_0$ is the amplitude of the wave, $\mathbf{n}$ a unit vector pointing in the direction of propagation and

$$k = \sqrt{\varepsilon(\omega)}\frac{\omega}{c_0} \tag{2.55}$$

the wavevector in the medium. Note that $\mathbf{E}_0 \cdot \mathbf{n} = 0$. In general, $\varepsilon(\omega)$ is a complex function: $\varepsilon \equiv \varepsilon_R + i\varepsilon_I$. The real part of dielectric function ε_R relates to the refractive

index m, whereas the imaginary part ε_I describes both absorption and scattering, *i.e.* extinction. As a result k is complex: $k \equiv \beta + i\kappa/2$. So that the *intensity* of the wave falls off as $e^{-\kappa \mathbf{n}\cdot\mathbf{r}}$, see Eq. 2.54. Consequently, κ is identified as the extinction coefficient, that is the inverse of extinction length $\ell_{\rm ex}$: $\kappa = \ell_{\rm ex}^{-1}$. Both β and κ can be expressed in terms of ε_R and ε_I using Eq. 2.55. If $\kappa \ll \beta$, which is the case for nearly all media unless they are extremely strongly absorbing and/or scattering, it is found that

$$\beta = \sqrt{\varepsilon_R}\frac{\omega}{c_0}, \qquad \kappa = \frac{\varepsilon_I}{\varepsilon_R}\beta, \tag{2.56}$$

from which it follows that the refractive index m is $\sqrt{\varepsilon_R}$. Using Eq. 2.56, it is clear how the refractive index m and the extinction length $\ell_{\rm ex}$ depend on microscopic quantities like the dipole density ρ and dynamic polarizability $\alpha(\omega)$.

The imaginary part of the dielectric function given by Eq. 2.33 arises from a complex dynamic polarizability $\alpha(\omega)$, see Eq. 2.6. Note that in the static limit, $\omega \downarrow 0$, $\alpha(\omega)$ becomes real and extinction disappears ($\kappa = 0$). In other words, absorption and scattering are essentially dynamic properties.

2.6 Mixtures of dielectrics

As the origin of the refractive index and extinction coefficient of *homogeneous* dielectrics is clear, it is interesting to investigate *inhomogeneous* dielectrics. For this purpose, consider a mixture of two dielectrics, with volume fractions ϕ_1 and ϕ_2, and dielectric constants ε_1 and ε_2, respectively. Aside from the dielectric constants and the volume fractions, the *average* refractive index $\varepsilon_{\rm av}$ and the extinction length depend on how the two dielectric components are organized and their dimensions. In the electrostatic limit, the components always have dimensions much smaller than the (infinitely) long wavelength, leading to a well-defined average refractive index. However, the extinction ($\ell_{\rm ex} \to \infty$) is zero in this limit. So in order to grasp both the extinction and average refractive index, the derivations will be in the quasi-static approximation.

As already mentioned, the morphology of the mixture influences both m and $\ell_{\rm ex}$. Three different effective medium models will be discussed: The Lorentz-Lorenz model [29], Maxwell Garnett theory [39] and Bruggeman's approach [40]. In the Lorentz-Lorenz model two types of dielectric spheres in vacuum are treated. Garnett considered spherical inclusions, *i.e.* scatterers, in a homogeneous dielectric background (cermet topology), whereas Bruggeman treated both dielectric components on an equal basis, more appropriate for the so-called aggregate topology [41]. In the cermet topology each inclusion is completely surrounded by the host dielectric, whereas in the aggregate topology the connectedness of the two components

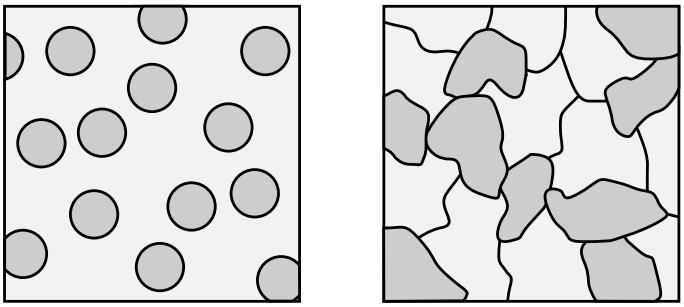

Figure 2.5 Two topologies of two-component dielectrics. The lighter and darker areas correspond to the different dielectric constant materials. Left a collection of spherical inclusions is depicted, the cermet topology, related to the Maxwell Garnett formalism. Right the aggregate topology is shown, considered by Bruggeman, which is symmetric in the statistical sense: *i.e.* an interchange of the two components results in the same type of medium with interchanged volume fractions. This symmetry is absent in the Maxwell Garnett type of mixture (left).

is treated on the same footing, see Fig. 2.5. For recent investigations of effective medium models for different morphologies see [42].

2.6.1 Quasi-static properties of a small dielectric sphere

In order to derive Maxwell Garnett results, first the small dielectric sphere is rediscussed; the results will be very similar to those in section 2.3. Consider a small dielectric sphere with dielectric constant ε_1 in otherwise homogeneous medium with dielectric constant ε_2. The sphere has a radius a (volume $\Omega = (4\pi a^3)/3$), much smaller than the wavelength involved, so that the quasi-static approach applies. In the host medium the macroscopic electric field far away from the sphere is homogeneous and given by $\mathbf{E}_2$. Analogous to Eq. 2.17, the macroscopic field inside the sphere $\mathbf{E}_1$ is homogeneous and reads

$$\mathbf{E}_1 = \frac{3}{\varepsilon+2}\mathbf{E}_2, \tag{2.57}$$

where $\varepsilon \equiv \varepsilon_1/\varepsilon_2$ is the dielectric constant ratio. The total field outside the dielectric sphere is the sum of $\mathbf{E}_2$ and the field of dipole in a background medium with dielectric constant ε_2 and dipole moment

$$\mathbf{p} = 3\varepsilon_2\Omega\frac{\varepsilon-1}{\varepsilon+2}\mathbf{E}_2 \equiv \alpha_{\varepsilon_1,\varepsilon_2}(0)\mathbf{E}_2 \equiv \varepsilon_2\alpha_\varepsilon(0)\mathbf{E}_2, \tag{2.58}$$

where $\alpha_{\varepsilon_1,\varepsilon_2}(0)$ is the static polarizability of the sphere and $\alpha_\varepsilon(0)$ is defined for later convenience.

In the quasi-static limit, the *dynamic* polarizability (necessary to describe extinction) is given by Eq. 2.6, where it is assumed that $\omega \ll \omega_0$. Keeping only the first order terms for both the real and imaginary part of the polarizability, it is found that

$$\alpha_{\varepsilon_1,\varepsilon_2}(\omega) \simeq \alpha_{\varepsilon_1,\varepsilon_2}(0)\left[1 + i\frac{\Gamma_0(\varepsilon_2)\,\omega^3}{\omega_0^4}\right]. \tag{2.59}$$

Here $\Gamma_0(\varepsilon_2)$ is the damping rate of a dipole in a background medium with dielectric constant ε_2. In order to fulfill the optical theorem, this damping rate relates to vacuum damping rate, see Eq. 2.5, as

$$\Gamma_0(\varepsilon_2) = \sqrt{\varepsilon_2}\,\Gamma_0, \tag{2.60}$$

which is the general result for a dipole in a dielectric host medium. Of course, the static polarizability in Eq. 2.5 is now given by $\alpha_{\varepsilon_1,\varepsilon_2}(0)$. Note that although Eq. 2.59 seems to depend on ω_0, this dependence is completely canceled by Γ_0, see Eq. 2.5: the quasi-static polarizability $\alpha_{\varepsilon_1,\varepsilon_2}(\omega)$ is completely independent of ω_0. The imaginary part of $\alpha_{\varepsilon_1,\varepsilon_2}(\omega)$ represents scattering and not absorption, as the scatterer is constructed to be fully elastic on enforcing the optical theorem.

2.6.2 The average dielectric constant

Lorentz-Lorenz expression Consider a collection of two types of spheres characterized by the densities ρ_i, dielectric constants ε_i, and volumes Ω_i (i=1,2) embedded in vacuum. The average dielectric constant $\varepsilon_{\rm av}$ of such a mixture can be calculated from Eq. 2.52 giving

$$\frac{\varepsilon_{\rm av}-1}{\varepsilon_{\rm av}+2} = \frac{1}{3}\left[\rho_1\alpha_1 + \rho_2\alpha_2\right], \tag{2.61}$$

where α_i is polarizability of sphere i. Using Eq. 2.21, the Lorentz-Lorenz effective medium expression resides to

$$\frac{\varepsilon_{\rm av}-1}{\varepsilon_{\rm av}+2} = \phi_1\frac{\varepsilon_1-1}{\varepsilon_2+2} + \phi_2\frac{\varepsilon_2-1}{\varepsilon_2+2}, \tag{2.62}$$

where $\rho_i\Omega_i$ is identified as the volume fraction ϕ_i. If the phases ε_1 and ε_2 completely fill the entire space, $\phi_1+\phi_2=1$. Obviously Eq. 2.62 can be generalized to systems containing more than two phases by adding more terms.

Maxwell Garnett theory Maxwell Garnett theory treats an inhomogeneous medium that consists of spheres with dielectric constant ε_1 and volume fraction ϕ_1 embedded in a background material with dielectric constant ε_2 and corresponding volume fraction $\phi_2 = 1 - \phi_1$. The derivation of the average dielectric constant ε_{av} presented here essentially follows the approach of Bohren and Huffman [43].

The average macroscopic electric field $\langle \mathbf{E} \rangle$ can be found by using the spatial averaging procedure, see section 2.2 and especially Eq. 2.12. The spatial averaging volume is large enough to contain many of the spherical inclusions. As a result

$$\langle \mathbf{E} \rangle = (1 - \phi_1)\langle \mathbf{E}_2 \rangle + \phi_1 \langle \mathbf{E}_1 \rangle, \tag{2.63}$$

where $\langle \mathbf{E}_2 \rangle$ and $\langle \mathbf{E}_1 \rangle$ are the average macroscopic fields in the background medium and the sphere, respectively. Similarly, the average polarization is given by

$$\langle \mathbf{P} \rangle = (1 - \phi_1)\langle \mathbf{P}_2 \rangle + \phi_1 \langle \mathbf{P}_1 \rangle. \tag{2.64}$$

The average polarization in the spheres and in the host material relate to the corresponding average macroscopic fields as

$$\langle \mathbf{P}_2 \rangle = (\varepsilon_2 - 1)\langle \mathbf{E}_2 \rangle, \qquad \langle \mathbf{P}_1 \rangle = (\varepsilon_1 - 1)\langle \mathbf{E}_1 \rangle. \tag{2.65}$$

The average dielectric constant ε_{av} of the composite medium is *defined* by

$$\langle \mathbf{P} \rangle = (\varepsilon_{av} - 1)\langle \mathbf{E} \rangle. \tag{2.66}$$

Combining Eqs. 2.63-2.66 yields

$$(1 - \phi_1)(\varepsilon_{av} - \varepsilon_2)\langle \mathbf{E}_2 \rangle + \phi_1(\varepsilon_{av} - \varepsilon_1)\langle \mathbf{E}_1 \rangle = 0. \tag{2.67}$$

For spherical inclusions the relation between $\langle \mathbf{E}_2 \rangle$ and $\langle \mathbf{E}_1 \rangle$ is known and given by Eq. 2.57. Here it is assumed that the fields scattered by the spheres average out to zero, similar to the treatment of fluids in section 2.4.2. The Maxwell Garnett result for the average dielectric constant follows:

$$\varepsilon_{av} = \varepsilon_2 \left[1 + \frac{3\phi_1 \left(\frac{\varepsilon - 1}{\varepsilon + 2}\right)}{1 - \phi_1 \left(\frac{\varepsilon - 1}{\varepsilon + 2}\right)} \right], \tag{2.68}$$

where again $\varepsilon \equiv \varepsilon_1/\varepsilon_2$. Identifying ϕ_1 as $\rho\Omega$, where ρ the density and Ω the volume of the spheres, and using the definition of $\alpha_\varepsilon(0)$ from Eq. 2.58, leads to

$$\varepsilon_{av} = \varepsilon_2 \left[1 + \frac{\rho\alpha_\varepsilon(0)}{1 - \frac{1}{3}\rho\alpha_\varepsilon(0)} \right], \tag{2.69}$$

clearly establishing the connection to the polarizability of a dielectric sphere, see Eq. 2.58. Note that the form of Eq. 2.69 is identical to Eqs. 2.33 and 2.40.

Equation 2.68 can be rewritten in a form similar to Eq. 2.62 yielding

$$\frac{\varepsilon_{av}-\varepsilon_2}{\varepsilon_{av}+2\varepsilon_2}=\phi_1\frac{\varepsilon_1-\varepsilon_2}{\varepsilon_1+2\varepsilon_2}, \tag{2.70}$$

so that both Eqs. 2.62 and 2.70 are identified to stem from the same general formula

$$\frac{\varepsilon_{av}-\varepsilon_h}{\varepsilon_{av}+2\varepsilon_h}=\phi_1\frac{\varepsilon_1-\varepsilon_h}{\varepsilon_1+2\varepsilon_h}+\phi_2\frac{\varepsilon_2-\varepsilon_h}{\varepsilon_2+2\varepsilon_h}, \tag{2.71}$$

where ε_h is the dielectric constant of a host dielectric. Thus ε_h equals 1 and ε_2 for the Lorentz-Lorenz and Maxwell Garnett expressions, respectively. If $\phi_1 > \phi_2$, then a more appropriate choice for ε_h in the Maxwell Garnett case is ε_1. However, the resulting values of ε_{av} are different for the two choices. Bruggeman resolved this dilemma.

Bruggeman's approach Bruggeman proposed that neither phase should be given preference (as in the Maxwell Garnett treatment), but that the inclusions should be considered as being embedded in the averaged medium itself. In the above formulation this is equivalent to choosing $\varepsilon_h = \varepsilon_{av}$, in which case Eq. 2.71 becomes

$$0=\phi_1\frac{\varepsilon_1-\varepsilon_{av}}{\varepsilon_1+2\varepsilon_{av}}+\phi_2\frac{\varepsilon_2-\varepsilon_{av}}{\varepsilon_2+2\varepsilon_{av}}, \tag{2.72}$$

known as the Bruggeman effective medium expression. Although Eqs. 2.62, 2.70, and 2.72 are superficially quite different, the above discussion shows that they all are related and differ only in the choice of the host material. The generalization to mixtures of more than two dielectrics is obvious.

2.6.3 Light scattering in mixtures

Scattering of light in dielectrics originates from the complex dynamic polarizability. To indicate how this really works, the extinction coefficient κ is calculated for the Maxwell Garnett result in the linear response approximation, that is $\rho\alpha_\varepsilon \ll 1$. The quasi-static dielectric function $\varepsilon(\omega)$ then reads

$$\varepsilon(\omega)=\varepsilon_2+\rho\alpha_{\varepsilon_1,\varepsilon_2}(\omega), \tag{2.73}$$

where $\alpha_{\varepsilon_1,\varepsilon_2}(\omega)$ is the complex quasi-static polarizability given by Eq. 2.59. Again, it is stressed that this complex polarizability is constructed via the optical theorem, so that the spheres are fully elastic scatterers. The real (ε_R) and imaginary (ε_I) part of $\varepsilon(\omega)$ thus are

$$\varepsilon_R=\varepsilon_2+\rho\alpha_{\varepsilon_1,\varepsilon_2}(0), \qquad \varepsilon_I=\rho\sqrt{\varepsilon_2}\left[\alpha_{\varepsilon_1,\varepsilon_2}(0)\right]^2\frac{\omega^3}{6\pi c_0^3}, \tag{2.74}$$

where $\Gamma(\varepsilon_2)$ and ω_0 are eliminated by use of Eqs. 2.5 and 2.60. The refractive index m is just given by $\sqrt{\varepsilon_R} = \sqrt{\varepsilon_2 + \rho\alpha_{\varepsilon_1,\varepsilon_2}(0)}$, which approximates to $\sqrt{\varepsilon_2}$ for $\rho\alpha_{\varepsilon_1,\varepsilon_2}(0) \ll \varepsilon_2$. The extinction coefficient κ, or equivalently the inverse of the extinction length ℓ_{ex}, follows from Eqs. 2.56, and 2.74 and reads

$$\kappa = \rho\left[\alpha_{\varepsilon_1,\varepsilon_2}(0)\right]^2 \frac{\omega^4}{6\pi c_0^4}. \tag{2.75}$$

This equation is related to the extinction cross-section σ_{ex}, which is defined as $\rho\sigma_{\text{ex}} \equiv \kappa = \ell_{\text{ex}}^{-1}$. Using Eq. 2.75 and the explicit form of $\alpha_{\varepsilon_1,\varepsilon_2}(0)$ [Eq. 2.58] the well-known extinction cross-section for a spherical Rayleigh scatterer is readily obtained

$$\sigma_{\text{ex}} = \frac{8}{3}x^4\left[\frac{\varepsilon-1}{\varepsilon+2}\right]^2 \pi a^2 \equiv Q_{\text{ex}}\pi a^2 \tag{2.76}$$

Here $x \equiv k_{\varepsilon_2}a$, where $k_{\varepsilon_2} = \sqrt{\varepsilon_2}(\omega/c_0)$ is the wavevector in the background dielectric ε_2 and a the radius of the sphere. Furthermore, the extinction efficiency factor Q_{ex} is defined as the ratio of the extinction cross-section σ_{ex} to the geometrical cross-section πa^2. This completes the derivation of extinction by a low concentration of small dielectric spheres in a dielectric host material.

CHAPTER 3

Spontaneous emission of impurity atoms in homogeneous dielectrics

The spontaneous emission rate of an impurity atom in an otherwise homogeneous dielectric is calculated using the Onsager-Böttcher approach. By identifying substitutional and interstitial impurities, the well-known empty-cavity and Lorentz local-field factors are obtained, respectively. For fluids, the substitutional case is predicted to occur prevalently.

3.1 Introduction

In 1917, Einstein demonstrated that spontaneous emission must occur if matter and radiation are to achieve thermal equilibrium [44]. This picture is so fundamental, that spontaneous emission rates are often believed to be an inherent property of the atom. However, the spontaneous emission rate can be modified by changing the environment, as was noticed by Purcell [45]. In the early 1970s, Drexhage carried out pioneering experiments on the modification of the luminescence decay rate of Europium complexes in front of a metallic mirror [46]. Later, many theoretical [47] and experimental [48] investigations have been devoted to the enhancement and inhibition of spontaneous emission of atoms in resonant cavities, in which case larger modifications are possible.

Modifications of the spontaneous emission rate can also be induced by placing the radiator inside a spatially inhomogeneous dielectric. For example, the case of emission near a dielectric interface has been studied both experimentally [46, 49] and theoretically [50]. More recently, spontaneous emission rates were predicted to alter in photonic crystals [8], materials in which the dielectric constant is periodically modulated on length scales of the wavelength of light. As a result, light in a certain frequency range cannot propagate in the crystal because of multiple Bragg reflections. At this so-called full photonic band gap, the radiative density of states (RDOS) is zero and, therefore, spontaneous emission of excited atoms embedded

in these materials is expected to be inhibited at those frequencies, since then coupling to propagating modes is absent. At other frequencies, it has been shown that spontaneous emission can be either enhanced or reduced [8]. Note that the atoms in question are different from the ones constituting the dielectric; in the rest of this chapter such atoms will be referred to as *impurity* atoms or, equivalently, impurity dipoles.

In this chapter, the most simple and fundamental problem is treated: the spontaneous emission rate of an impurity dipole in a macroscopically homogeneous dielectric. As will be shown, merely placing a dipole in a dielectric medium already modifies its spontaneous emission rate.

3.2 Which local-field correction applies to spontaneous emission?

The spontaneous emission rate $\Gamma(\varepsilon)$ of an impurity dipole inside a homogeneous medium with dielectric constant ε is predicted by Nienhuis and Alkemade [10] to follow the $\sqrt{\varepsilon}$ dependence of the RDOS, and is thus given by

$$\Gamma(\varepsilon) = \sqrt{\varepsilon}\,\Gamma_0, \tag{3.1}$$

where Γ_0 is radiative decay rate of the dipole in vacuum. This dependence of $\Gamma(\varepsilon)$ is exactly identical to Eq. 2.60, which describes the radiation damping rate, the classical analog of spontaneous emission, of the dynamic polarizability of a dipole inside a dielectric that fulfills the optical theorem. However, Nienhuis and Alkemade arrived at Eq. 3.1 by quantizing the macroscopic Maxwell's equations, while in principle the dipole couples to the microscopic vacuum fluctuations. The microscopic, or local, electric field felt by a dipole is usually different from the macroscopic field, and hence deviations from Eq. 3.1 are expected.

The concept of the local field was already explained in detail in the previous chapter. There it was shown that for highly symmetric, completely homogeneous dielectrics, *i.e.* fluids and cubic lattices, the ratio of the local to the macroscopic field is given by the Lorentz local-field factor

$$L_{\mathrm{Lor}} = \frac{\varepsilon + 2}{3}, \tag{3.2}$$

which is the same for all dipoles that constitute the dielectric, see also Eq. 2.45. Indeed, in experiments [51] involving only *pure* systems, *i.e.* only one kind of atom or molecule is present, the observed local-field effects agree very well with this Lorentz description. However, in the case of an impurity dipole, it is not at all clear whether Eq. 3.2 should apply.

The Onsager-Böttcher local-field approach, see section 2.4.5, allows an impurity dipole to be treated: an impurity dipole with polarizability α_{I} is placed at the

center of a spherical cavity with volume Ω in an otherwise homogeneous medium with dielectric constant ε. The local-field correction pertaining to the field in the cavity is

$$L_{\mathrm{OB}}(\alpha_{\mathrm{I}}/\Omega) = \frac{3\varepsilon}{2\varepsilon + 1 - \frac{2\alpha_{\mathrm{I}}}{3\Omega}(\varepsilon - 1)}, \tag{3.3}$$

see Eq. 2.49. As already explained, the Lorentz result [Eq. 3.2] is regained when the polarizability α_{I} of the impurity dipole is identical to the polarizability α of the dipoles that form the dielectric, and the inverse volume Ω^{-1} of the cavity equals the density ρ of dipoles in the medium.

Considering the case of an impurity dipole inside the cavity, one sometimes neglects the response of the dielectric on α_{I}, *i.e.* the reaction field is neglected. Equation 3.3 then simplifies to the so-called empty-cavity factor

$$L_{\mathrm{emp}} = \frac{3\varepsilon}{2\varepsilon + 1}, \tag{3.4}$$

identical as for the field inside a real empty cavity, see Eq. 2.23. It has been proposed theoretically [13, 16, 52, 53] that one of the factors, L_{Lor} or L_{emp}, should be included in a description of $\Gamma(\varepsilon)$ of impurity dipoles inside dielectrics, that is $\Gamma(\varepsilon) = \sqrt{\varepsilon} L_{\mathrm{Lor}}^2 \Gamma_0$ or $\Gamma(\varepsilon) = \sqrt{\varepsilon} L_{\mathrm{emp}}^2 \Gamma_0$. The majority of the researchers in the field [53] favor the Lorentz factor. On the other hand, experimental results [54, 55] indicate that the empty-cavity factor [52] should be employed. Obviously, there is a controversy to be resolved.

Barnett *et al.* [13] indicated that part of the confusion arises from the choice of cavity that is used in the macroscopic derivation of the local-field correction. The virtual cavity, often employed in the derivation of the Lorentz-Lorenz equation [see section 2.4.4], would give rise to L_{Lor}. Contrary, L_{emp} applies when the impurity dipole is considered inside a real empty cavity. They do not make a clear statement as to which type of cavity applies to impurity dipoles in a dielectric.

De Vries and Lagendijk [16] presented a full microscopic calculation of point dipoles on a cubic lattice, which form the dielectric, plus one impurity dipole, using Green's function formalism [27]. The resonance width of the elastic impurity dipole is taken as the spontaneous emission rate. For substitutional impurity dipoles, that is a medium dipole is replaced by an impurity dipole (at a lattice position), the empty cavity result L_{emp} is found to apply. For interstitials, that is the impurity dipole is placed in between lattice sites and no medium dipoles are removed, the Lorentz-cavity factor L_{Lor} determines the modification of spontaneous emission. In this derivation, the polarizability of the impurity dipoles is required to obey the optical theorem, so that it captures spontaneous emission. In fact, the

optical theorem may be viewed as the microscopic analogon of Einstein's thermodynamic arguments [44] relating absorption, stimulated and spontaneous emission. A generalization to fluids is made and it is concluded that most often the substitutional result, that is L_{emp}, applies, in agreement with experimental observations [54, 55].

In the rest of this chapter, an alternative derivation of the results of De Vries and Lagendijk [16] will be presented, using the Onsager-Böttcher approach to model both substitutional and interstitial impurity dipoles.

3.3 Substitutional impurity dipoles

In the case of the substitutional impurity dipole, just the standard Onsager-Böttcher approach is considered. The impurity dipole in the cavity replaces the medium dipole, which would have been there in the case of a homogeneous dielectric. So indeed, the impurity dipole substitutes a dipole of the dielectric. In the far field, the total static polarizability for the substitutional case is then given by [see Eq. 2.50]

$$\alpha_{\mathrm{sub}} = \alpha_{\mathrm{I}} L_{\mathrm{emp}} L_{\mathrm{OB}} (\alpha_{\mathrm{I}}/\Omega) + (1-\varepsilon) L_{\mathrm{emp}} \Omega, \tag{3.5}$$

where the first term is the contribution of the impurity dipole α_{I}, and the second corresponds to the polarizability of the empty cavity with volume Ω. Note that for $\alpha_{\mathrm{I}} = 0$, the total static polarizability α_{sub} is not zero; the polarizability of the empty cavity is still remnant. The polarizability of the impurity dipole itself determines the spontaneous emission rate, and therefore only the first term of Eq. 3.5 is considered.

In order to obtain spontaneous emission rates, the dynamic polarizability is considered. The impurity dipole has to obey the optical theorem, as to describe spontaneous emission, and hence the dynamic polarizability of the dipole in *vacuum* is

$$\alpha_{\mathrm{I}}(\omega) = \alpha_{\mathrm{I}}(0) \times \frac{\omega_0^2}{\omega_0^2 - \omega^2 - i(\Gamma_0 \omega^3/\omega_0^2)}, \tag{3.6}$$

identical to Eq. 2.6. For completeness, here $\alpha_{\mathrm{I}}(0)$ is the static polarizability, ω_0 the resonance frequency, and Γ_0 the vacuum spontaneous emission rate. Implementing this polarizability $\alpha_{\mathrm{I}}(\omega)$ in Eq. 3.5 readily gives the dynamic polarizability $\alpha_{\mathrm{sub,I}}(\omega)$ of a substitutional impurity

$$\alpha_{\mathrm{sub,I}}(\omega) = \alpha_{\mathrm{I}}(\omega) L_{\mathrm{emp}}^2 \left[1 - \frac{2\alpha_{\mathrm{I}}(\omega)(\varepsilon - 1) L_{\mathrm{emp}}}{9\varepsilon\Omega} \right]^{-1}, \tag{3.7}$$

where $L_{\rm OB}(\alpha_{\rm I}(\omega)/\Omega)$ is explicitly written in terms of $L_{\rm emp}$. The polarizability of this "dressed" impurity near resonance has a Lorentzian structure analogous to Eq. 3.6:

$$\alpha_{\rm sub,I}(\omega) = \alpha_{\rm sub,I}(0) \times \frac{\omega_0^2(\varepsilon)}{\omega_0^2(\varepsilon) - \omega^2 - i(\Gamma(\varepsilon)\omega^3/\omega_0^2(\varepsilon))}, \tag{3.8}$$

with parameters given by

$$\frac{\omega_0^2(\varepsilon)}{\omega_0^2} = \left[1 - \frac{2\alpha_{\rm I}(0)(\varepsilon-1)L_{\rm emp}}{9\varepsilon\Omega}\right], \tag{3.9}$$

$$\alpha_{\rm sub,I}(0) = L_{\rm emp}^2 \frac{\omega_0^2}{\omega_0^2(\varepsilon)}\alpha_{\rm I}(0), \tag{3.10}$$

$$\frac{\Gamma(\varepsilon)}{\Gamma_0} = \sqrt{\varepsilon}\, L_{\rm emp}^2 \frac{\omega_0^2(\varepsilon)}{\omega_0^2}. \tag{3.11}$$

Here the spontaneous emission rate $\Gamma(\varepsilon)$ of the substitutional impurity follows from the polarizability $\alpha_{\rm sub,I}(0)$ and the resonance frequency $\omega_0(\varepsilon)$ by use of the optical theorem, see Eqs. 2.5 and 2.60. Note that in vacuum, $\varepsilon = 1$, the original results are regained, that is $\omega_0(1) = \omega_0$, $\alpha_{\rm sub,I}(0) = \alpha_{\rm I}(0)$, and $\Gamma(1) = \Gamma_0$. The resonance frequency is red shifted and the line width behaves in accordance with the empty-cavity description, identical to the results of De Vries and Lagendijk [16].

3.4 Interstitial impurity dipoles

The case of the interstitial impurity dipole is modeled by placing an extra impurity dipole in the cavity without removing the medium dipole; there are two dipoles in the cavity. In principle, the impurity dipole can be placed anywhere in the cavity, but for convenience of calculation it is positioned at the center of the cavity, on top of the medium dipole. It might seem unjustified to place the impurity at a point of high symmetry. However, a randomly positioned impurity is *on average* indeed located at the center. Furthermore, even if the impurity is not placed at the exact center of the cavity, but reasonably close, the results found by assuming a centered impurity dipole are in first approximation correct, see pages 150-153 of [14]. This indicates that choosing a point of high symmetry for the position of the impurity does not determine the outcome of the derivation.

By symmetry, it follows that the impurity and medium dipole have the same orientation. As a result, analogous to Eq. 3.5, the total static polarizability for the interstitial case reads

$$\alpha_{\rm int} = (\alpha_{\rm I} + \alpha)L_{\rm emp}L_{\rm OB}((\alpha_{\rm I} + \alpha)/\Omega) + (1-\varepsilon)L_{\rm emp}\Omega, \tag{3.12}$$

where α is the polarizability of the dipoles that form the dielectric. The three different contributions (impurity dipole, medium dipole, and empty cavity) are clearly identified. Contrary to the substitutional case, the total polarizability $\alpha_{\rm int} = 0$ for $\alpha_{\rm I} = 0$, as then the medium is homogeneous, and hence the polarizabilities of the medium dipole and the empty cavity exactly cancel. In fact, $\alpha_{\rm int}$ represents the effective polarizability $\alpha_{\rm int,I}(\omega)$ of the interstitial impurity dipole embedded in the dielectric, that is $\alpha_{\rm int} = \alpha_{\rm int,I}(0)$. The polarizability α of the medium dipole can be eliminated from Eq. 3.12 by recognizing that $\alpha/\Omega = \rho\alpha = 3(\varepsilon-1)/(\varepsilon+2)$ [Eq. 2.51], where ρ is of course the density of the dipoles in the dielectric. The dynamic polarizability of the interstitial impurity then resides to

$$\alpha_{\rm int,I}(\omega) = \alpha_{\rm I}(\omega) L_{\rm Lor}^2 \left[1 - \frac{2\alpha_{\rm I}(\omega)(\varepsilon-1)L_{\rm Lor}}{9\varepsilon\Omega}\right]^{-1}, \tag{3.13}$$

where $\alpha_{\rm I}(\omega)$ is given by Eq. 3.6. Note that for $\alpha_{\rm I}(\omega) = 0$, indeed $\alpha_{\rm int,I}(\omega) = 0$. The structure of Eqs. 3.7 and 3.13 is identical, only $L_{\rm emp}$ in Eq. 3.7 is replaced by $L_{\rm Lor}$ in Eq. 3.13. Similar as in the substitutional case, the polarizability of the "dressed" interstitial impurity has a Lorentzian line shape given by Eq. 3.8. The parameters for the interstitial case are

$$\frac{\omega_0^2(\varepsilon)}{\omega_0^2} = \left[1 - \frac{2\alpha_{\rm I}(0)(\varepsilon-1)L_{\rm Lor}}{9\varepsilon\Omega}\right], \tag{3.14}$$

$$\alpha_{\rm int,I}(0) = L_{\rm Lor}^2 \frac{\omega_0^2}{\omega_0^2(\varepsilon)} \alpha_{\rm I}(0), \tag{3.15}$$

$$\frac{\Gamma(\varepsilon)}{\Gamma_0} = \sqrt{\varepsilon}\, L_{\rm Lor}^2 \frac{\omega_0^2(\varepsilon)}{\omega_0^2}. \tag{3.16}$$

Again the resonance frequency is red shifted, although with a different functional dependence on ε. The Lorentz local-field factor is found to determine the modification of the spontaneous emission rate, in agreement with Ref. [16].

3.5 Discussion

The obtained results for both the substitutional and interstitial impurity still depend on the volume of the cavity Ω. For the case of the interstitials the volume is fixed: $\Omega = \rho^{-1}$. For substitutionals, Ω is free and generally taken to be the real volume of the impurity atom or molecule. For small impurity volumes, $\Omega < \rho^{-1}$, only one dipole of the dielectric is expelled from the cavity. If the impurity is large, $\Omega \gg \rho^{-1}$,

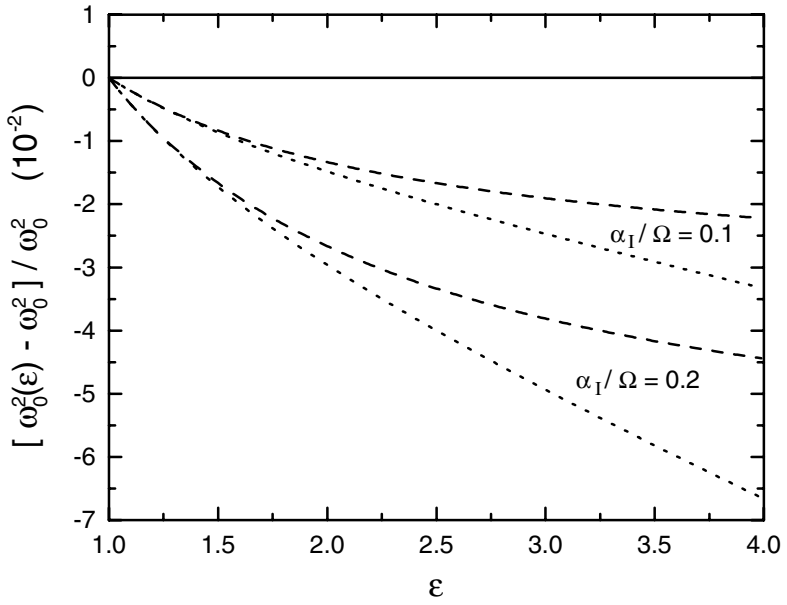

Figure 3.1 The red shift of the resonance frequency of substitutional (dashed lines, Eq. 3.9) and interstitial (dotted lines, Eq. 3.14) impurities, for two different polarization densities α_I/Ω. The solid line represents no shift, corresponding to $\alpha_I/\Omega \downarrow 0$. Note that the shift is rather small, only a few percent.

many dipoles of the dielectric are removed, and the impurity is a true macroscopic cavity.

The resonance frequency of the impurity slightly shifts to the red, see Fig. 3.1. This shift is a direct consequence of the reaction field produced by the polarization in the medium, which is induced by the impurity dipole. For small impurity polarization densities ($\alpha_I(0)/\Omega \ll 1$), the reaction field disappears, and thus the resonance frequency shift can be neglected ($\omega_0^2(\varepsilon) = \omega_0$). In experiments, this is nearly always the case, except for extremely polarizable atoms like Na, Li, Rb, so that a shift of the resonance frequency is difficult to observe.

The spontaneous emission rate increases upon placing the impurity dipole in a dielectric, see Fig. 3.2. The volume Ω of the cavity is irrelevant, if the impurity polarization density is small ($\alpha_I(0)/\Omega \ll 1$). The relatively large differences between the models should allow for a clear distinction in experiment.

Two different classes of common host media can be distinguished: crystalline and disordered materials. In crystalline materials, which are necessarily solid, both substitutional and interstitial impurities occur. The substitutionals are positioned at

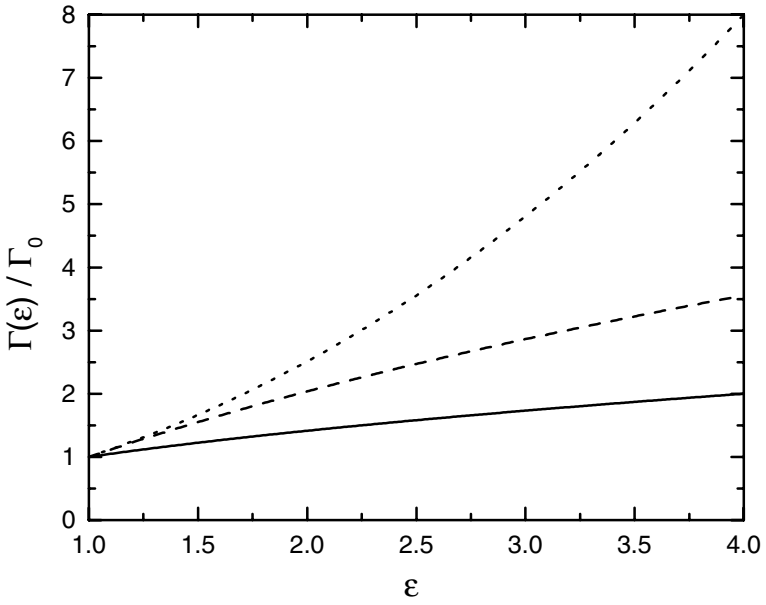

Figure 3.2 The relative spontaneous emission rate of substitutional (dashed line, Eq. 3.11) and interstitial (dotted line, Eq. 3.16) impurities for zero resonance frequency shift, that is $\omega_0^2(\varepsilon)/\omega_0^2 = 1$. The solid line comes from Eq. 3.1. Large deviations from the vacuum spontaneous emission rate Γ_0 are predicted to occur in dielectrics.

lattice sites, the interstitials somewhere in between. In the case of disordered materials, like fluids and glasses, this distinction is not so clear. For such host media, it is essential to consider the local environment in order to distinguish between substitutional and interstitial [16]. Interstitial behavior occurs when impurities do not influence the positions of the particles that form the dielectric. So the volume of the impurity has to be much smaller than the voids in between the medium dipoles. On the other hand, if the size of the impurity is comparable, or larger, than the size of the medium particles, the substitutional result applies. As, in that case, the impurity forms a real excluded volume for the dipoles of the dielectric. At very low densities, the distinction between the two types of impurities is not relevant, since any distinct feature of positional correlation of the medium dipoles will disappear, and $L_{\rm Lor} \approx L_{\rm emp}$ to first order in Ω^{-1}. In the case of fluids, only substitutional behavior is expected to occur, as the sizeable dimensions of the impurities present a real excluded volume for the surrounding dielectric.

CHAPTER 4

Luminescence of europium complexes in alcohols

The criteria for selecting a suitable luminescent system, that is the radiating molecule plus dielectric host, to study local-field effects on spontaneous emission are discussed, resulting in the choice for europium complexes dissolved in alcohols with varying refractive indices. The luminescence quantum efficiency plays an important role in comparing the experimental results to the theory of the previous chapter, and is hence considered in more detail. Experimental results are presented on Eu(hfc)$_3$ in (deuterated) methanol, and on Eu(fod)$_3$ in a series of (deuterated) alcohols and mixtures hereof. The hfc-complex turns out to be chemically unstable in methanol, whereas Eu(fod)$_3$ is stable in alcohols, making the latter more suitable. Unfortunately, small variations in the local environment of Eu(fod)$_3$ complex upon changing the host (alcohol), blur most of the local-field effect on spontaneous emission.

4.1 How to measure local-field effects on spontaneous emission?

In the previous chapter, spontaneous emission of an impurity dipole inside a dielectric was predicted to depend on local-field factors. The resonance frequency, see Eqs. 3.9 and 3.14, was shown to shift slightly to the red, with increasing dielectric constant of the medium. The spontaneous emission rate was demonstrated to depend more strongly on the dielectric constant, see Eqs. 3.11 and 3.16. How would one observe such effects experimentally?

First of all, in the theoretical description some assumptions were made, which need to be discussed more thoroughly. The polarizable impurity dipole in the model has only one resonance, *i.e.* it is a two-level system. In nature, most molecules show spontaneous emission from many levels. Furthermore, the impurity is forced to obey the optical theorem. This means that once the impurity is in the excited state, it will always decay to the ground state by emission of a photon. In other

words, the quantum efficiency for resonant luminescence equals 1 (100 %), *i.e.* the excited impurity is not allowed to decay to the ground state via non-radiative processes. However, nearly all excited molecules also decay via non-radiative relaxation, complicating the comparison of experiments with theory. Last, but not least, the radiative decay rate Γ_0 of the impurity in vacuum is assumed to be a fixed parameter, independent of any variations in the dielectric constant of the host. This implies that the electronic wavefunctions involved in the luminescent transition of the impurity are unaffected by changing the environment. This requirement on the electronic wavefunctions is a stringent selection criterion on which type of impurity can be used for testing local-field effects on spontaneous emission.

The type of experiment one likes to perform is measuring the radiative properties of an impurity, both the emission spectra as well as luminescence decay, in host material with variable dielectric constant, or, equivalently, variable refractive index [see section 2.5]. The variation in refractive index is most easily obtained by using liquids, and simply changing the type of liquid. In order to compare with the theoretical description, in which the dielectric constant was taken to be real, the liquids used in the experiment have to be transparent, *i.e.* non-absorbing, in the wavelength region in which the impurities emit their radiation.

4.2 The ideal system

The ideal system to measure local-field effects on spontaneous emission consists of an impurity with a resonant luminescence quantum efficiency of 1, and transition matrix elements independent of the varying surrounding refractive index.

Standard fluorescing organic dye molecules are then immediately discarded, as their optical properties are highly sensitive to changes in the chemical properties of the environment [56]. This is mainly due to the fact that the electronic wavefunctions involved in the radiative transitions have a high electron densities close to the edges of the dye molecule, making these wavefunctions very susceptible to changes in the local environment. As a result, not only the transition matrix elements change, but also the resonance frequencies and fluorescence quantum efficiency. So, what is needed is a luminescent impurity in which the electronic wavefunctions involved are well shielded from the surrounding.

Lanthanide, or rare earth, ions show luminescence from 4f *intra*-shell transitions. These transitions are well shielded from the environment by the outer electrons, making them good candidates for the experiment. However, the luminescence quantum efficiency for many lanthanides can be low, posing a real drawback. Furthermore, the luminescence spectra of lanthanides exhibit many sharp emission bands, which is an indication that more than one resonance is important, compli-

cating the interpretation. Despite these drawbacks, lanthanides are still a far better choice than organic dyes, for which chemical effects are nearly uncontrollable. Proper complexation of a suitable rare earth ion, and careful selection of the dielectric host, can result in a near ideal system.

4.3 Europium-complexes

4.3.1 Lanthanide metals

The lanthanide, or rare earth, metals that follow lanthanum in the Periodic Table (atomic number 58-71), are the fourteen elements in which the fourteen 4f electrons are successively added to the lanthanum configuration ($[Xe]4f^0 5d^1 6s^2$). The characteristic valence for lanthanide ions is 3+, but Ce can have oxidation number 4+, and for Sm, Eu, and Yb 2+ is also possible. In principle, the number of donor atoms in the first coordination sphere can vary from six to twelve, but eight and nine are most common. The 4f intra-shell electrons are shielded from the environment by the outer core 5s and 5p electrons, and are therefore minimally involved in bonding. As a consequence, the luminescence properties of rare earth metal ions are almost unaltered after complex formation with different encapsulating ligands [57]. Furthermore, the primary coordination number and complex geometries are nearly entirely determined by the ligands, instead of the lanthanide ion. It should be noted that the lanthanide ions show a strong tendency to bind water. Therefore, it is essential to use negatively charged ligands for suitable lanthanide complexation, but complete stripping of water molecules is nearly impossible [58].

The energy diagram The energy levels of multiple electron configurations are usually expressed in the Russell-Saunders coupling scheme [59], using the symbol ${}^{(2S+1)}L_J$, in which L is the total orbital angular momentum, S the total spin of the electrons, and J the total angular momentum quantum number. The *order* of the energy levels is given by Hund's rules [59]. In this energy level diagram, electrons can exchange between different energy levels, which is accompanied by either the uptake or release of energy, *i.e.* absorption or emission of light, respectively. The selection rules [59] determine which electric dipole transitions are allowed.

In principle, the Russell-Saunders coupling scheme is only valid when spin-orbit coupling is weak, *i.e.* in the case of low atomic numbers. Otherwise, the quantum numbers S and L loose their relevance, and the selection rules fail. According to these selection rules, the transitions between two levels with the same parity are not allowed ($\Delta S \neq 0$), which implies that the f-f transitions of lanthanide ions are in principle parity forbidden. However, the existence of spin-orbit coupling in these atoms make that the f-f transitions become more allowed, and hence

do occur. In addition, the transition can also become allowed through the mixing of wavefunctions, caused by a non-centrosymmetric crystal or ligand field, quantitatively described by Judd-Ofelt theory [60]. In general, precise calculations concerning the energy level diagram of lanthanide ions are complicated, and to simplify these, the Russell-Saunders coupling scheme is applied despite the presence of significant spin-orbit coupling.

Roughly speaking, the energy level diagram is determined by different interactions, and is subdivided in terms with separations of the order of 10^4 cm^{-1} by the electrostatic interaction, and a typical splitting of 10^3 cm^{-1} as the result of spin-orbit coupling. Finally, in lanthanide ion complexes, the ligand field partially or fully removes the degeneracy of the J-levels, with splittings of the order of 10^2 cm^{-1} [61].

The emission bands in the luminescence spectra of lanthanide ions are relatively sharp. Due to the low transition probabilities, the luminescence decay times are relatively long, in the microsecond to millisecond range. For comparison, note that the fluorescence decay times in organic dye molecules are in the nanosecond regime. The splitting of the energy levels of rare earth ions results in many possible transitions between different states after excitation of the ion. Therefore, the emission spectrum of a lanthanide ion consists of a series of distinct frequencies, each corresponding to the transition from the lowest excited state to one of the sublevels of the ground state; these frequencies are characteristic for each ion. The chemical properties of lanthanide ions may be quite similar, but their luminescence properties differ quite significantly. On the basis of photo-physical considerations, lanthanide ions can be subdivided in the following three groups [62]:

1. La^{3+} and Lu^{3+} do not exhibit luminescence due to the empty and filled 4f shell, respectively.

2. Ce^{3+}, Pr^{3+}, Nd^{3+}, Pm^{3+}, Ho^{3+}, Er^{3+}, Tm^{3+}, and Yb^{3+} show weak luminescence. The energy difference between the lowest excited state and the highest level of the ground state is relatively small, making deactivation via non-radiative decay quite efficient.

3. Sm^{3+}, Eu^{3+}, Gd^{3+}, Tb^{3+}, and Dy^{3+} show strong luminescence due to their relatively large energy gaps of 7400, 12300, 32000, 14200, and 7850 cm^{-1}, respectively. Note that Gd^{3+} is difficult to excite due to the large energy gap, but once it is excited, it has a quantum efficiency very close to 1 for all sorts of host materials [63].

The Eu^{3+} ion From all lanthanides, especially Eu^{3+} ([Xe]4f^6 configuration) is famous for its luminescence properties. For example, the red phosphor in fluores-

cent strip lamps is Eu^{3+} [64]. The main luminescence transitions of Eu^{3+} occur between the $^5D_0$ state and the ^7F_j levels ($j = 0,1,...,6$), of which the $^5D_0 \rightarrow {}^7F_5$ and $^5D_0 \rightarrow {}^7F_6$ transitions are usually very weak. For Eu^{3+} ions in a highly centrosymmetric environment, the luminescence mainly occurs through the $^5D_0 \rightarrow {}^7F_1$ magnetic dipole transition. This transition is relatively insensitive to changes in the symmetry. However, for Eu^{3+} ions in a highly non-centrosymmetric environment, that is when the crystal or ligand field strongly perturbs the central ion, the electric dipole transitions $^5D_0 \rightarrow {}^7F_{0,2,4}$ are dominant.

The main advantage of using Eu^{3+} as an impurity dipole to test local-field effects on spontaneous emission is the non-degeneracy of the $^5D_0$ level. Consequently, the luminescence emission spectra are relatively uncomplicated and the luminescence decay rate is equal for all $^5D_0 \rightarrow {}^7F_j$ transitions. Furthermore, the luminescence quantum efficiency of Eu^{3+}-complexes dissolved in liquids can be relatively high, provided suitable ligands and solvents are used [57].

4.3.2 Sensitized emission

As a consequence of the parity forbidden transitions within the 4f shell of the lanthanide ions, the resonant light absorption is low. Characteristic values for the molar absorptivity are of the order of 1-10 $M^{-1}cm^{-1}$. Therefore, large interest exists in sensitized emission, using a chromophoric group as an antenna that efficiently delivers the energy, leading to the excitation of the coordinated lanthanide ion. The chromophore or sensitizer can be present in solution, directly coordinated to the lanthanide ion, or covalently attached to an organic ligand that also binds the lanthanide. The latter is the case for rare earth ligand complexes. The generally accepted energy diagram for sensitized emission is schematically depicted in Fig. 4.1. The first step involves the absorption of light by the sensitizer, ligand, which has a relatively high absorptivity, leading to excitation from the ground singlet state S_0 to one of the vibrational states S_1. The molecule rapidly (0.1 - 1 ps) [65] loses the excess vibrational energy via non-radiative decay, falls back to the lowest level of S_1, and stays there for several nanoseconds [65]. At this stage, two alternative routes are available. The molecule can either deactivate by a radiative transition from S_1 to S_0 (prompt ligand fluorescence), or undergo a transition to the triplet state T (inter-system crossing). From the triplet state, the molecule can return to the ground state by means of a spin-forbidden transition (phosporescence), or the energy can be transferred to an appropriate 4f level of the lanthanide ion, here Eu^{3+}. After the loss of excess energy via non-radiative processes (internal conversion), the luminescent state of the ion becomes populated (for Eu^{3+} the $^5D_0$ level). The ion is now ready to luminesce (emit light), but it can also deactivate via non-radiative decay (not shown) to the ground state. For optimal luminescence, the prompt ligand

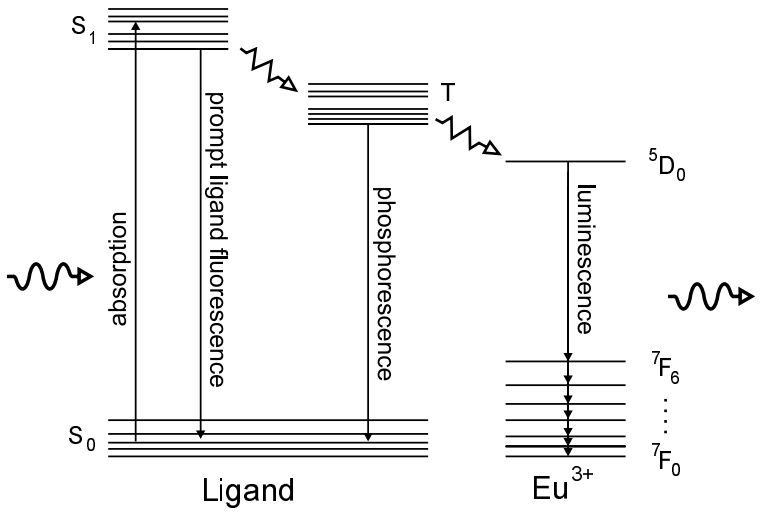

Figure 4.1 The schematic energy diagram of sensitized emission of Eu^{3+}. The optical excitation process of the central lanthanide ion is described in the text.

fluorescence, the phosphorescence, and the non-radiative deactivation of the luminescent level should be minimized. On the other hand, the inter-system crossing and the energy transfer from the ligand to the lanthanide ion should be efficient.

4.3.3 $Eu(fod)_3$ and $Eu(hfc)_3$

Several commercially available Eu^{3+}-complexes were tested for their applicability to use in the experiments to probe local-field effects on luminescence. In this chapter, only two will be described: $Eu(fod)_3$ [66] and $Eu(hfc)_3$ [67], see Fig. 4.2, which are representative for the entire series tested. $Eu(fod)_3$ is a β-diketone ligand complex, which usually have one H_2O molecule positioned in the first coordination sphere [57] (not shown in Fig. 4.2). $Eu(hfc)_3$ is a camphorate. As already mentioned, the non-centrosymmetric ligand field produced by the surrounding ligands strongly determine the matrix elements of the 4f intra-shell transitions of the Eu^{3+} ion [60]. In other words, the symmetry, or equivalently crystal structure, of the ligands determine the transition probabilities. Consequently, every complex has a different vacuum radiative lifetime Γ_0, and cannot be compared in that respect. In both complexes, the ligands not only serve to enhance the luminescence efficiency, but also to shield the 4f intra-shell transitions from unwanted effects caused by the environment.

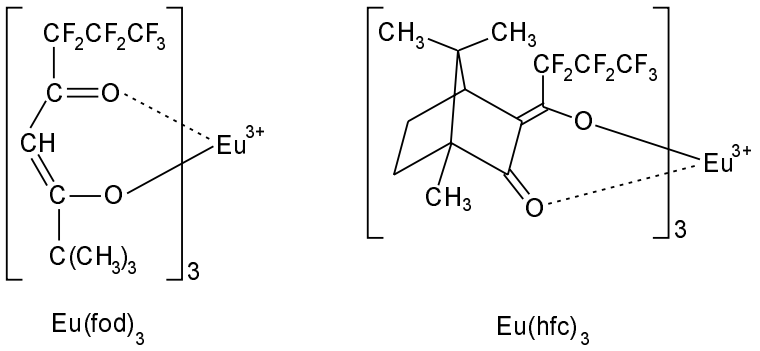

Figure 4.2 The structure formulas of two Eu-complexes used in the experiments: $Eu(fod)_3$ and $Eu(hfc)_3$.

4.4 The dielectric host

Rare earth complexes dissolve well into polar liquids. In the experiments done by Rikken and Kessener [54], who also used Eu^{3+}-complexes to test local-field effects on spontaneous emission, the polar liquids used to vary the refractive index were of different chemical nature. When trying to reproduce their results, it was found that the choice of solvent is crucial. The optical properties of the 4f intra-shell transitions in Eu^{3+}-complexes can vary enormously by dissolving it in chemically different liquids, although seemingly the complex shields the rare earth ion from the environment. For example, the emission spectra may change, indicative that the symmetry of the ligand field changes. Accordingly, the transition matrix elements, or equivalently Γ_0 in Eqs. 3.11 and 3.16, change. Furthermore, the luminescence quantum efficiency depends on the type of liquid. It was found that the luminescence lifetime of a particular complex could vary over an order of magnitude by only dissolving it into chemically different liquids, without changing the refractive index. Such effects may completely blur the observation of local-field effects on spontaneous emission. Nevertheless, Rikken and Kessener [54] succeeded to confirm the empty-cavity model [Eq. 3.11]. However, due to the above described problems, their results should be interpreted with care.

In order to improve on the method used by Rikken and Kessener, in the experiments described here, the refractive index is changed by using a chemically homologic series of simple alcohols. The alcohols used are $CH_3(CH_2)_nOH$, with n ranging from 0 for methanol (MeOH) to 9 for 1-decanol (DeOH). Accordingly, the refractive index varies from 1.33 to 1.44. To test the influence of the intrinsic molecular vibrations of the alcohols on the luminescence properties, also deuterated al-

cohols are used: $CH_3(CH_2)_nOD$, with $n = 0, 1, 3$. The refractive index of a deuterated alcohol is identical to a normal one. Furthermore, their chemical properties are identical, as also their size (trivial as this may seems, the size of the molecule will turn out to be an important parameter). So indeed, only the importance of the OH/OD stretching vibration is investigated by comparing the luminescence of the Eu^{3+}-complex in normal and deuterated alcohols.

4.5 The luminescence quantum efficiency

The luminescence quantum efficiency Q of a material is in general defined as the ratio of the number of emitted photons to the number of absorbed photons. For a single luminescing molecule, this resides to the probability that upon optical excitation indeed it decays radiatively. Consequently, the quantum efficiency is directly related to all the different deactivation mechanisms present.

The quantum efficiency depends on the wavelength of excitation. For example, if Eu^{3+} is resonantly excited in the $^5D_0$ level the quantum efficiency is larger than upon excitation via the surrounding ligand, since the probability of energy transfer from the ligand to the $^5D_0$ level is less than unity, see Fig. 4.1. Nevertheless, sensitized emission does strongly enhance the luminescence intensity, but this is solely due to the higher absorptivity and not due to a higher quantum efficiency. For the experiments concerning local-field effects on spontaneous emission, only the resonant quantum efficiency is important, that is the ratio of the radiative decay rate Γ_R to the total decay rate $(\Gamma_R + \Gamma_{NR})$ from the $^5D_0$ level,

$$Q = \frac{\Gamma_R}{\Gamma_R + \Gamma_{NR}}. \tag{4.1}$$

Here, $\Gamma_R = \sum_j \Gamma_{R,^5D_0 \rightarrow ^7F_j}$ is the total radiative decay rate of all transitions from the $^5D_0$ level to the ^7F_j multiplet, and Γ_{NR} the total decay rate of the competing non-radiative relaxation processes. The experimentally observed luminescence decay time τ_{obs} is determined by the total decay rate, $\tau_{obs}^{-1} \equiv \Gamma_{obs} = (\Gamma_R + \Gamma_{NR})$.

In the classical theory of spontaneous emission, the optical theorem is employed to relate the resonant extinction cross-section to the total scattering cross-section, implying that no energy is lost via non-radiative decay. So, in order to compare experiments with the theory on local-field effects, which thus only describes the dependence of Γ_R on the refractive index of the host material, either the quantum efficiency should be 1, or the quantum efficiency should not depend on the refractive index, as

$$\Gamma_{obs} = Q^{-1}\Gamma_R. \tag{4.2}$$

Here, it is assumed that all transitions $^5D_0 \rightarrow {}^7F_j$ follow the same dependence on refractive index. This assumption is valid, when the ligand field strongly perturbs the central Eu^{3+} ion, so that all $^5D_0 \rightarrow {}^7F_j$ are of electric dipole nature [68].

In general, it makes no sense to compare radiative decay rates to the observed luminescence decay rates without discussing non-radiative decay.

4.5.1 Non-radiative decay via multi-phonon relaxation

The non-radiative decay process for large energy gap lanthanide ions, like Sm^{3+}, Eu^{3+}, Gd^{3+}, Tb^{3+}, and Dy^{3+}, in crystalline or glassy host materials is governed by multi-phonon relaxation [63, 69]. Experimentally it is well-known that the non-radiative decay rate Γ_{NR} of all rare earth ions in one host obey the exponential energy gap law

$$\Gamma_{NR} = \beta \exp[-\alpha \Delta E], \tag{4.3}$$

with constant α and β, and where ΔE is the electronic energy gap between the 4f levels. As can be seen from Eq. 4.3, the larger the energy gap ΔE, the smaller Γ_{NR}, since then larger numbers of phonons are involved in the non-radiative relaxation, making the process less probable. Therefore, non-radiative decay processes mainly occur via relaxation to the most energetic phonons with corresponding energy $\hbar\omega_{max}$, so that the number of phonons involved in the transition is minimized ($\Delta E/\hbar\omega_{max}$ is minimized). The parameter α is reasonably constant for a wide variety of materials, that is $\alpha = (4.5 \pm 2) \cdot 10^{-3}$ cm^{-1}. Whereas, the so-called electronic factor β varies over 5 orders of magnitude for different host materials, obstructing a unifying description for lanthanide ions in host materials.

Van Dijk and Schuurmans [69] resolved the problem of variation in β, and found theoretically that

$$\Gamma_{NR} = \beta_{el} \exp[-\alpha(\Delta E - 2\hbar\omega_{max})] = \beta_{el} \exp[-\gamma(p-2)], \tag{4.4}$$

where β_{el} is the true electronic factor, γ a constant in the range 1-5 [63], and $p = \Delta E/\hbar\omega_{max}$ the minimum number of phonons involved. Now β_{el} varies only over less than an order of magnitude, and $\beta_{el} \simeq 10^7$ s^{-1}. The electronic factor β_{el} contains the electronic coupling element, which contains all the information on how the local environment is organized. The exponential behavior of Γ_{NR} is due to the vibrational overlap [63, 70]. In general, the radiative decay rate is approximately equal to the non-radiative decay rate when 6 phonons are involved [63]. For transitions involving less than 6 phonons, the non-radiative mechanism wins and the rare earth ion has a low luminescence quantum efficiency. Oppositely, when more than 6 phonons are needed, the emission is predominantly radiative.

The local environment plays an important role in non-radiative relaxation. For rare earth ligand complexes, the local environment is mostly defined by the ligand itself. The combination of the type, number, and position of acceptor oscillators determine the non-radiative decay rate. Under the assumption that all acceptor oscillators, *i.e.* molecular vibrations, contribute independently to the non-radiative relaxation, Eq. 4.4 can be written as

$$\Gamma_{\mathrm{NR}} = \sum_j \beta_j \exp\left[-\gamma(p_j - 2)\right]. \tag{4.5}$$

Here, the sum runs over all local acceptor oscillators j, β_j is the electronic factor for each j, and p_j the number of vibrations involved in the deactivation via oscillator j. In Eq. 4.5, decay mechanisms via combinations of different types of oscillators are neglected. Most often this is not a drawback, as the largest contribution to Γ_{NR} arises from the most energetic oscillators. The electronic factor β_j depends on the distance R_j of the oscillator j to the lanthanide ion: $\beta_j \propto 1/R_j^6$, similar as in Förster type dipole-dipole coupling [65]. For example, the contribution to Γ_{NR} of an oscillator in the first coordination sphere is about an order of magnitude larger than of an identical oscillator in the second coordination sphere [71]. Therefore, most often only the contributions of the first coordination sphere are considered. However, it should be stressed that for complexes in which the first coordination sphere consists of only low energetic oscillators, the main contribution of non-radiative decay may originate from the presumably high energetic oscillators in the second coordination sphere. In summary, in order to obtain a lanthanide ligand complex with a high luminescence quantum efficiency, the molecular vibrations inside the complex, close to the central lanthanide ion, must have low resonance frequencies compared to the frequency gap of the rare earth ion.

4.5.2 Non-radiative decay via O-H vibrations

Usually, non radiative decay, or quenching, via O-H vibrations is the most important deactivation pathway [58, 61], as the O-H stretch mode is highly energetic: $\hbar\omega_{\mathrm{OH}} \simeq 3400\ \mathrm{cm}^{-1}$, see Fig. 4.3. The deactivation by O-H vibrations was extensively studied in the mid 1960s. Most of the luminescence studies used Tb^{3+} and Eu^{3+} ions, the luminescence of which can be easily detected, because of their relatively high quantum efficiency. The high efficiency is a direct consequence of the large energy gap between the luminescent excited state and the ground state, as predicted by the theory of multi-phonon relaxation for non-radiative decay. Kropp and Windsor [72] were the first to show that the luminescence lifetimes of the $^5D_4$ level of Tb^{3+} and the $^5D_0$ level of Eu^{3+} ions in D_2O are significantly longer than in H_2O. The effect was explained by the larger number of energy quanta needed to match

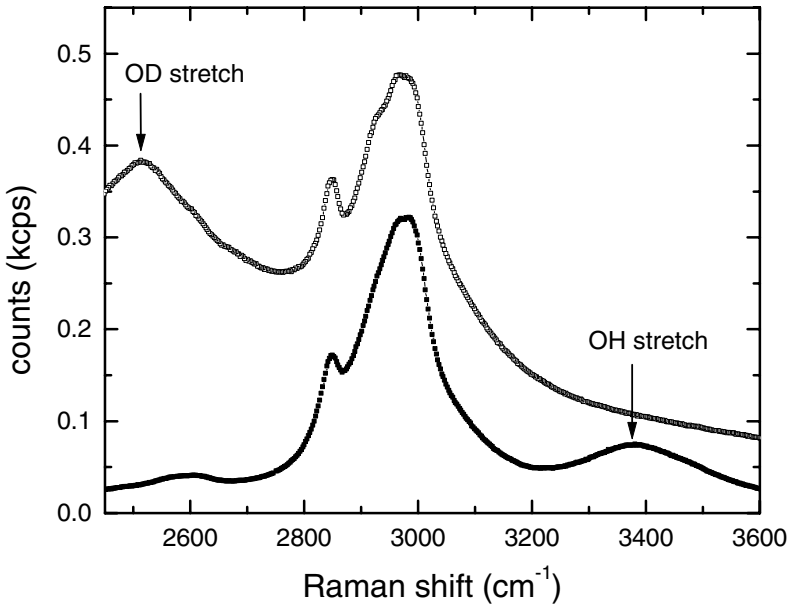

Figure 4.3 Stokes Raman spectra of pure methanol, CH_3OH (MeOH), and deuterated methanol, CH_3OD (MeOD), the filled and open squares, respectively. For MeOH the O-H stretch mode is observed around 3400 cm^{-1}, whereas the O-D stretch mode in MeOD is located at 2500 cm^{-1}. This shift is known as the isotope effect and is due to the difference in mass of the oscillators. The central peak at 2950 cm^{-1} originates from the C-H vibrations. The measurements were done by M. van der Voort [73].

the energy gap in D_2O, see Fig. 4.3. Furthermore, the Eu^{3+} ions are more affected than the Tb^{3+} ones, due to the smaller energy gap between the lowest excited state and the highest level of the ^7F_j ground state multiplet, 12500 cm^{-1} ($^5D_0 \rightarrow ^7F_6$) compared to 14200 cm^{-1} ($^5D_4 \rightarrow ^7F_0$), respectively.

Kropp and Windsor subdivided Γ_{NR} in: (1) a rate constant for quenching by deuterated vibrations; this contribution is usually small and neglected, (2) a rate constant for quenching by O-H vibrations, and (3) a rate constant for quenching via the remaining pathways. They performed lifetime measurements in D_2O with different mole fractions of H_2O and found that the non-radiative decay increased linearly with the mole fraction of O-H oscillators. This indicates that indeed the oscillators can be treated independently, validating the assumption made to derive Eq. 4.5.

Horrocks and Sudnick [58] performed similar experiments on systems in which lanthanide ions are encapsulated by (bio)organic ligands. The combination of (1)

the estimated number of coordinating water molecules of many different complexes in aqueous solutions, and (2) the differences in luminescence decay rates of these complexes when dissolved in D_2O and H_2O, lead to the by now well-known *Horrocks* equation,

$$n = q(\Gamma_{H_2O} - \Gamma_{D_2O}). \tag{4.6}$$

Here, n is the number of O-H (or O-D) oscillators in the first coordination sphere, Γ_{H_2O} and Γ_{D_2O} the observed luminescence decay rates in H_2O and D_2O in ms^{-1}, and q = 2.1 ms for Eu^{3+} and 8.4 ms for Tb^{3+}. The estimated number of O-H oscillators in the first coordination sphere using the Horrocks equation is in good agreement with the number inferred from the crystal structure obtained via X-ray measurements, with an uncertainty of approximately 1 O-H oscillator.

The Horrocks equation is directly related to the multi-phonon relaxation described by Eq. 4.5. As will be shown below, the experimental values obtained by Horrocks and Sudnick determine the parameters β and γ in Eq. 4.5. As $\Gamma_{NR,OD} \ll \Gamma_{NR,OH}$ and thus $\Gamma_{H_2O} - \Gamma_{D_2O} = \Gamma_{NR,OH} - \Gamma_{NR,OD} \simeq \Gamma_{NR,OH}$, Eq. 4.6 readily gives the contribution to the non-radiative decay of an O-H oscillator: $\Gamma^{Eu}_{NR,OH} \simeq 1/(2.1)$ ms^{-1} = 0.47 ms^{-1} and $\Gamma^{Tb}_{NR,OH} \simeq 1/(8.4)$ ms^{-1} = 0.12 ms^{-1} for each O-H oscillator in the first coordination sphere of Eu^{3+} and Tb^{3+}, respectively. The smaller rate for Tb^{3+} as compared to Eu^{3+} is due to the larger number of vibrations needed to bridge the energy gap, see Eq. 4.5: $p_{Tb} \simeq 14200/3400 = 4.2$ and $p_{Eu} \simeq 12500/3400 = 3.7$, for Tb^{3+} and Eu^{3+}, respectively . Furthermore, the electronic factor β from Eq. 4.5 is independent of the type of lanthanide ion, so that the non-radiative decay rates obtained from the Horrocks equation can be linked to the theory of multi-phonon relaxation [Eq. 4.5],

$$\Gamma^{s}_{NR,OH} = \beta \exp[-\gamma(p_s - 2)], \tag{4.7}$$

where s = Eu, Tb [Eq. 4.5]. Given these two equations and using the experimental values Horrocks obtained, the parameters β and γ are determined: $\beta \simeq 8 \cdot 10^4$ s^{-1} and $\gamma \simeq 3$. The value obtained for γ is in good agreement with the range of values known for lanthanides in crystalline or glassy hosts, there γ = 1-5, whereas β is about two orders of magnitude low [63, 69]. However, here only the quenching of 1 O-H oscillator is investigated, when in fact 10 H_2O molecules [62] coordinate Eu^{3+} (or Tb^{3+}) in water. So the collective contribution of all 20 O-H oscillators leads to an electronic factor of $20 \cdot \beta \simeq 1.6 \cdot 10^6$ s^{-1}, which is in good agreement with $\beta_{el} \simeq 10^7$ s^{-1}, given the approximations made. This establishes the connection between the theory of multi-phonon relaxation and the Horrocks equation.

4.5.3 Non-radiative decay via other vibrations

Aside from O-H oscillators, other vibrations may contribute to non-radiative decay. Especially the lighter oscillators containing a hydrogen atom are quite efficient in quenching due to their high oscillation frequencies. Examples are the C-H stretch mode with $\hbar\omega_{\mathrm{CH}} \simeq 2950\ \mathrm{cm}^{-1}$ [see Fig.4.3] and the N-H stretch mode, $\hbar\omega_{\mathrm{CH}} \simeq 3500\ \mathrm{cm}^{-1}$. The quenching by an C-H oscillator is less than by O-H oscillator, that is $\Gamma^{\mathrm{Eu}}_{\mathrm{NR,CH}} \simeq 0.09\ \mathrm{ms}^{-1}$ for each C-H oscillator in the first coordination sphere. Oppositely, the non-radiative decay rate via an N-H vibrations is larger than via an O-H oscillator: $\Gamma^{\mathrm{Eu}}_{\mathrm{NR,NH}} \simeq 0.64\ \mathrm{ms}^{-1}$. The quenching by heavier oscillators is much less efficient, and can most often be neglected.

4.6 Experimental

4.6.1 The luminescence set-up

The europium complexes were optically excited in the absorption band of the ligand at 354.7 nm, using the 20 Hz rep. rate pulses of a tripled Nd:YAG laser (Quanta Ray, DCR 2A). The pulses duration was 10 ns, much shorter than the luminescence lifetimes observed. The samples, europium complexes dissolved in alcohols (described below), were contained in 1×1 cm quartz cuvettes (Helma QS-series). Upon optical excitation, the Eu^{3+} ions showed luminescence, which was dispersed by a Spex 1401 double spectrometer (resolution $2\ \mathrm{cm}^{-1}$) and detected with a Hamamatsu R943-02 red-sensitive single-photon counting tube. The luminescence decay rates were in the millisecond range and recorded with a multichannel scaler (EG&G-Ortec, T914); bin width 1 μs, with a maximum range of 16.4 ms (2^{14} bins). For recording luminescence spectra, the PMT signal was fed into the counting card of the computer, which simultaneously controlled scanning of the spectrometer.

4.6.2 The samples

The samples are 1 mmol/l solutions of $Eu(hfc)_3$ and $Eu(fod)_3$ in different alcohols, in which the europium complexes dissolved well. The alcohols were all obtained from Aldrich, with a minimum purity of 99 %. As already mentioned, the alcohols used were $CH_3(CH_2)_nOH$, with $n = 0,...,9$ (but not $n = 6,8$), as also deuterated alcohols $CH_3(CH_2)_nOD$, with $n = 0,1,3$, and mixtures hereof. The refractive indices of the alcohols, and its mixtures, were determined with an Abbe-refractometer (Carl Zeiss).

The concentration of 1 mmol/l corresponds to an average inter-complex distance of 12 nm, or equivalently 40 parts per million (ppm) for MeOH ranging

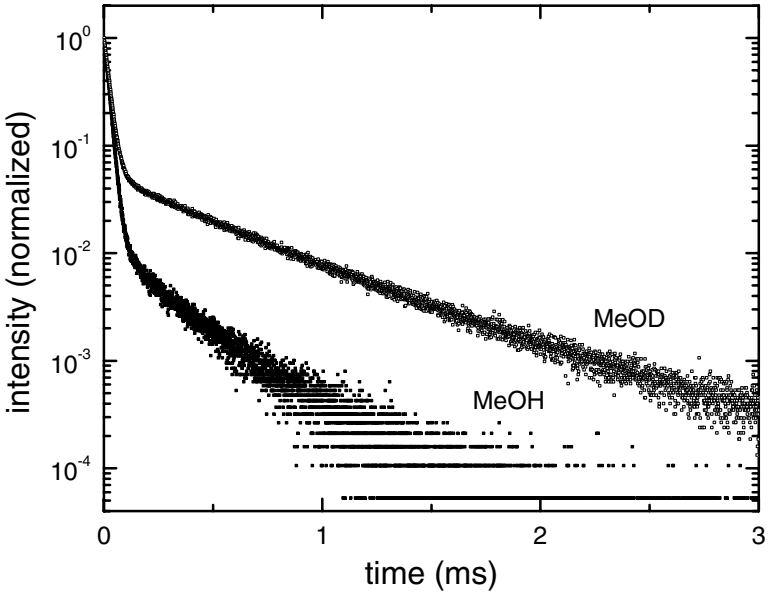

Figure 4.4 Luminescence decay of $Eu(hfc)_3$ in MeOH and MeOD measured at 16360 cm^{-1}. The decay in both liquids consists of two components. MeOH: 22 $\pm$ 1 μs and 0.28 $\pm$ 0.01 ms. MeOD: 27 $\pm$ 1 μs and 0.53 $\pm$ 0.01 ms.

to 220 ppm for DeOH. The concentration is low enough to discard concentration quenching, which was experimentally checked.

The deuterated samples were prepared in a nitrogen purged box, to minimize the water contamination. Furthermore, the deuterated samples were readily measured after preparation (within a half hour), for the same reason.

4.7 Luminescence of $Eu(hfc)_3$ in methanol

The luminescence decay of $Eu(hfc)_3$ in methanol, CH_3OH (MeOH), and deuterated methanol, CH_3OD (MeOD), measured at 16360 cm^{-1}, corresponding to the maximum of the $^5D_0 \rightarrow ^7F_2$ transition, is shown in Fig. 4.4. As can be seen, the decay consists of two components for both MeOH and MeOD, indicating that two different europium species might be present. The luminescence lifetimes for both components are longer in MeOD than in MeOH. The short-living component has lifetimes of 22 $\pm$ 1 μs and 27 $\pm$ 1 μs for MeOH and MeOD, respectively. Likewise, the long-living component yields: 0.28 $\pm$ 0.01 ms (MeOH) and 0.53 $\pm$ 0.01 ms (MeOD). If the components are indeed both stemming from Eu^{3+}

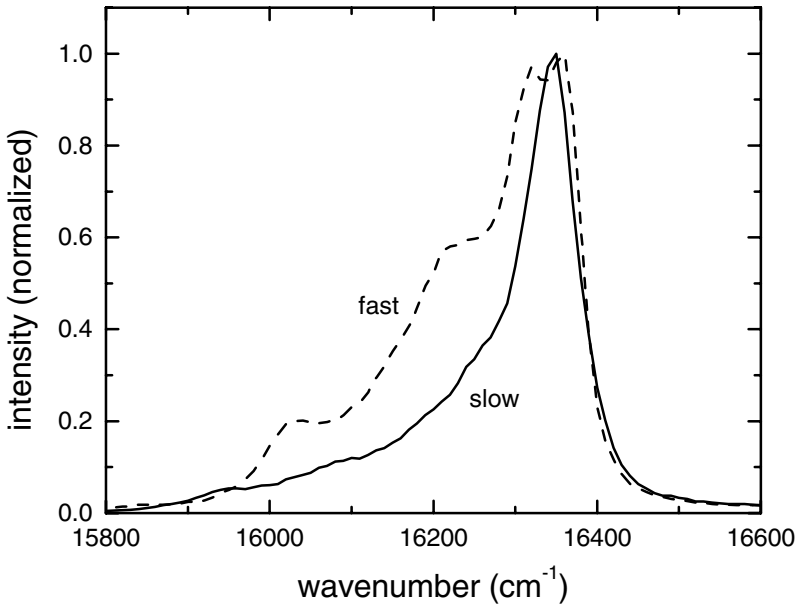

Figure 4.5 The time-resolved luminescence spectra of the fast and slow decaying components of $Eu(hfc)_3$ dissolved in MeOD. Both spectra are characteristic for Eu^{3+} luminescence from $^5D_0$ level to $^7F_2$, proving that both components are europium related. The spectra are similar in MeOH.

luminescence, then the difference in lifetimes between dissolving in MeOH and MeOD gives information on the O-H (O-D) coordination, by use of the Horrocks equation [Eq. 4.6]. However, first both components have to be identified as europium species.

For this purpose, time-resolved luminescence spectra were recorded. This is done by measuring the luminescence decay at different wavelengths. At each wavelength, the decay consisted of two components, similar as in Fig. 4.4. The luminescence lifetimes of both components were found to be independent of wavelength, characteristic for the luminescence from the non-degenerate $^5D_0$ level of Eu^{3+}. The intensities of both components vary with wavelength and represent the time-resolved luminescence spectra, which are displayed in Fig. 4.5 for $Eu(hfc)_3$ in MeOD. From these spectra, it is concluded that both components stem from europium luminescence, both in MeOH and MeOD. The difference in lifetimes of the two components [Fig. 4.4] is the result of different local environments; both the radiative and non-radiative decay rates are different then.

Information on the non-radiative decay can be obtained by exploiting the Hor-

rocks equation, Eq. 4.6; the number of O-H oscillators in the first coordination sphere of the two components can be estimated. For the fast component, the difference in decay rate in MeOH and MeOD gives an estimate of 18 $\pm$ 7 O-H oscillators in the first coordination sphere. For the slow component, this number is 3.5 $\pm$ 0.4. The O-H oscillators present can either be H_2O molecules binded to Eu^{3+} in the complex, or O-H groups from the methanol. Regarding the fast component, the large amount of O-H oscillators close to europium indicates that the "complex" is very open, and many H_2O and/or MeOH molecules are near the central ion; probably the complex is partially or fully dissociated. The slow component is most likely the stable Eu(hfc)$_3$ complex with 2 H_2O molecules located in the first coordination sphere.

In conclusion, Eu(hfc)$_3$ is chemically unstable in methanol, hence the two-component decay. Similar two-component decays were observed for Eu(tfc)$_3$ and Eu(thd)$_3$ in methanol. Therefore, all these complexes are discarded as suitable luminescence probes to investigate local-fields effects on spontaneous emission.

4.8 Luminescence of Eu(fod)$_3$ in alcohols

The luminescence spectrum of Eu(fod)$_3$ in 1-butanol, C_4H_9OH (BuOH), is presented in Fig. 4.6. The spectrum consists of 5 major lines, which are identified as the $^5D_0 \rightarrow {}^7F_j$ transitions of Eu^{3+}, with $j = 0,...,4$. Obviously, the luminescence mainly decays via the $^5D_0 \rightarrow {}^7F_2$ transition, indicating that the fod-ligand field strongly perturbs the Eu^{3+} ion. A direct consequence is that the luminescence is of electric dipole character. In general, a $^5D_0 \rightarrow {}^7F_j$ transition is $(2j+1)$-degenerate. This degeneracy can be removed by the non-centrosymmetric ligand field of the complex. A clear example of this lifted degeneracy is $^5D_0 \rightarrow {}^7F_2$ transition of Eu(fod)$_3$, for which a $(2j+1) = 5$ peak structure is observed. Contrary, the $^5D_0 \rightarrow {}^7F_0$ transition is sharp (FWHM = 15 cm^{-1}), representative for the luminescence for a transition between two non-degenerate levels.

The luminescence spectra of Eu(fod)$_3$ dissolved in different (deuterated) alcohols look all very similar. The only observable difference occurs in the weak $^5D_0 \rightarrow {}^7F_3$ and $^5D_0 \rightarrow {}^7F_4$ transitions. The relative intensities of these transitions, as compared to the other $^5D_0 \rightarrow {}^7F_j$ transitions, and their line shapes are independent of the type of alcohol. However, as shown in Fig. 4.7, the line position does depend on the type of alcohol, with a maximum frequency shift of 70 and 80 cm^{-1} for $^5D_0 \rightarrow {}^7F_3$ and $^5D_0 \rightarrow {}^7F_4$, respectively. Although these transitions only slightly contribute to the total luminescence decay, the shift in the line positions indicates that, regarding the luminescence properties of Eu(fod)$_3$ in alcohols, the series of alcohols is subdivided into two groups. Those alcohols with a refractive index lower

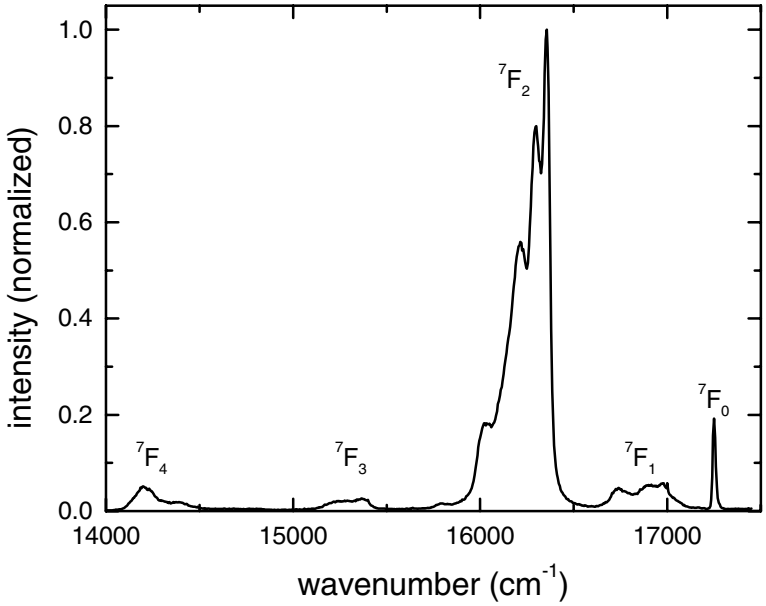

Figure 4.6 The Luminescence spectrum of $Eu(fod)_3$ in BuOH. Five different transitions are observed: $^5D_0 \rightarrow {}^7F_j$, with $j = 0,...,4$. The most intense decay channel is the $^5D_0 \rightarrow {}^7F_2$ transition, indicating that the Eu^{3+} ion is strongly perturbed by the fod-ligand field. Consequently, the radiative decay from the $^5D_0$ level is determined by electric dipole radiation.

than BuOH have identical luminescence spectra, as also those with a higher refractive index. The origin of this subdivision is not clear at this point, and will be discussed in more detail later in section.

The luminescence decay of $Eu(fod)_3$ in BuOH measured at 16360 cm^{-1} is displayed in Fig. 4.8. In contrast with the other europium complexes studied, the decay is single exponential, indicating that only one type of Eu^{3+} complex is present. For all alcohols, and its mixtures, such a single exponential decay of $Eu(fod)_3$ luminescence was observed, making it suitable for the experiment.

The collection of luminescence lifetimes observed for $Eu(fod)_3$ in all different (deuterated) alcohols, and its mixtures, is given in Fig. 4.9. The lifetimes observed for the OD-alcohols are around 850 μs, much longer than $\sim$ 450 μs decay times for OH-alcohols. From this difference, and using the Horrocks equation [Eq. 4.6], the number of O-H (O-D) oscillators in the first coordination sphere is found to be 2.1 ± 0.1. In other words, 1 H_2O molecule is binded to the Eu^{3+} ion in the complex, serving as an efficient quencher.

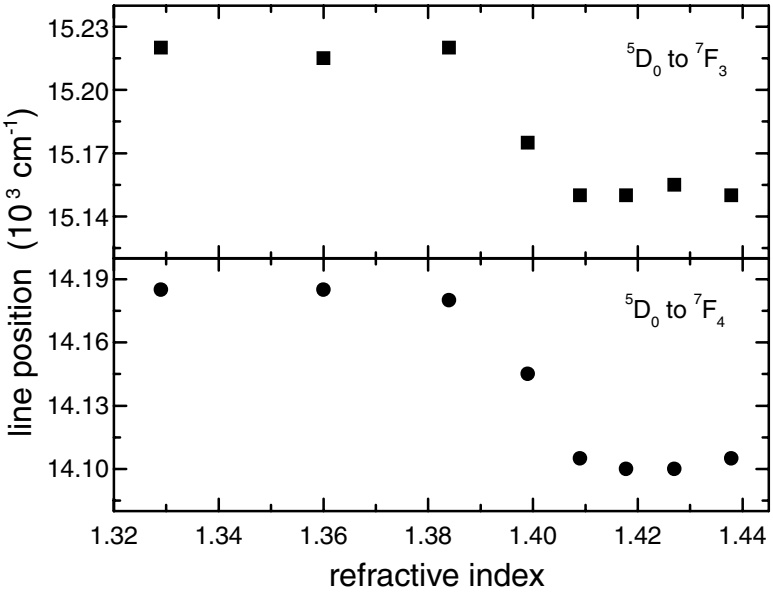

Figure 4.7 The $^5D_0 \rightarrow ^7F_3$ and $^5D_0 \rightarrow ^7F_4$ line positions of Eu(fod)$_3$ dissolved in different pure OH-alcohols, here labeled with their refractive indices. The functional dependence of the line position on refractive index is remarkably similar for both transitions. With respect to the luminescence properties of Eu(fod)$_3$ in alcohols, the homologic series $CH_3(CH_2)_nOH$ can be subdivided into two groups: $n = 0, 1$, and 2 form a group (refractive index $\simeq$ 1.329 to 1.384), and $n = 4, 5, 7$, and 9 (refractive index $\simeq$ 1.409 to 1.438), separated by BuOH (n =3). The error bars are of the order of the symbol size.

Scaling the luminescence lifetimes of Eu(fod)$_3$ in OH- and OD-alcohols with the observed decay times for EtOH and EtOD, respectively, results in an universal curve. This indicates that the scaled lifetimes for both OH- and OD-alcohols can be discussed on the same footing. For alcohols with refractive index lower than 1.40, the luminescence lifetime strongly depends on the type of mixture, and a clear dependence on the refractive index is absent. For alcohols with a refractive index larger than 1.40, the luminescence lifetimes all fall on a single line, representing the functional dependence on refractive index. This clear separation was also observed in the luminescence spectrum for the $^5D_0 \rightarrow ^7F_3$ and $^5D_0 \rightarrow ^7F_4$ transitions, see Fig. 4.7. Note that the separation occurs at exactly the same refractive index of 1.40. Apparently, the europium complex undergoes subtle changes when dissolved in different lower alcohols, whereas these changes are absent for the higher alcohols. This is likely due to the difference in size of the alcohol molecules. Methanol is much smaller than 1-decanol, and thus penetrates more easily into the complex,

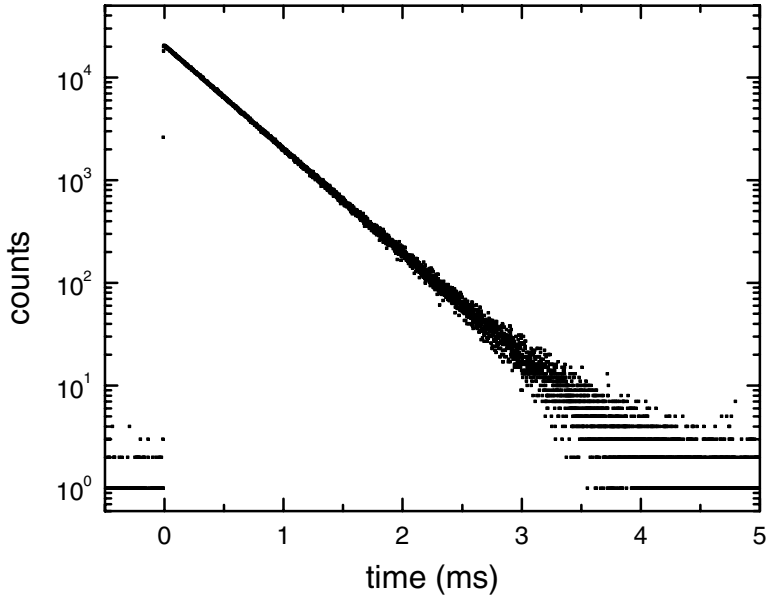

Figure 4.8 The luminescence decay of $Eu(fod)_3$ in BuOH measured at 16360 cm^{-1}. From the single exponential decay a luminescence decay time of 429 $\pm$ 2 μs is inferred.

modifying the local structure. This change in structure of the complex leads to a modification of the radiative and non-radiative decay, observable both in the luminescence spectra and decay measurements. For smaller solvent molecules, the variations will be larger, hence the spread in the luminescence lifetimes at low refractive indices (< 1.40), see Fig. 4.9.

The luminescence quantum efficiency in $Eu(fod)_3$ is higher in OD-alcohols than in OH-alcohols, as readily deduced from the difference in lifetimes, see Fig. 4.9. The efficiencies were independently determined by comparing to a standard solution of 1 mmol/l $Eu(NO_3)_3$ in CH_3OD, which has a known resonant quantum efficiency of 0.79 $\pm$ 0.01 [74]. For this purpose, europium is resonantly excited in the $^5D_2$ level using the 465.7 nm line of an Argon laser (Spectra Physics, 165), in the case of the fod-complex by-passing excitation via the ligands. Comparing the absorption efficiencies of the different solutions, $Eu(fod)_3$ in alcohols and $Eu(NO_3)_3$ in CH_3OD, and the spectrally integrated luminescence intensities, gives the quantum efficiencies. For $Eu(fod)_3$ in OD-alcohols an efficiency of 0.82 $\pm$ 0.09 is found, and in OH-alcohols 0.43 $\pm$0.07. Within the error, the luminescence quantum efficiency is *independent* of the type of alcohol. The relatively large error is due to small amount of absorption, which is hence difficult to determine accu-

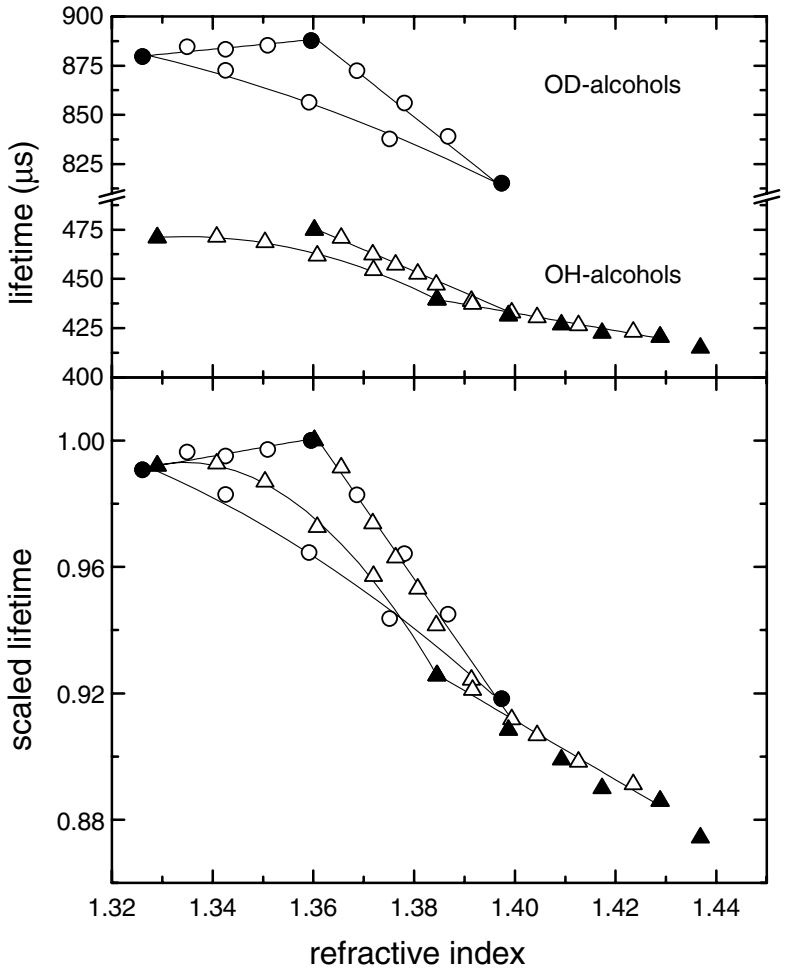

Figure 4.9 *Upper figure:* The luminescence lifetimes of $Eu(fod)_3$ in normal (triangles) and deuterated (circles) alcohols. The solid symbols represent measurements on pure alcohols, the open symbols on mixtures. The following mixtures were used: MeOD/EtOD, MeOD/BuOD, EtOD/BuOD for OD-alcohols, and MeOH/PrOH, EtOH/BuOH, and PrOH/OcOH for OH-alcohols. The solid lines serve to distinguish the different alcohol mixtures. Note that the lifetimes for OD-alcohols are in 800-900 μs range, considerably longer than the lifetimes observed for OH-alcohols (425-475 μs).
Lower figure: The luminescence lifetimes of the upper figure scaled with the lifetimes of $Eu(fod)_3$ in pure EtOH and EtOD for the OH- and OD-alcohols, respectively. The equivalence of the scaled EtOD/BuOD and EtOH/BuOH lifetimes indicates that the scaling results in an universal curve for $Eu(fod)_3$ in alcohols. For alcohols with refractive index lower than 1.40, the luminescence lifetime is *not* solely dependent on the refractive index: for different mixtures with the same refractive index, different lifetimes are found. For alcohols with refractive index higher than 1.40, the lifetimes monotonously decrease with increasing refractive index. The error bars are of the order of the symbol size.

rately. Nevertheless, the measurements prove that the quantum efficiency of europium complexes can be high, close to 1, if dissolved in suitable liquids.

In conclusion, the luminescence lifetime of $Eu(fod)_3$ is a function of refractive index only for the higher alcohols (refractive index > 1.40), even though the system, $Eu(fod)_3$ in a homologic series of alcohols, was carefully selected. Consequently, the range of refractive index variation is too small (refractive index: 1.40-1.44) to compare the experimental result to theoretical models describing local-field effects on spontaneous emission (if one would, the empty-cavity model comes out best, but not very convincingly). It is thus necessary to perform experiments on a different system in which the refractive index can be varied over a larger range, so that indeed local-field effects on spontaneous emission can be revealed.

CHAPTER 5

Local-field effects on spontaneous emission in dense supercritical CO_2

Experiments on the spontaneous emission rate of Eu(fod)$_3$ in dense supercritical CO_2 are presented. The refractive index of the supercritical gas is varied from 1.00 to 1.27 by increasing the pressure up to 1100 bar. Accordingly, the spontaneous emission rate changes. Local-field effects on spontaneous emission are clearly observed in these experiments. The empty-cavity model [see chapter 3, Eq. 3.11] is found to apply, settling the discussion on which local-field correction applies to spontaneous emission.

5.1 Why Eu(fod)$_3$ in supercritical CO_2?

One of the major problems that came up in the previous chapter is that upon variation of the refractive index, the *type* of molecule constituting the dielectric also changes. As a result, local-field effects on spontaneous emission are almost completely blurred. In this chapter, this problem is circumvented by measuring the radiative lifetime of Eu(fod)$_3$ in supercritical CO_2 as function of the pressure of the fluid. Then, the refractive index changes because the density of the molecules in the dielectric changes. The type of molecule, CO_2, remains the same for all refractive indices, improving on the experiments presented in literature [54, 55] and the previous chapter.

The choice for Eu(fod)$_3$ is clear from the previous chapter. From all europium complexes that were tested, it is the only complex that is stable in alcohols. Consequently, it is likely to be also most stable in a supercritical gas. Furthermore, the luminescence quantum efficiency can be close to unity, provided the complex is embedded in a suitable host.

CO_2 is selected for the following reasons. First of all, the CO_2 molecule has a fairly large optical polarizability, so that upon compression high refractive indices

can be obtained, making the range of refractive index variation large. In the spectral region of Eu^{3+} luminescence, from 600 to 800 nm, dense supercritical CO_2 is transparent (non-absorbing), and its refractive index is independent of wavelength (low dispersion) [75]. The luminescence quantum efficiency of $Eu(fod)_3$ in dense CO_2 is indeed expected to be high, a point discussed in more detail later in this chapter. The critical temperature for CO_2, 31.06 °C [76], is conveniently close to room temperature, so that the sample cell only has to be heated slightly. And last but not least, $Eu(fod)_3$ is known to dissolve well into supercritical CO_2 [77].

5.2 The pressure set up

The experiments were performed in a home-built pressure cell with optical access [78]. An extensive discussion on the high-pressure set up is presented, as the system and techniques used are uncommon to most researchers.

5.2.1 The sample cell

The central role of the set up is taken up by the sample cell, which is directly connected to the high pressure system, see Fig. 5.1. The hart of the sample cell is formed by a 15 mm long, synthetic-sapphire cylinder (custom-made by Melles Griot), with an outer diameter of 24.98 mm and a 6.285 $\pm$ 0.005 mm bore, as determined by a three-point measurement. Having a hardness comparable to that of diamond, sapphire can withstand pressures over a 1000 bars. The sample volume is defined by the bore of the sapphire cylinder, which is enclosed between two stainless steel caps at the flat-end sides. The caps are made to fit closely around the sapphire cylinder with a margin of at most 0.02 mm in order to keep the O-rings (Eriks, BN8) from extruding at high pressures. These O-rings close the cell.

The supercritical gas enters and leaves the cell by means of a 4 meter long, 0.18 mm bore stainless steel capillary, which is cold-welded to the upper steel cap. The other end of the capillary is attached to the gas compressor.

The temperature of the cell is measured close the sample volume, using a standard wire-wound Pt resistance thermometer of 100 Ohm (at 0 °C). The sample cell is placed inside a large cylindrical aluminum block (height = 420 mm, diameter = 150 mm); the temperature is regulated by controlling the current through a coil heating the aluminum block. The long-term stability of the temperature is about 50 mK. Although no thermocouples were placed to measure the temperature gradient, similar experiments with the same set up have shown that the gradient is less than 1 mK/cm [78]. During the experiments, the temperature of the supercritical CO_2 was kept at 35.00 $\pm$ 0.05 °C, a few degrees above the critical temperature.

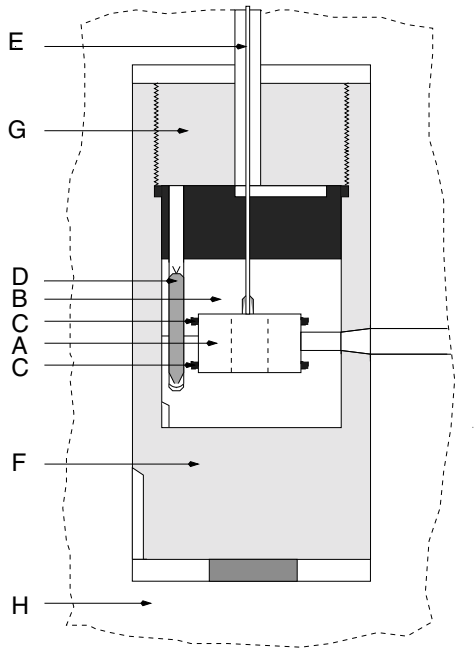

Figure 5.1 An overview of the sample cell. The sapphire cell (A) is enclosed by two stainless steel caps (B) with rubber O-rings (C). The caps are placed in a copper cylinder (F), which is screwed tight with a copper screw piece (G). Next to the sapphire cell, a hole is drilled, housing a Pt thermometer (D). The supercritical gas enters and leaves the cell through a 0.18 mm bore stainless steel capillary (E). The entire sample cell is kept in an aluminum thermostat (H).

Filling the cell with Eu(fod)$_3$ The sample cell can be completely taken apart, which is necessary to load it with a few grains (~ 0.5 mg $\simeq 0.5$ μmol) of Eu(fod)$_3$ powder. The amount corresponds to a concentration of about 1 mmol/l (similar as in the alcohols solution), provided all Eu(fod)$_3$ dissolves in the supercritical gas.

After filling it, the cell was placed in the aluminum block and the capillary connected to the gas compressor. The air left in the system due to the filling, needs to be cleared. For this purpose, CO_2 (AGA 99.9995%) at 60 bars (vapor pressure of CO_2 at room temperature) was sent into the system. Through diffusion the remaining air mixed with CO_2. By releasing this mixture into the open air, and repeating this process several times, sufficiently pure CO_2 (> 99.99 %) was obtained.

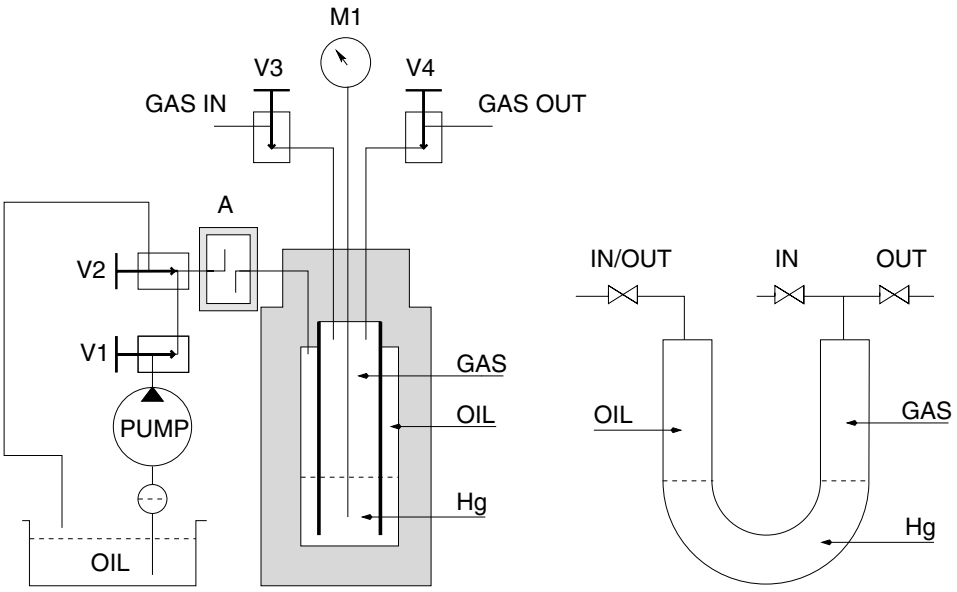

Figure 5.2 A schematic representation of the gas compressor:
[*right:*] The gas compressor can be considered as a U-shaped tube, partly filled with mercury, Hg. Upon compression, oil is pumped in the left side of the tube, compressing the gas on the right side. The mercury serves as a pressure transducer.
[*left:*] A more detailed outline of the compressor. Gas is inserted via valve V3. Valve V4 connects the compressor to the sample cell. By pumping oil from the reservoir into the compressor (V1 open; V2 closed), the volume of the gas is decreased and thus the pressure increased. Visa versa, upon releasing the pressure, V1 is closed and V2 is opened. The indicator (M1) indicates the mercury level in the compressor by measuring the resistance of a Pt-Ir wire, which is extended into the mercury-gas area. The mercury trap (A) is a safety device, which prevents the mercury from entering the pumping system.

5.2.2 The compressor

The compressor serves to vary the pressure of the dielectric fluid, and hence its refractive index. The range of pressures attainable is from 1 bar (ambient pressure) to 1100 bar at which the O-rings are no longer able to withstand the pressure, causing them to burst. Note that the sapphire cylinder can hold pressure up to 1500 bar. However, because of the brittleness of sapphire, it is not able to withstand quick *changes* in pressure ($>$ 10 bar/s).

In simple terms, the gas compressor ('t Hart & Zn.) can be depicted as an U-shaped tube, as shown in Fig. 5.2. The hydraulic liquid (oil) is on one side of the tube, the compressed gas on the other. Mercury acts as a pressure transducer, keep-

ing the oil from contaminating the gas. The valves V3 and V4 lead the gas into or out of the compressor. An electronic mercury-level indicator is attached, helping the experimentalist to prevent the mercury from exiting the compressor, either from the gas or oil side. This indicator consists of a Pt-Ir wire (with known resistivity) that is extended into the mercury-gas area of the compressor. The wire is part of a Wheatstone bridge, and by short-circuiting the resistance of the wire underneath the mercury surface, the mercury level in the compressor is obtained.

The mercury level is increased by pumping (by hand) more oil in the compressor (valve V1 opened and valve V2 closed). In this way, the gas compressor can reach a maximum pressure of 3000 bar. In order to release pressure, valve V1 is closed and valve V2 is opened, so that the oil flows back into the oil reservoir. The mercury trap (A) is a safety device, which prevents the mercury from spilling into the pumping system in case the mercury is accidentally pushed back too much by the pressure of the gas.

5.2.3 Overview of the pressure set-up

During the measurements, pressure was only increased, since a decrease in pressure would in turn decrease the amount of dissolved $Eu(fod)_3$ in the sample cell. Furthermore, allowing the dissolved europium complex to flow with the fluid from the sample cell into the gas compressor, would also contaminate the gas compressor. Therefore, when the measurement series was completed, the fluid was released from the sample cell through a bubble outlet (valve V8 in Fig. 5.3). The outlet facilitates a slow release of pressure, by monitoring the frequency of the gas bubbles. This is necessary to prevent the sapphire window from braking; pressure changes of less than 10 bar/s were required.

In order to obtain high enough pressures, the gas compressor had to be filled with a sufficient amount of CO_2. Therefore, it was necessary not only to transfer CO_2 gas, but also CO_2 liquid from the gas cylinder into the compressor. This was accomplished by using a filling board, as is schematically drawn in Fig. 5.3. The hart of the filling board is the *cold finger*, a volume of 18.4 cc enclosed in stainless steel. Transfer of liquid occurs in two stages. In the first stage, Valves V1, V2 and V3 are opened, and V4, V5 and V6 are closed. The cold finger is cooled down below the freezing point of CO_2, using liquid N_2. When gas from the cylinder enters the cold finger it freezes, resulting in a reduction of pressure. Gas continues to flow in, since the vapor pressure of the cylinder remains at 60 bar. When all the gas inside the cold finger has frozen (when manometer M1 indicates a constant pressure of 60 bar), valves V1 and V2 are closed and V6 is opened (V7 is closed). Upon heating the cold finger, the solid CO_2 melts and pressure builds up rapidly. At a pressure of a 100 bar, valve V5 is quickly opened and gas flows into the compres-

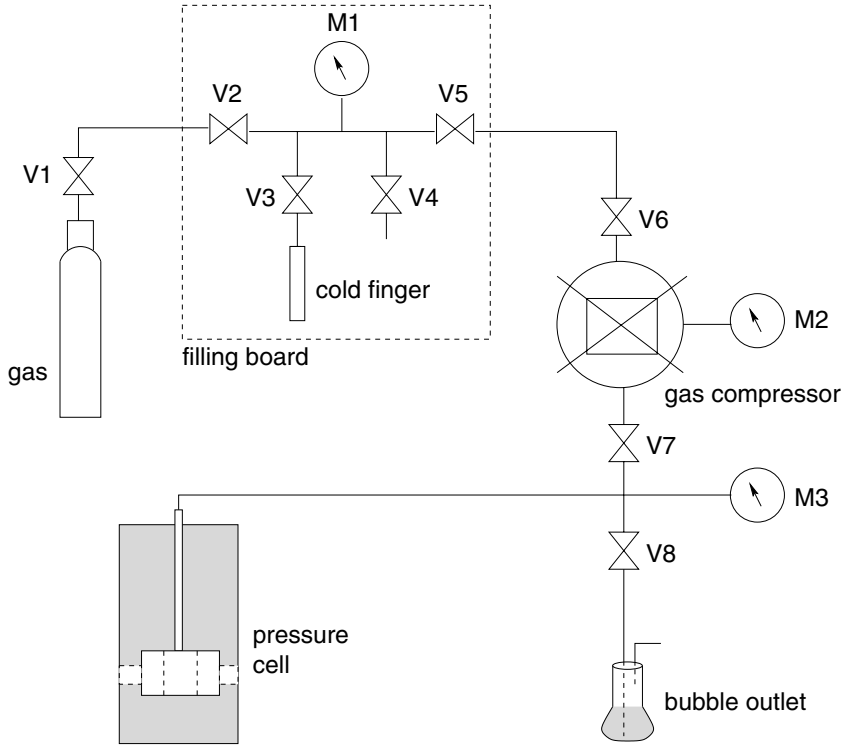

Figure 5.3 An outline of the pressure set up. When filling the gas compressor with gas or liquid, valves V1-V6 are used while valve V7 is closed (see text for procedure). During measurements V6 and V8 are closed and V7 is opened. Manometer M2 gives the pressure of the hydraulic liquid (oil) in the gas compressor, while M3 gives the pressure of the fluid in the sample cell. Upon releasing the high pressure from the sample cell, valve V7 is closed and V8 is opened. The bubble outlet makes it possible to monitor the amount of gas being released.

sor, where it condenses into liquid, as now the temperature of the compressor is lower than of the "cold" finger (due to the heating). Then, valve V6 is closed; the gas compressor is filled with liquid CO_2. This procedure is repeated once more, after which the measurements can commence.

5.3 The refractive index determination

Upon compressing the supercritical gas, the refractive index increases. As the gas is kept at an isotherm of 35 °C close to the critical temperature, a small increase in pressure results in a large increase in refractive index. Consequently, the determi-

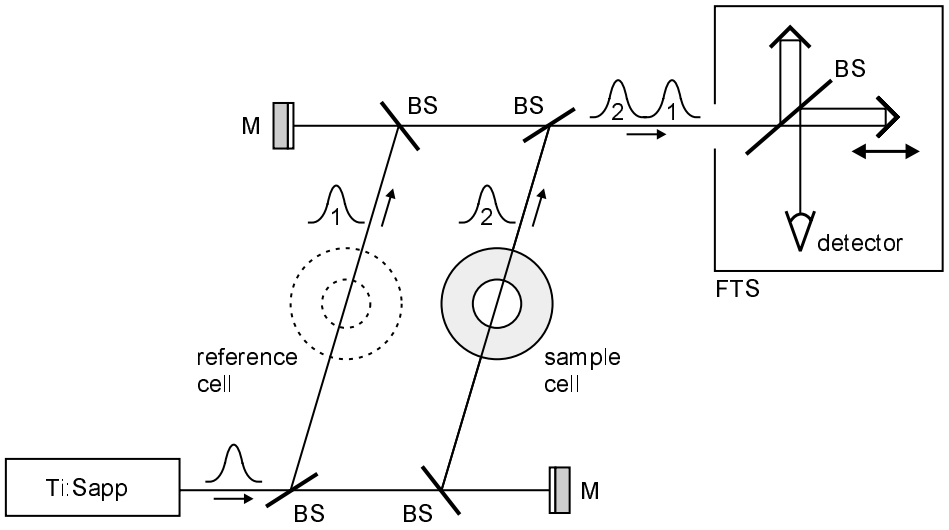

Figure 5.4 An overview of the interferometric time-resolved pulse transmission set up. BS: beam splitter; FTS: Fourier transform spectrometer; M: mirror; Ti:Sapp: pulsed titanium sapphire laser. A 70 fs pulse train from a Ti:sapphire laser is sent through a fixed Mach-Zehnder interferometer with the sample cell in one of the arms. The pulse through the dense supercritical CO_2 (pulse 2) is delayed with respect to the reference pulse (pulse 1), because the refractive index of the dense gas is higher than of the air in the reference cell. This delay is recorded using a scanning Fourier transform spectrometer, from which the refractive index can be inferred *in situ*.

nation of the refractive index via the pressure, implies an extremely accurate measurement. Therefore, it was decided to measure the refractive index itself.

The refractive index is determined *in situ* using a time-resolved interferometric technique [79], see Fig. 5.4. A 70 fs pulse train (rep. rate 82 MHz) from a titanium sapphire lasers (Spectra Physics, Tsunami 3960) with a central wavelength of 780 nm is passed through the supercritical gas in the sample cell. To compare the transmitted pulse (pulse 2 in Fig 5.4) through the dense gas with an undistorted reference pulse (pulse 1), the sample cell is placed in one of the arms of a fixed Mach-Zehnder interferometer. The reference cell serves to balance the interferometer. Due to the refractive index of dense CO_2 being higher than of air (at ambient pressure), pulse 2 is delayed opposed to pulse 1. This time delay $\Delta\tau$ is recorded with a scanning Fourier transform (FT) spectrometer (Biorad, FTS-60A). The delay directly relates to the refractive index difference Δm between the dense gas and the air, that is $\Delta m = (c_0\Delta\tau)/\Delta L$. Here c_0 is the speed of light in vacuo and ΔL the path length through the dense gas, *i.e.* the bore of the sapphire cylinder.

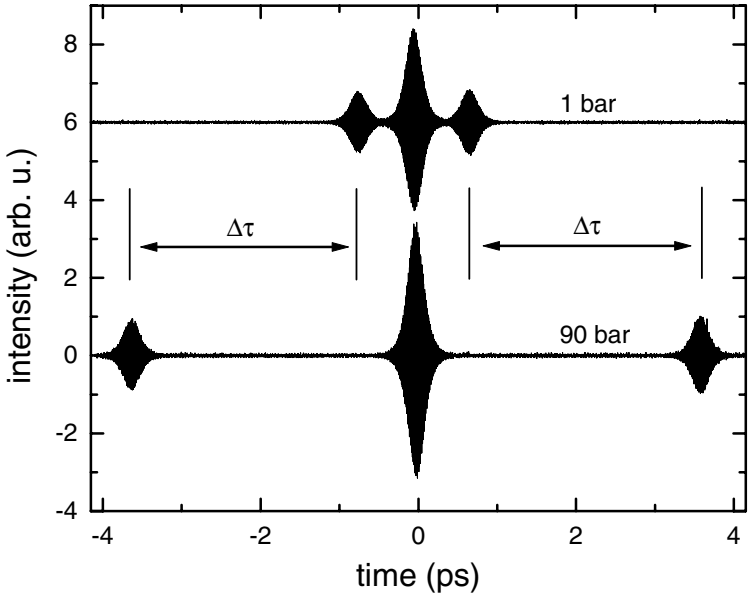

Figure 5.5 The interferogram of the pulse pair exiting the Mach-Zehnder interferometer as measured by the scanning FT spectrometer, for two different pressures of CO_2 (1 and 90 bar). The central peak around time is zero represents the sum of the two auto-correlates for each pulse. The cross-correlates between the two pulses are observed as side peaks. Upon increasing the pressure, the cross-correlates shift in time due to the change in optical path length. The time difference $\Delta\tau$ between the positions of the cross-correlates at 1 and 90 bar, which could be measured with an accuracy of 10 fs, directly relates to the difference in refractive index of CO_2 for these pressures. The high stability of the FT spectrometer allows to resolve the individual fringes of the light field. However, the spacing of fringes is too small to observe in this figure, due to the long time track of more than 8 ps; the peaks are completely filled with fringes. Note that the interferogram recorded at 1 bar is offsetted for clarity.

The interferogram recorded by the scanning FT spectrometer is depicted in Fig. 5.5. The spectrometer measures an interferometric auto-correlate of the incident pulse pair (pulse 1 and 2). Centered around time is zero, the auto-correlates of the respective pulses are observed: $\mathbf{E}_1^*\mathbf{E}_1$ and $\mathbf{E}_2^*\mathbf{E}_2$, where $\mathbf{E}_i$ is the complex amplitude of the electric field of pulse i. The cross-correlates $\mathbf{E}_1^*\mathbf{E}_2$ and $\mathbf{E}_2^*\mathbf{E}_1$ at both sides of the central auto-correlate, carry the essential information on the delay between the two pulses. This is nicely observed in Fig. 5.5, where the cross-correlates shift $\Delta\tau$ in time with increasing pressure, *i.e.* refractive index. As the refractive index of CO_2 at 1 bar is known to be 1.0005 [75], the refractive of the supercritical

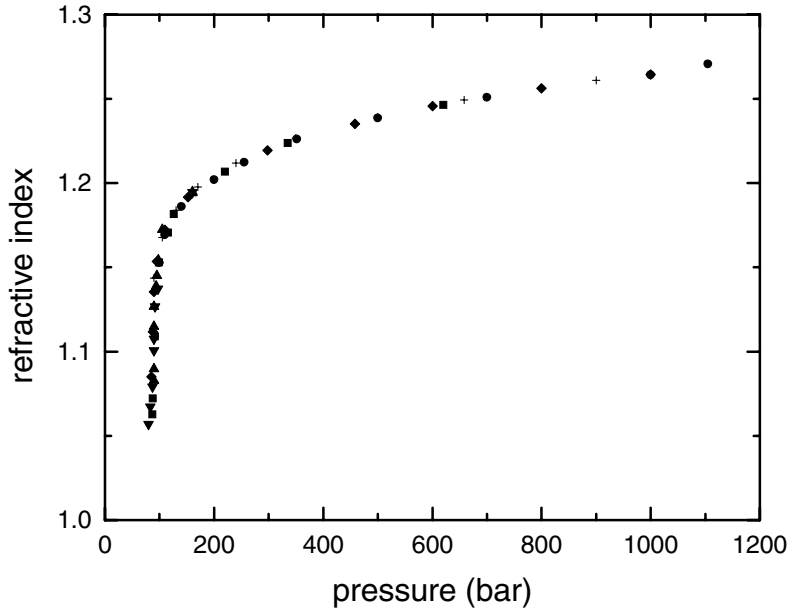

Figure 5.6 The refractive index of supercritical CO_2 versus pressure at 780 nm, for the 35.00 ± 0.05 °C isotherm. The different symbols correspond to different measurement series, indicating the high reproducibility of the set up. The S-shaped curve is typical for a fluid just above the critical temperature. The range of refractive index variation obtained is from 1.05 to 1.27.

gas at any pressure can be inferred from the time delay $\Delta\tau$. The overall accuracy in the refractive index is 10^{-3}, which is mainly determined by the uncertainty in the path length through the sample cell, *i.e.* the bore of the sapphire cylinder.

The refractive index of dense supercritical CO_2 as a function of its pressure is shown in Fig. 5.6. Close to the critical point (31.06 °C and 73.825 bar [76]) a small variation in pressure corresponds to a large change in refractive index. For higher pressures ($>$ 200 bar) the supercritical fluid behaves more like a liquid: a large increase in pressure is necessary to increase the refractive index. The range of refractive index variation is from 1.05 to 1.27. This range is limited on the low side by the minimum density of CO_2 necessary to dissolve detectable amounts of $Eu(fod)_3$, and on the high side by the pressures the sample cell can withstand. Although these measurements were performed at a wavelength of 780 nm, the values obtained for the refractive index hold, within the experimental error, for the entire spectral range of Eu^{3+} luminescence (600-800 nm), as the dispersion of CO_2 is very low [75].

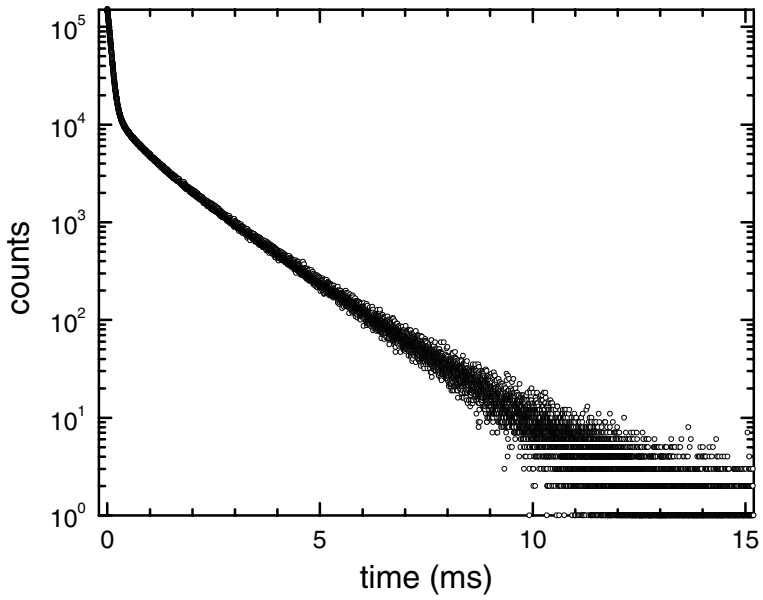

Figure 5.7 The luminescence decay of Eu(fod)$_3$ dissolved in supercritical CO_2 at a pressure of 99 bar (refractive index is 1.154). Two different components are observed. The luminescence lifetime of the long living component is 1.46 ± 0.01 ms. Whereas, the fast decaying component has a characteristic lifetime of 0.14 ± 0.02 ms.

5.4 Luminescence of Eu(fod)$_3$ in dense supercritical CO_2

The set up used to measure luminescence decay and spectra is identical to the one used in the previous chapter, see section 4.6.

A typical luminescence decay of Eu(fod)$_3$ in supercritical CO_2 is shown in Fig. 5.7. As can be seen, the luminescence decay consists of two components, similar as the decay of Eu(hfc)$_3$ in methanol [see section 4.7]. There the fast decaying component was identified as a (partially) dissociated hfc-complex, whereas the slowly decaying component originated from stable Eu(hfc)$_3$.

In order to elucidate the origin of the two components for Eu(fod)$_3$ in CO_2, again time-resolved luminescence spectra were recorded [section 4.7], see Fig.5.8. Identical to Eu(hfc)$_3$ in methanol, both components are related to the luminescence of europium species. The spectrum of the fast decaying component is much more broadened than the spectrum of the slowly decaying component: for the non-degenerate $^5D_0 \rightarrow {}^7F_0$ transition, the line widths are 50 ± 5 and 17 ± 2 cm^{-1}, respectively. For comparison, this line width for Eu(fod)$_3$ in alcohols is 15 ± 2 cm^{-1}.

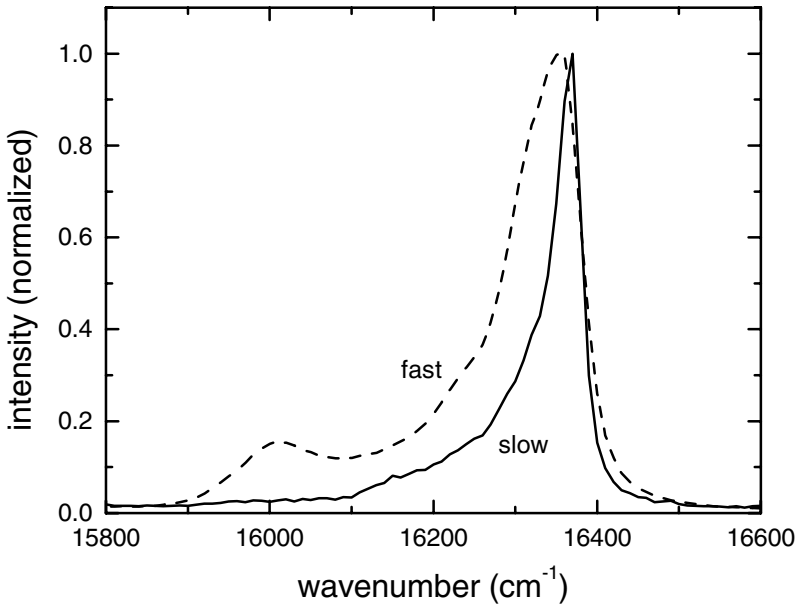

Figure 5.8 The time-resolved luminescence spectra of the fast and slowly decaying components of $Eu(fod)_3$ in supercritical CO_2, measured at a refractive index of 1.214 (250 bar). Both spectra are characteristic for Eu^{3+} luminescence from the $^5D_0$ level to $^7F_2$, indicating that both components are europium related. For both components, the spectra are identical for all refractive indices.

From this broadening, it is concluded that the fast decaying component stems from the luminescence of a dissociating europium complex and is therefore disregarded, conform the conclusions for $Eu(hfc)_3$ in methanol. Apparently, europium complexes in general are not very stable and dissociate relatively easy when in solution. For the case of $Eu(fod)_3$, it turns out that this complex is stable in alcohols, whereas it is only partly stable in dense supercritical CO_2. In the remaining of this chapter, only the slowly decaying component is considered.

The $Eu(fod)_3$ luminescence spectra are identical for all pressures. This indicates that the symmetry of the complex is independent of pressure, which means that the transition dipole moments involved are unaffected by the varying refractive index. Furthermore, although not visible in Fig. 5.8, the luminescence mainly decays through the $^5D_0 \rightarrow {}^7F_2$ transition, proving that the ligand field strongly perturbs the central ion, and hence the transition is of electric dipole character.

5.4.1 The luminescence quantum efficiency

As already mentioned in the previous chapter, the luminescence quantum efficiency plays an important role in these experiments. The choice for CO_2 as the dielectric host is partly based on the fact that the molecular vibrations of the molecule are low in energy. Therefore, as inferred from the theory of multi-phonon relaxation [see section 4.5.1], the contribution of CO_2 to the non-radiative decay is small. More precisely, mainly the fundamental around 1388 cm^{-1} [80] would contribute. However, the large number of vibrations needed (about 12) for the non-radiative decay makes this process negligible. The luminescence quantum efficiency is solely determined by the vibrations of the complex, and not by the dielectric host, CO_2.

For $Eu(fod)_3$ in alcohols, it was concluded that the non-radiative decay mainly occurs via the O-H oscillators of one H_2O molecule binded to the Eu^{3+} ion in the first coordination sphere. Here, it will be shown that this one H_2O molecule is *not* present in the $Eu(fod)_3$ complex when dissolved in CO_2. As a direct consequence, the luminescence quantum efficiency is significantly higher.

The luminescence lifetimes observed are around 1.5 ms, which corresponds to a decay rate of 0.67 ms^{-1}. From the results of Horrocks and Sudnick [see section 4.5.2], the contribution to the non-radiative decay of each O-H oscillator in the first coordination sphere is 0.47 ms^{-1}. Therefore, the presence of 1 H_2O molecule (2 O-H oscillators) close to Eu^{3+} would at least give a luminescence decay rate of 0.94 ms^{-1}, whereas the experiment shows a considerably lower rate [81]. This directly leads to the conclusion, that no water molecules can be present close to the Eu^{3+} ion. This is also confirmed by the difference in luminescence spectra, compare the $^5D_0 \rightarrow {}^7F_2$ transition in Figs. 4.6 and 5.8, indicating that the local environment is different for $Eu(fod)_3$ in alcohols and in dense CO_2, that is with and without 1 H_2O molecule, respectively.

As water is eliminated as a source of luminescence quenching, only the oscillators of the fod-complex itself are left to serve as acceptors. From all candidates, the C-H stretch vibrations in the *second* coordination sphere, in the middle of the β-diketone ring, are the most efficient quenchers, see Fig. 4.2. In total there are 3 (1 for each fod-ligand) of these C-H oscillators present in the $Eu(fod)_3$ complex. However, the contribution to the non-radiative decay of a C-H oscillator in the second coordination sphere is smaller than 0.01 ms^{-1} [see section 4.5.3]. Hence, the maximum total non-radiative decay rate is 0.03 ms^{-1}. Comparing this to the observed luminescence decay rate of ~ 0.67 ms^{-1}, leads to the conclusion that the luminescence quantum efficiency is higher than 0.95 (95 %); similar high efficiencies have been reported previously for europium complexes [46, 54]. The luminescence lifetimes obtained are also the radiative lifetimes.

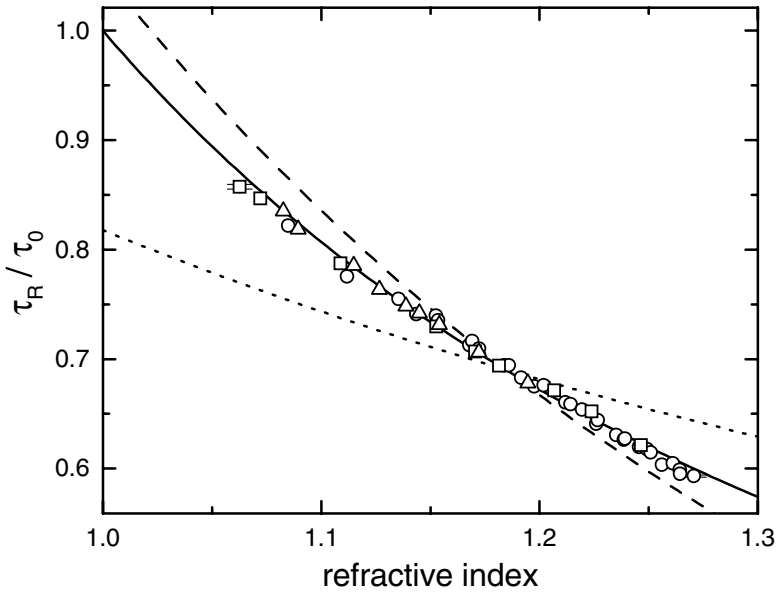

Figure 5.9 The scaled radiative decay times as a function of refractive index. The radiative lifetimes τ_R are scaled by the extrapolated vacuum lifetimes τ_0. The vacuum lifetime slightly depends on the excitation energy per shot P. For $P = 4 \pm 1$ mJ/cm^2: $\tau_0 = 2.04 \pm 0.01$ ms (squares), $P = 17 \pm 3$ mJ/cm^2: $\tau_0 = 1.97 \pm 0.01$ ms (circles), $P = 70 \pm 20$ mJ/cm^2: $\tau_0 = 1.85 \pm 0.01$ ms (triangles). For comparison, the results from the empty-cavity (full line), full-cavity (dashed line), and no-cavity models (dotted line) are plotted. The error bars for both the decay times and the refractive index are of the order of the symbol size.

5.4.2 Local-field effects on spontaneous emission

The measured variation of radiative lifetime with refractive index is shown in Fig. 5.9. The high quality of the data allows for a comparison to the substitutional-impurity or empty-cavity [Eq. 3.11], interstitional-impurity or full-cavity [Eq. 3.16], and no-cavity [Eq. 3.1] models. The red shift predicted by Eqs. 3.9 and 3.14 is not observed, the spectra are independent of refractive index, and hence the polarizability density α_I/Ω of the complex is taken to be zero in Eqs. 3.11 and 3.16. Clearly, the empty-cavity model applies. Furthermore, it is observed that the extrapolated vacuum lifetimes slightly depend on the excitation energy. A 10% decrease in the lifetime is found when the pumping energy is increased from 4 ± 1 mJ/cm^2 to 70 ± 20 mJ/cm^2; similar dependences have been observed previously [82]. This effect is probably due to the cooperative decay of

europium molecules via stimulated emission at higher pump intensities. Nonetheless, the empty-cavity model is confirmed for all pumping powers, giving confidence that this is indeed the right model.

5.5 Conclusions

In conclusion, the luminescence decay experiments on $Eu(fod)_3$ in dense supercritical CO_2 confirm that the complex is a substitutional impurity [Eq. 3.11], that is the CO_2 molecules experience a real excluded volume. This result, together with theoretical description presented in chapter 3, settles a long discussion on which local-field correction applies to spontaneous emission.

It should be stressed that the observation of local-field corrections to spontaneous emission remains subtle. In this regard, the following should be noted. Similar experiments were performed using dense supercritical Xe as the dielectric host. The advantage of Xe above CO_2 is in the larger refractive index range (1.05-1.38) attainable, due to the larger polarizability of the Xe atom. However, it turned out that the luminescence decay of $Eu(fod)_3$ in Xe is multi exponential, most likely because many indistinguishable components contribute. Furthermore, the luminescence spectra changed upon increasing the pressure, indicating that the fod-complex is completely unstable in supercritical Xe, rendering this system useless. The difficulties encountered in the experiments on the luminescence of europium complexes in alcohols and in supercritical Xe clearly indicate that indeed the choice of system (luminescing impurity + dielectric host) is crucial for observing the local-field effect.

CHAPTER 6

Strongly photonic macroporous GaP networks

A photo-assisted electrochemical etching technique to fabricate macropores in single crystalline gallium phosphide (GaP) with variable porosity has been developed. Scanning electron microscopy and X-ray diffraction experiments confirm that the material consists of three dimensional, interconnected random networks with pore sizes of about 150 nanometers. Optical transmission measurements demonstrate that the non-absorbing, disordered structures strongly scatter light. The photonic strength is controlled by filling the pores with liquids of different refractive index. Macroporous GaP filled with air has the highest scattering efficiency for visible light reported to date.

6.1 Strongly photonic materials

In a binary system with components of refractive indices n_1 and n_2, the efficiency of light scattering depends on how these components are organized in the system, the dimensions of the components and the refractive index ratio $n_1/n_2 = m$. Scattering of light is strongest if m is large, and the length scale of refractive index variation, s, is comparable to the wavelength of light λ. This regime has received much attention, in the search for strongly scattering (photonic) materials. For ordered systems with a periodic variation in the refractive index, the material is a photonic crystal. These feature photonic band gaps [8, 83], frequency ranges for which light will not propagate in the crystal due to multiple Bragg reflections. If the material is disordered, interference of scattered light ultimately leads to Anderson localization [18, 84]. Photonic band gaps and Anderson localization are closely related. Both inhibit light propagation due to interference not absorption , and can only be obtained for strongly photonic materials, those with $m \sim 3$ or larger.

For infrared light, Anderson localization has been reported for GaAs powders ($m \simeq 3.5$) [84] and a two-dimensional photonic band gap for macroporous Si

($m \simeq 3.4$) [85]. In the visible, considerable progress has been made by the preparation of three-dimensional air-sphere crystals of TiO_2 ($m \simeq 2.7$) [83]. Inhibition of propagation of visible light has not yet been reported for three-dimensional structures, apparently larger m (> 2.7) are needed. Obviously, m is a crucial parameter for photonic materials. In addition to large m, it is thus desirable to have the ability to tune m, allowing investigation of its importance for the photonic strength.

Intermezzo As already mentioned, strongly photonic materials are obtained for large variations in the refractive index, or equivalently the dielectric constant, on length scales of the wavelength of light. In this intermezzo, a microscopic validation for these requirements is presented.

Consider the extinction cross section of a dielectric sphere with dielectric constant ε embedded in vacuo, see section 2.6.3, specifically Eq. 2.76. For simplicity of the argument, assume that the dielectric constant is close to unity and can thus be written as $\varepsilon = 1 + \rho\alpha$, see Eq. 2.26. Combining Eqs. 2.26 and 2.76 yields for the extinction cross section

$$\sigma_{\text{ex}} \simeq \frac{1}{6\pi}[\rho\Omega\alpha]^2 \left(\frac{\omega}{c_0}\right)^4 \propto N^2, \tag{6.1}$$

where $N \equiv \rho\Omega$ is the total number of microscopic dipoles that constitute the sphere of volume Ω. If all these dipoles would contribute to the scattering independently, the extinction cross section would scale with just the number of the dipoles N. The N^2-dependence is due to the fact that the dipoles all radiate in phase, that is the individual scattering amplitudes add up coherently.

Now it seems that in order to obtain strong scattering, that is a strongly photonic system, it is just a matter of increasing the number of dipoles N. However, the coherent addition of the individual scattering amplitudes fails when the sphere becomes of the order of or larger than the wavelength λ, as then the dipoles are no longer all in phase since they are too far apart. The largest attainable cross section of a random scatterer is about λ^2. So a material that is homogeneous and much larger than the wavelength hardly scatters light, simply because those parts of the medium that radiate in phase are counter-balanced with parts in anti-phase; a bowl of water is evidently transparent. This absence of scattering can be remedied by removing the parts that are in anti-phase, leaving a medium with only in-phase parts, which consequently strongly scatters light again. The material obtained has air holes (the removed anti-phase parts) about a wavelength apart; the refractive index varies on length scales of the wavelength of light. Furthermore, for materials with a higher dipole density ρ and/or microscopic polarizability α, that is with a higher refractive index, the scattering efficiency in general increases, see for example Eq. 6.1. The

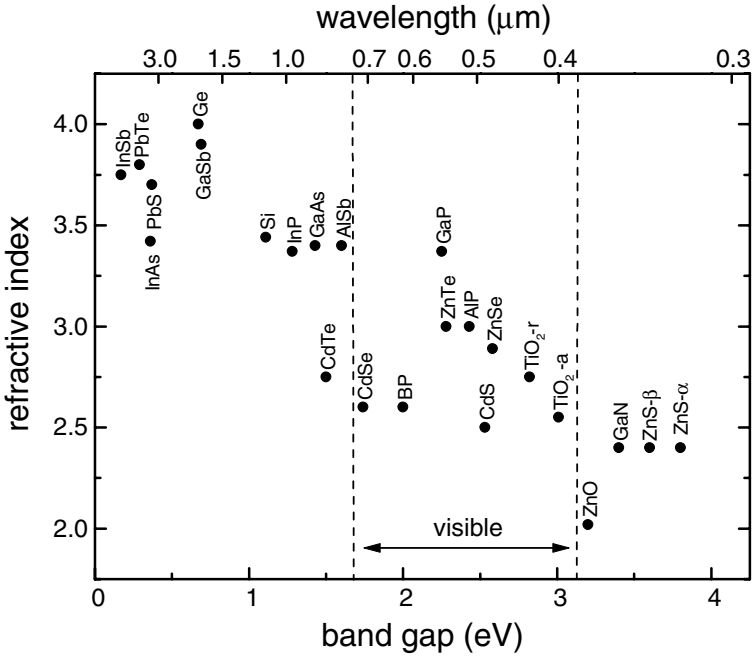

Figure 6.1 The refractive index of various (semiconducting) materials as a function of their electronic band gap. On average, the refractive index decreases with increasing band gap. For photon energies lower than the electronic band gap (sub-bandgap light), the materials are transparent; for higher photon energies light is absorbed. Data taken from [87].

requirements for a strongly photonic system are now based on qualitative microscopic considerations.

Semiconducting materials are highly suitable for the preparation of strongly photonic materials as they have large refractive indices and, for sub-bandgap light, low absorptivities, see for an overview Fig. 6.1. The low absorptivity is essential, as the origin of the full photonic band gap and Anderson localization, interference, has to survive. Materials with smaller electronic band gaps tend to have larger refractive indices, which can be qualitatively explained by modeling the inter-band transition as a two-level system [86]. Germanium is a good candidate with a large refractive index of 4.1, but to avoid inter-band absorption the wavelength of light has to be $\sim 2\ \mu$m or longer, making it experimentally difficult to access. Gallium phosphide (GaP) has a large refractive index of ~ 3.3 and an indirect band gap of 2.24 eV (550 nm) [87], allowing the preparation of strongly photonic systems with negligible absorption in the red part of the *visible* spectrum.

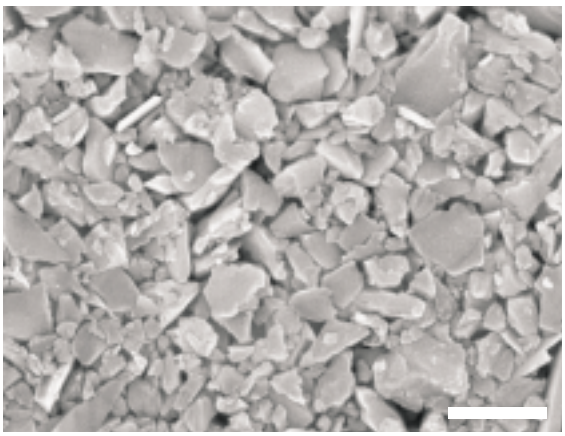

Figure 6.2 A SEM micrograph of finely grained germanium. The lighter areas correspond to Ge and the darker parts to the air in between. The Ge powder was sedimented to reduce the poly-dispersity (see text); the typical particle diameter is ~ 0.5 μm. The scale bar represents 1 μm. Picture by courtesy of J. Gómez Rivas [89].

The variation of refractive index on length scales of the wavelength of light can be obtained in many different ways. For photonic band gap materials, templating with artificial opals seems to be ideal [83]. For random materials, grinding semiconductors has shown to be successful: for fine grained GaAs localization has been reported [84], and similarly prepared Si powders nearly localize light [88]. Scanning electron microscopy (SEM) on finely grained Ge clearly shows a modulated dielectric structure, see Fig. 6.2; the single crystals of Ge were powdered in a planetary micromill by J. Gómez Rivas [89]. After milling, the variation in particle size is large. To reduce this poly-dispersity, the powder was suspended in methanol and let to sediment for 2.5 minutes. Only the smaller particles, which are left in suspension, were used to prepare the strongly scattering material. Despite considerable effort, the poly-dispersity remains fairly large.

In this chapter a new technique, photo-assisted electrochemical etching, is presented for the preparation of a different type of strongly scattering random material, that is macroporous GaP networks. These networks are mechanically stable and can hence be filled with various liquids, allowing the importance of the refractive index contrast on the photonic strength to be investigated.

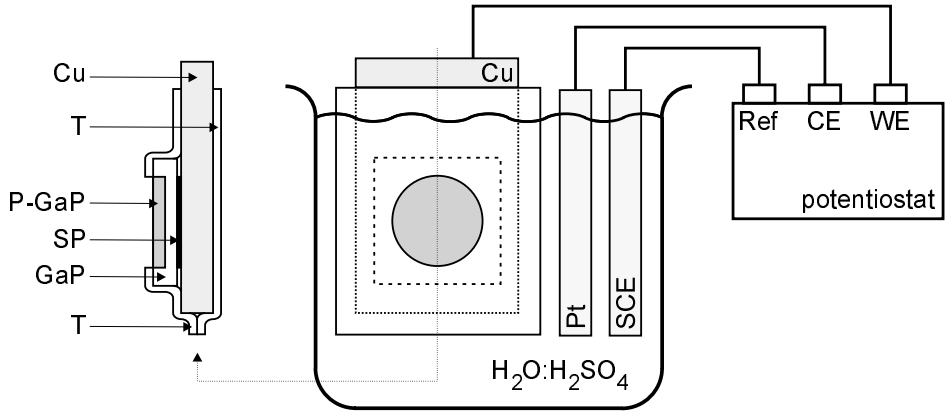

Figure 6.3 A schematic overview of the electrochemical set up used for the preparation of macroporous GaP. CE: counter electrode; Cu: copper; GaP; gallium phosphide wafer; P-GaP: porous GaP; Pt: platinum counter electrode; Ref: reference electrode; SCE: Saturated Calomel Electrode; SP: silver paste; T: teflon sticker; WE: working electrode. The GaP wafer is mounted as a working electrode in a standard electrochemical cell with a 0.5 M sulphuric acid electrolyte; the applied potential is controlled by the potentiostat. At the left, a cross section of the working electrode is depicted. The GaP wafer is brought into Ohmic contact with a copper plate with the use of silver paste. In order to protect the Cu from the electrolyte, the assembly is packed in teflon sticker, leaving open a circular area of 0.24 cm^2 for etching GaP.

6.2 Preparation of macroporous GaP networks

The macroporous GaP structure is formed by electrochemical anodic etching of n-type of GaP single crystals (donor density 2×10^{17} cm^{-3}, [90]) under dielectric breakdown conditions [91, 92, 93]. The 350 μm thick, polished wafers are mounted with a (100)-face exposed to the 0.5 M H_2SO_4 electrolyte as the working electrode in a standard electrochemical cell, with a Saturated Calomel Electrode (SCE) as reference and a platinum counter electrode, see Fig. 6.3. Potentials are given with respect to SCE. The cell was controlled by means of an EG&G PAR273A potentiostat.

Application of a strong positive potential (15 V SCE) leads to severe band bending at the n-GaP/electrolyte interface, see Fig. 6.4. Inter-band tunneling of electrons [95] from the valence band or from band gap states to the conduction band takes place, generating holes at the surface, which are consumed in anodic dissolution of GaP, that is [96]

$$GaP + 6h^+ \rightarrow Ga^{3+}(aq) + P^{3+}(aq). \tag{6.2}$$

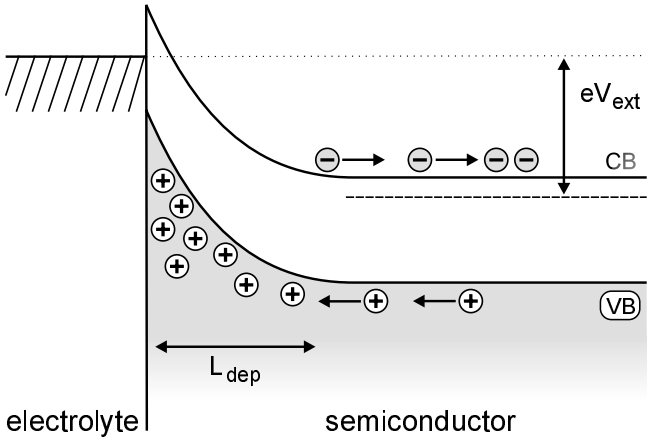

Figure 6.4 The energy-band diagram of the semiconductor/electrolyte interface under reversed bias voltage V_{ext}; the characteristics are very similar to a Schottky diode (metal/semiconductor junction) [94]. The energy difference between the Fermi level in the semiconductor (dashed line just below the conduction band (CB)) and in the electrolyte is determined by eV_{ext}. Band bending takes place at the interface. Consequently, electrons tunnel from the valence band (VB) to the CB, leaving an accumulation of holes at the interface, *i.e.* electrons are depleted. The thickness of this depletion layer L_{dep} depends on the electronic properties of the semiconductor and the applied potential V_{ext}.

The generation of holes is spatially non-uniform. More specifically, initially submicron pits are etched at surface defects, about 10 microns apart. These pits serve as the starting points for the etching of the sub-surface porous structure [92]. As soon as the whole electrode surface is covered with a porous layer, the anodic etching current is becomes constant, indicating that the porous network is uniformly growing deeper into the GaP crystal. The anodic charge is proportional to the thickness of the porous structure L, enabling coulometric control of this important parameter [93]. A SEM micrograph of a cross section of a porous slab is used to calibrate the linear charge-thickness relation, see Fig 6.5 [*left*]. The corresponding porosity is determined to be ~ 35 volume-% of air. In this fashion, a series of samples with porous slab thicknesses from 5 to 120 μm was prepared.

In addition to the anodically etched GaP (A-GaP), also photoanodically etched GaP (PA-GaP) samples were prepared. Exploiting a new technique that utilizes homogeneous photo-assisted etching, slabs with a higher porosity were obtained. A-GaP samples are subjected to a further process of photoanodic etching in a H_2O:H_2SO_4:H_2O_2 electrolyte using 50 mW of 1.96 eV sub-bandgap light from a HeNe laser, under an applied positive potential of 2 V SCE. The applied potential

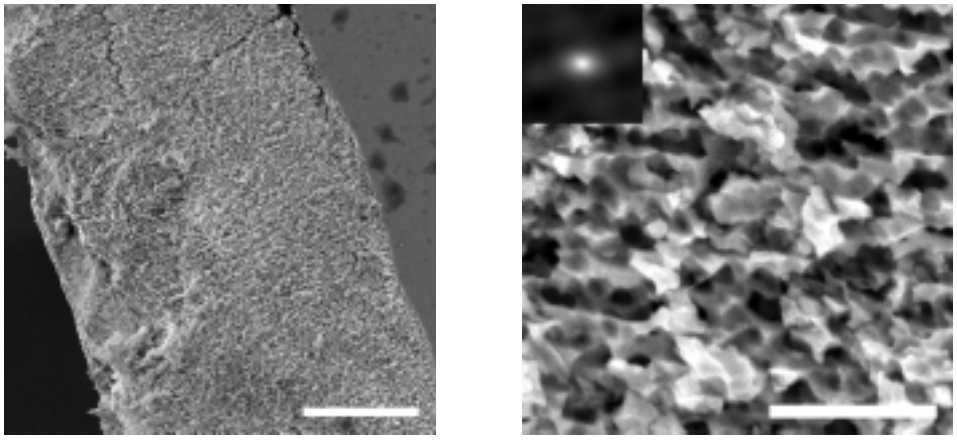

Figure 6.5 Two SEM micrographs of macroporous GaP:
[*left*]: A cross section of a porous slab of GaP. In the top right, the unetched GaP substrate is visible, whereas, in the lower left corner, the air-porous GaP interface is seen. The slab is etched by passing 10 C through the cell for a fixed electrolyte/GaP interface area of 0.24 cm^2, leading to a thickness of 50 μm. The small ruptures and irregularities are caused by breaking the sample, which is necessary to make the image . The scale bar represents 20 μm.
[*right*]: A SEM micrograph of photoanodically etched GaP (PA-GaP) and in the inset its auto-correlate. The lighter areas correspond to GaP and dark parts to the pores. The typical size of the GaP entities is about 150 nm, as concluded from the auto-correlate. The porous structure is statistically homogeneous and isotropic. The scale bar represents 1 μm.

is too low for the anodic etching process to take place, so that the thickness of the porous slab is not affected by the photoanodic etching treatment, only the porosity is increased. Photons are absorbed by a transition of an electron from the top of the valence band to an interfacial state, 0.3 eV below the conduction band, followed by thermal release of the interfacial electron into the conduction band [97]. The remaining hole is involved in anodic dissolution. The addition of H_2O_2 to electrolyte serves to enhance the extremely low absorption probability: H_2O_2 chemisorbs at the GaP surface and thereby increases the density of interfacial states just below the conduction band [93], making sub-bandgap absorption more efficient. Due to the nevertheless weak absorption of the light in the porous structure, the photoanodic etching current is linear with sample thickness, see Fig. 6.6. Consequently, the etch rate is constant across the porous network and the porosity of the sample is increased uniformly, controlled by the photoanodic etch charge. In such a way, PA-GaP with slab thicknesses between 5 and 60 μm were prepared, with an

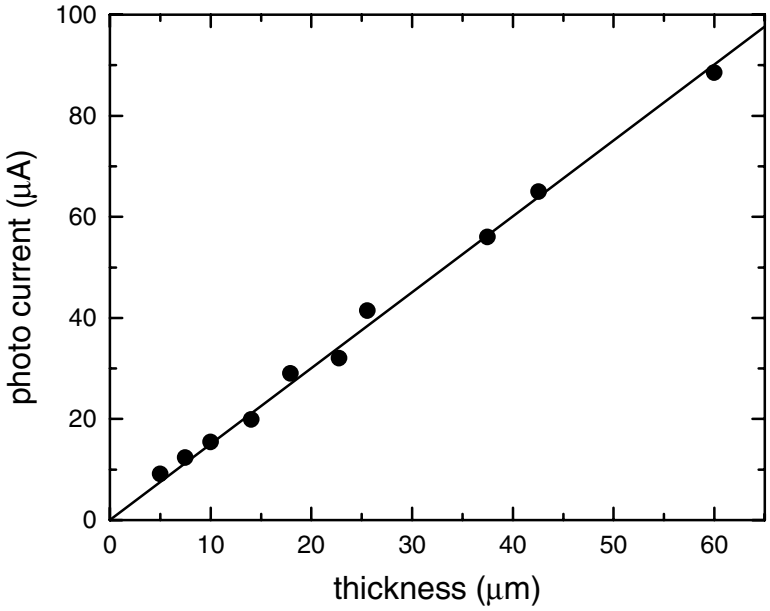

Figure 6.6 The photoanodic etching current of porous GaP in the H_2O:H_2SO_4:H_2O_2 electrolyte under illumination of 50 mW of HeNe light as function of sample thickness. As can be seen, the photocurrent is linear with slab thickness, with a constant of proportionality of 1.50 ± 0.03 A/m, indicating that the absorption is uniform throughout the porous structure for all slab thicknesses. The error bars are of the order of the symbol size.

increased estimated porosity to about 50 volume-% of air. Further etching resulted in mechanically unstable samples, probably due to reaching the rigidity percolation threshold [98].

A SEM micrograph of the porous structure of PA-GaP (Fig. 6.5 [*right*]) reveals that the structure is random. A detailed and quantitative analysis of the PA-GaP structure is obtained from the auto-correlation function, which is also known as the Patterson function [99]. This function represents the spatial correlation of the GaP structures, or, equivalently, the air structure in between. The auto-correlate is not circular symmetric but slightly elongated, indicating a preferential direction. PA-GaP is characterized by two correlation lengths, along and perpendicular to this direction, which are 155 ± 8 and 108 ± 6 nm, respectively. Analysis of the SEM pictures from different parts of the porous sample show the same values for the two correlation lengths, a characteristic of a statistically homogeneous material. Furthermore, the slight asymmetry in the auto-correlate is connected to preferential etching along certain crystallographic axes [91], also indicated by the somewhat tri-

angular shape of the GaP entities. However, for different parts of the porous structure, the direction was along different crystallographic axes, among which no correlation could be detected. Therefore, the entire sample on average is considered to be isotropic and homogeneous.

6.3 Total transmission

To the eye, bulk GaP is transparent and orange, while the color of A-GaP is dark yellow and the PA-GaP samples are more bright whitish yellow. This indicates that PA-GaP scatters light more strongly than A-GaP, as apparently for PA-GaP relatively more blue light is scattered out before it is absorbed. The scattering efficiency is measured quantitatively by determining the total light transmission through the porous slab as function of its thickness L, as will be shown below.

6.3.1 Diffusion of light

Light propagating through disordered media is multiply scattered, making an exact description of the transport of light through such media extremely difficult. An enormous simplification in the description of the transport of light can be made by neglecting all interference effects, as then transport may be described by diffusion [100, 101]. Light propagates by performing a random walk, which is characterized by the transport mean free path ℓ, the average distance light propagates before its direction is randomized. For slab geometries, the three-dimensional diffusion equation reduces to the one-dimensional case in the non-translationally invariant direction, *i.e.* the z direction. Then, the energy density $U(z)$ in the stationary state inside the sample is determined by

$$\left[\frac{\partial^2}{\partial z^2} - \frac{1}{L_\mathrm{a}^2}\right] U(z) = -\frac{1}{D} I_0 \delta(z-\ell), \tag{6.3}$$

where L_a is the diffuse absorption length and D the diffusion constant. The diffusion constant is given by $D = v_\mathrm{e}\ell/3$, where v_e is the energy transport velocity in the medium [102]. In Eq. 6.3, the incoming energy flux at the boundary $z = 0$ has been replaced by a source of diffusive radiation of strength I_0 located at $z = \ell$ [21]. Simulations have shown that Eq. 6.3 is accurate to within about 1 % for slabs sufficiently thick to be opaque [103].

Diffuse internal reflection [104, 105] at the boundaries is the source of the diffuse fluxes going into the sample at $z = 0$ and L. Hence, the boundary conditions can be written as [105]

$$U - z_{\mathrm{e},1}\frac{\partial U}{\partial z} = 0, \quad U + z_{\mathrm{e},2}\frac{\partial U}{\partial z} = 0, \tag{6.4}$$

where $z_{e,i}$ are the extrapolation lengths, with the interface label $i = 1,2$ for $z = 0, L$, respectively. These extrapolation lengths depend on the polarization and angular averaged reflectivities of the boundaries $\overline{R_i}$, that is $z_{e,i} = (2\ell/3)(1+\overline{R_i})/(1-\overline{R_i})$.

In the experiments, the total transmission coefficient is determined, which is defined as the transmitted flux normalized to the incident flux, and given by [88, 106]

$$T_{12} = \frac{-D}{I_0}\left.\frac{\partial U}{\partial z}\right|_{z=L} = \frac{\sinh(\ell/L_a) + (z_{e,1}/L_a)\cosh(\ell/L_a)}{(1+z_{e,1}z_{e,2}/L_a^2)\sinh(L/L_a) + (1/L_a)(z_{e,1}+z_{e,2})\cosh(L/L_a)}, \tag{6.5}$$

where the labeling of T_{12} indicates that the light is incident at interface 1 and leaves the sample at interface 2. For asymmetric scattering geometries, that is $z_{e,1} \neq z_{e,2}$, or equivalently $\overline{R_1} \neq \overline{R_2}$, the total transmission coefficient depends on the interface of illumination: $T_{12} \neq T_{21}$. In experiments, the scattering medium is most often sustained by a transparent substrate, leading to this asymmetry. This point will be discussed in more detail in the experimental results section.

For non-absorbing samples, $L_a \gg L$, Eq. 6.5 simplifies to

$$T_{12} = \frac{\ell + z_{e,1}}{L + z_{e,1} + z_{e,2}}. \tag{6.6}$$

Contrary, for strongly absorbing samples, $L_a \ll L$, the total transmission decreases exponentially with sample thickness L, that is $T \propto \exp[-L/L_a]$.

6.3.2 Experimental results

Total transmission measurements were done at the wavelengths λ = 632, 685, and 780 nm. The transmitted diffuse light intensity was collected with a 3-inch $BaSO_4$ integrating sphere (Labsphere) and measured using a silicon diode detector, see Fig. 6.7 [*left*].

For the comparison of the transmission measurements with diffusion theory, Eqs. 6.5 and 6.6, it is essential to know the extrapolation lengths $z_{e,i}$. The extrapolation length $z_{e,1}$, corresponding to the air-porous medium interface (see Fig. 6.7 [*right*]), depends on the mismatch between the refractive index of air and the average refractive index of the scattering medium n_e, as this mismatch determines the reflection coefficient $\overline{R_1}$. Similarly, $z_{e,2}$ depends on n_e and the refractive index of the crystalline GaP substrate. The average refractive index n_e is determined by the refractive indices of the constituting components, *i.e.* air and GaP, and their relative volume fractions, see section 2.6. From Maxwell Garnett effective medium

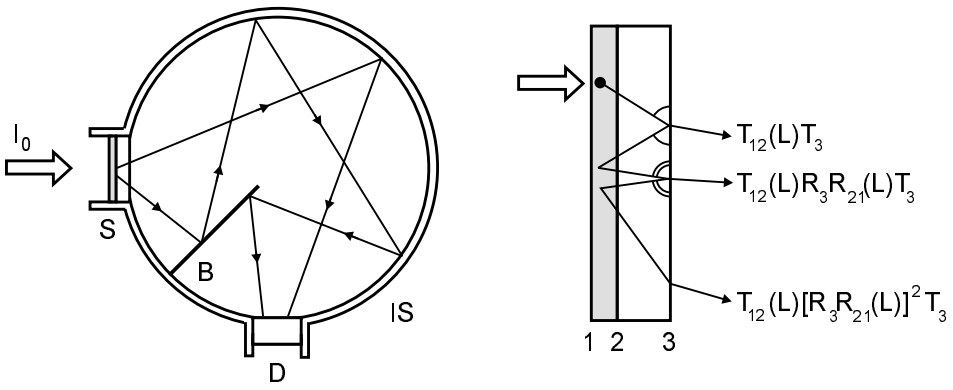

Figure 6.7 [*left*]: A schematic overview of the total transmission set up. B: baffle; D: detector; IS: $BaSO_4$ integrating sphere; I_0: incident light intensity; S: sample. The diffuse transmitted light intensity is collected by the integrating sphere, where the baffle ensures that no light enters the detector without being scattered in the IS. The sample is mounted with the porous slab facing the incident beam.
[*right*]: A zoom-in on the sample, with the porous slab in grey and the crystalline GaP substrate in white. Transmitted light through porous medium is specularly reflected by the substrate-air interface (interface 3), modifying the total light transmission. Multiple reflections inside the substrate have to be taken into account in order to obtain a quantitative comparison between the experiment and diffusion theory. The individual terms contributing to the total transmission are described in the text.

theory, Eqs. 2.68, the average refractive index for A-GaP (35 volume-% air) is predicted to be 2.42, and for PA-GaP (50 volume % air) 1.97. The results for n_e from Bruggeman's approach, Eq. 2.72, are very similar, and yield 2.44 and 2.04, for A-GaP and PA-GaP, respectively. Note that the results from effective medium theory only apply in the long wavelength limit, that is in the absence of scattering. Indeed, experiments [107] have shown that for (strongly) scattering media the average refractive index is significantly lower than calculated from effective medium theories. Therefore, for the rest of this thesis, the following estimated average refractive indices will be used: A-GaP: $n_e = 2.0 \pm 0.1$ and PA-GaP: $n_e = 1.7 \pm 0.1$. Given these average refractive indices, the reflection coefficients $\overline{R_i}$ and extrapolation length ratios $z_{e,i}/\ell$ can be calculated [105]; the results are summarized in Tab. 6.1

Besides diffuse internal reflection, also multiple reflections inside the GaP substrate influence the transmission coefficient, see Fig. 6.7 [*right*]. The total transmission coefficient $T(L)$ is given by the sum of the individual contributions

$$T(L) = \sum_{n=0}^{\infty} T_{12}(L)[R_3 R_{21}(L)]^n T_3 = \frac{T_{12}(L)T_3}{1 - R_3 R_{21}(L)}. \tag{6.7}$$

	n_e	$\overline{R_1}$	$z_{e,1}/\ell$	$\overline{R_2}$	$z_{e,2}/\ell$
A-GaP	2.0 ± 0.1	0.78 ± 0.05	5.4 ± 0.6	0.10 ± 0.01	0.81 ± 0.02
PA-GaP	1.7 ± 0.1	0.67 ± 0.06	3.4 ± 0.5	0.14 ± 0.02	0.89 ± 0.03

Table 6.1 The average refractive index n_e, reflection coefficients $\overline{R_i}$, and extrapolation length ratios $z_{e,i}/\ell$ of A-GaP and PA-GaP, for the air-porous medium interface ($i = 1$) and the porous medium-substrate interface ($i = 2$). The errors are determined by the estimated error in n_e.

Here $T_{12}(L)$ is the transmission coefficient through the porous slab of thickness L (Eq. 6.6), T_3 the angle averaged transmission coefficient of interface 3, $R_3 = 1 - T_3$, and $R_{21}(L)$ the diffuse reflection coefficient of the porous slab. Under the assumption that the scattering medium is non-absorbing, that is $R_{21}(L) + T_{21}(L) = 1$, the *inverse* transmission becomes

$$[T(L)]^{-1} = [T_{12}(L)]^{-1} + C, \tag{6.8}$$

where C is a constant independent of L given by $(\ell + z_{e,2})/(\ell + z_{e,1})(R_3/T_3)$. Apparently, the inverse transmission T^{-1} is only offsetted by the constant C, and hence the slope of T^{-1} versus L is not influenced by the presence of a substrate.

In Fig. 6.8, the inverse total transmission versus the porous slab thickness L for $\lambda = 685$ nm is shown. The measurements are described by classical diffusion with negligible absorption, as is evident from the linear dependence, see Eqs. 6.6 and 6.8. The results for $\lambda = 632$ and 780 nm are similar, where the slope for both A-GaP and PA-GaP is higher for 632 nm, and lower for 780 nm. Given the extrapolation length ratios, see Tab. 6.1, and using Eq. 6.6, it is easy to extract the transport mean free paths ℓ from the measurements; the results are summarized in Tab. 6.2. To

	A-GaP		PA-GaP	
λ (nm)	ℓ (μm)	$k_e\ell$	ℓ (μm)	$k_e\ell$
632	0.42 ± 0.04	8.3 ± 0.5	0.13 ± 0.02	2.2 ± 0.2
685	0.47 ± 0.05	8.6 ± 0.5	0.17 ± 0.02	2.6 ± 0.2
780	0.59 ± 0.06	9.5 ± 0.6	0.27 ± 0.03	3.7 ± 0.3

Table 6.2 Transport mean free paths ℓ and $k_e\ell$-values for A-GaP and PA-GaP. Obviously, PA-GaP scatters approximately three times as efficient as A-GaP. For shorter wavelengths, the scattering efficiency is also slightly higher. The errors are determined by the uncertainty in the extrapolation length ratios, which are taken to be independent of wavelength.

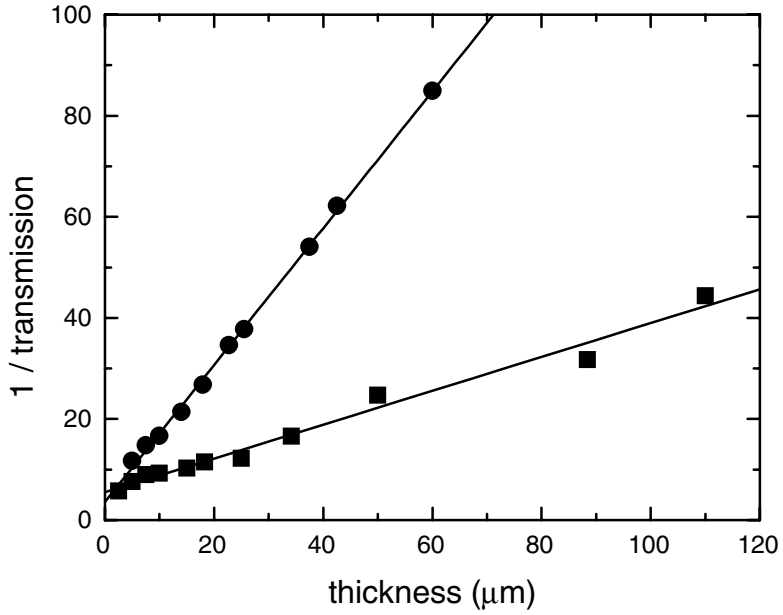

Figure 6.8 The inverse total transmission as a function of the porous slab thickness, measured at 685 nm. The squares correspond to anodically etched GaP (A-GaP) and the circles to photoanodically etched GaP (PA-GaP). The solid lines are calculated using diffusion theory with negligible absorption, giving excellent agreement with the data. The transport mean free paths are inferred from the slope, resulting in $0.47 \pm 0.05\,\mu$m and $0.17 \pm 0.02\,\mu$m for A-GaP and PA-GaP, respectively. The error bars are of the order of the symbol size.

compare the scattering properties of the samples, the values of $k_e\ell = \frac{2\pi}{\lambda} n_e \ell$, the standard measure of inverse scattering efficiency, are also given in Tab. 6.2. The photoanodic etching treatment enhances the scattering efficiency by more than a factor of three, resulting in the most strongly scattering material for visible light reported to date [108].

The scattering efficiency is observed to increase for shorter wavelengths. This is most likely due to the typical size ($\sim$ 150 nm) of the GaP scattering entities in the porous structure being relatively small compared to the wavelength.

6.4 Filling the pores with liquids; tuning the scattering efficiency

From the single spots in the X-ray diffraction pattern, it is concluded that after etching the porous layer is still single crystalline GaP, meaning that the network is completely interconnected. As a result, the material is mechanically stable and can be

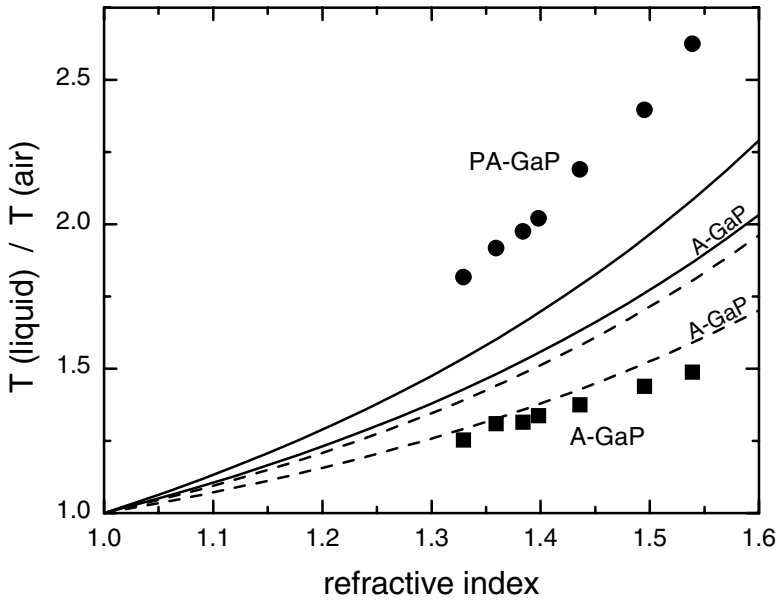

Figure 6.9 Transmission of light at λ = 685 nm through anodically etched (A-GaP, squares) and photoanodically etched GaP (PA-GaP, circles) filled with liquids, normalized to the transmission of the air filled sample, as a function of the refractive index of the liquid. The increase in transmission matches the increase in ℓ, which is a direct measure of the opacity. Results from effective medium theories are shown for comparison: Maxwell Garnett (dashed lines, see Eq. 6.10) and Bruggeman theory (solid lines, see Eq. 6.9). The models are plotted for the two corresponding volume fractions: 35 % of air for A-GaP and 50 % for PA-GaP; the curves for A-GaP are labeled for clarity. Although both models qualitatively describe the dependence of ℓ on the porosity and refractive index ratio, no quantitative agreement could be obtained. The error bars are of the order of the symbol size.

filled with liquids.

For λ = 685 nm, the diffuse light transmission through a 50 μm thick sample, filled with liquids of different refractive index, ranging from 1.33 to 1.54, is shown in Fig. 6.9. The transmission increases due to the decrease in refractive index ratio m between the voids and GaP, with a largest increase by a factor of 2.6 for the higher porosity material, PA-GaP. For samples much thicker than the extrapolation lengths ($L \gg z_{e,i}$), it is seen from Eq. 6.6 that the relative increase of transmission matches the relative increase of ℓ. Therefore, the dependence of the scattering efficiency on refractive index ratio of one microscopic scattering realization is directly measured.

Also plotted in Fig. 6.9 for comparison are results from effective medium theories, see section 2.6, that is Maxwell Garnett's and Bruggeman's results. In section

2.6.3, scattering by a low concentration of small dielectric spheres in a dielectric host has been treated, see Eq. 2.76. To describe the observed dependence of the transmission on refractive index ratio, see Fig. 6.9, one has to go beyond this limit.

In Bruggeman's approach, which is developed for the aggregate topology (see Fig. 2.5), both dielectric components are treated on the same footing. The dielectric constants are ε_1 and ε_2, with volume fractions of ϕ_1 and ϕ_2 ($\phi_1 + \phi_2 = 1$), respectively. The components are considered to be the scattering entities in the averaged medium itself. The mean free path ℓ is found by summing both contributions to the extinction cross section, see Eq. 2.76, [101]

$$\ell^{-1} \propto \phi_1 \Omega_1 \left[\frac{\varepsilon_1 - \varepsilon_{\rm av}}{\varepsilon_1 + 2\varepsilon_{\rm av}} \right]^2 + \phi_2 \Omega_2 \left[\frac{\varepsilon_2 - \varepsilon_{\rm av}}{\varepsilon_2 + 2\varepsilon_{\rm av}} \right]^2 . \tag{6.9}$$

Here Ω_i ($i = 1,2$) is the typical scattering volume of component *i*, and $\varepsilon_{\rm av}$ the average dielectric constant of the medium known from Eq. 2.72. Equation 6.9 is symmetric under interchange of the components. In the experiment, only the dielectric constant of the air/liquid component, say ε_1, is varied; the dielectric constant of GaP and the volume fractions are fixed. The relative increase of transmission upon filling the pores with a dielectric ε_1, corresponds to the ratio $\ell(\varepsilon_1)/\ell(\varepsilon_1 = 1)$. This ratio turns out to be independent of Ω_1/Ω_2, as a result of the symmetry in Bruggeman's formulation, and is plotted in Fig. 6.9 for the known porosities, $\phi_1 = 35$ and 50 volume-%.

The Maxwell Garnett result applies for spherical scatterers, with dielectric constant ε_1 and volume fraction ϕ_1, in a dielectric background medium with dielectric constant ε_2. The results of section 2.6.3 can be expanded by including the "local-field" correction to the effective polarizability of the sphere, as present in Eqs. 2.68 and 2.69. As the extinction cross section is quadratically dependent on the polarizability, compare Eqs. 2.58 and 2.76, it is found that

$$\ell^{-1} \propto \phi_1 \left[\frac{\varepsilon_1 - \varepsilon_2}{\varepsilon_1 + 2\varepsilon_2} \right]^2 \left[1 - \phi_1 \left(\frac{\varepsilon_1 - \varepsilon_2}{\varepsilon_1 + 2\varepsilon_2} \right) \right]^{-2} . \tag{6.10}$$

Note that Eq. 6.10 in *not* symmetric under interchange of the components, see also the discussion concerning this matter in section 2.6, and hence the result depends on which material is chosen as the dielectric background medium. For the A-GaP sample, with a porosity of 35 volume-%, it is clear that GaP is the background medium; the corresponding result for the relative increase in ℓ is given in Fig. 6.9. However, for PA-GaP, with a porosity of 50 volume-%, the choice is not so obvious. The closest resemblance to the experiment is obtained by taking the air/liquid component as the background ground medium; the result for this choice is shown in Fig. 6.9. It should be stressed that the two effective medium theories are compared to experiment without any adjustable parameters.

As can be seen, the measurements are not quantitatively described by the effective medium models, although qualitatively the dependence of ℓ on refractive index contrast and porosity is captured. As concluded from the SEM pictures of porous GaP, see Fig. 6.5, the aggregate topology (Bruggeman) seems to be the better choice. This indeed holds for PA-GaP, but the results for A-GaP are better described by Maxwell Garnett theory. Furthermore, it is striking that the discrepancy between theory and experiment is largest for the most strongly scattering material, PA-GaP. In fact, the effective medium approach is developed for virtually non-scattering media (long-wavelength limit), and is hence not expected to apply for strongly photonic systems. Nevertheless, most calculations in literature on scattering of light in mixtures [41, 42] are based on effective medium theories. The experiments on porous GaP clearly show that such theories fail for strongly scattering media, prompting the need for new ones.

As observed, a relatively small decrease of refractive index ratio, from 3.26 to 2.12, leads to a large modification of the scattering efficiency, establishing the importance of the refractive index ratio for strongly photonic materials.

CHAPTER 7

Light scattering near the localization transition in GaP networks

Enhanced backscattering of light from anodically and photoanodically etched, macroporous GaP networks is studied. The most strongly scattering material, photoanodically etched GaP, features anomalous rounding of the top of the backscatter cone. The phenomenon cannot be attributed to finite sample size or absorption and is most likely the onset of Anderson localization. A simple model of enhanced backscattering incorporating the scaling theory of localization is presented; a comparison to the measurements is made.

7.1 Introduction

It is well established that the properties of light in multiply scattering media are affected by interference. Important examples are enhanced backscattering [22], short and long-range correlations in the intensity fluctuations [109], universal conductance fluctuations [110], and Anderson localization [18, 84, 111]. To observe these phenomena in full glory, light should be elastically scattered, meaning that light absorption must be negligible. For Anderson localization, *i.e.* inhibition of light propagation due to interference, the material should also be extremely strongly scattering. That is, the transport mean free path, the average distance light propagates before its direction is randomized, should be of the order of the wavelength of light. Such strong scattering can only be attained for large relative variations in refractive index on the length scale of the wavelength. For years, these requirements could not be met for visible light. Only for microwave radiation localization effects were observed [112].

Quite recently a new route towards Anderson localization was worked out, using high refractive index semiconductors in the non-absorbing, sub-bandgap re-

gion. For finely grained GaAs powders, the first observation of strong localization of near infra-red light has been reported [84].

As described in the previous chapter, a new type of strongly scattering material, macroporous GaP networks, was prepared. GaP has a large refractive index of ~ 3.3 and an indirect band gap of 2.24 eV (550 nm) [87], see Fig. 6.1, making it a good candidate for preparing a material which features Anderson localization in the red part of the visible spectrum. Macroporous GaP is the most strongly scattering medium for visible light reported to date and localization effects are anticipated. As enhanced backscattering is expected to be very sensitive to Anderson localization [23], the angular distributions of backscattered intensity are measured for these strongly scattering materials.

7.2 The off-centered rotation technique

The enhanced backscatter cones are recorded using the off-centered rotation technique [113], see Fig. 7.1. The incoming laser light is reflected off a beam splitter onto the scattering sample. The backscattered light is transmitted through the beam splitter and focused on the tip of an optical fiber using a positive lens (focal length = 1 m). The fiber transports the light to a photo-multiplier tube for detection. The sample, beam splitter, and detection optics are placed on a rotating frame, with as the center of rotation R. The center R$'$ of the sample surface is the mirror image of center R, with respect to the plane of the beam splitter. In Fig 7.1 [*right*], the set up is shown after rotation. As the incoming beam is directed at R, the reflected beam off the beam splitter still arrives at the center of the sample surface R$'$ after rotation. With respect to the frame, the direction of detection is fixed. By also rotating the sample around axis R$'$, the incoming beam is kept perpendicular to the sample surface. This co-rotation is obtained by placing the sample on a rotatable disc, which is connected by a twisted band to a disc of the same size that is fixed to the laboratory frame. During rotation, the incoming direction on the sample is fixed and the angular distribution of backscattered light is recorded.

The main advantage of this set up is that the scattered light always follows the same path through the beam splitter and detection optics. The only remaining angular dependence of the set up is in the reflection of the incident beam off the beam splitter. This dependence can be measured accurately by replacing the sample with a detector, and hence can be corrected for.

In order to observe the enhanced backscattering cone, it is essential to average out speckle [114]. The required ensemble averaging is performed by spinning the sample around the detection axis [113]. An efficient ensemble average is obtained by mounted the sample on an unbalanced motor, so that apart from spinning the

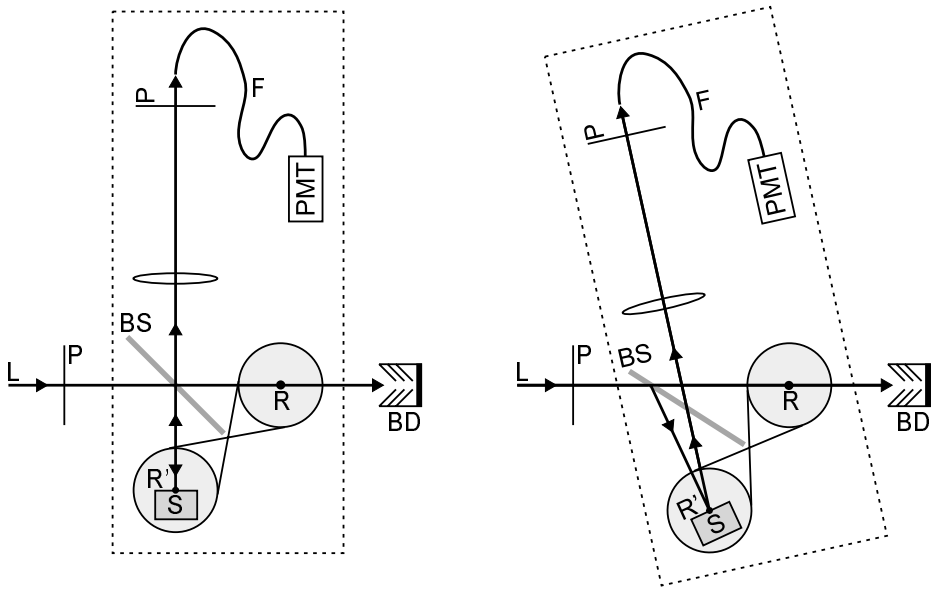

Figure 7.1 An overview of the off-centered rotation set-up to record the angular distribution of backscattered intensity [113]. BD: beam dump; BS: beam splitter; F: multi-mode optical fiber; L: incident laser light; P: polarizer; PMT: photo-multiplier tube; R, R′: rotation axes; S: scattering sample:
[*left*]: The position of the set up for recording the intensity at exact backscattering. All optical components are place on a frame that rotates around R, which is the mirror image in the beam splitter of the center R′ of the front sample surface. As a result, the path from the sample to the detector of the scattered light is independent of rotation angle. The sample co-rotates around R′ to keep the incoming direction perpendicular to the sample surface. The scattered light is focused with a positive lens on the tip of a fiber, which is connected to a photo-multiplier tube for detection. The linear polarizers P select the vertical polarization (s-polarization) channel.
[*right*]: The same set up after rotation over $\sim$ 200 mrad to another detection angle.

sample, it also slightly 'wobbles'.

Linearly polarized light was used to illuminate the samples, and the detection was in the polarization-conserving channel [115]. For these polarization channels also single scattered light is detected, effectively rising the diffuse background [114]. As a result, the enhancement factors of the backscatter cones are not equal to 2. This does not affect the further results.

The accessible angular range is large, 0.9 rad, which is necessary to accurately measure the broad wings of backscatter cones of very strongly scattering samples. The large illumination area of 4 mm in diameter results in a resolution better than

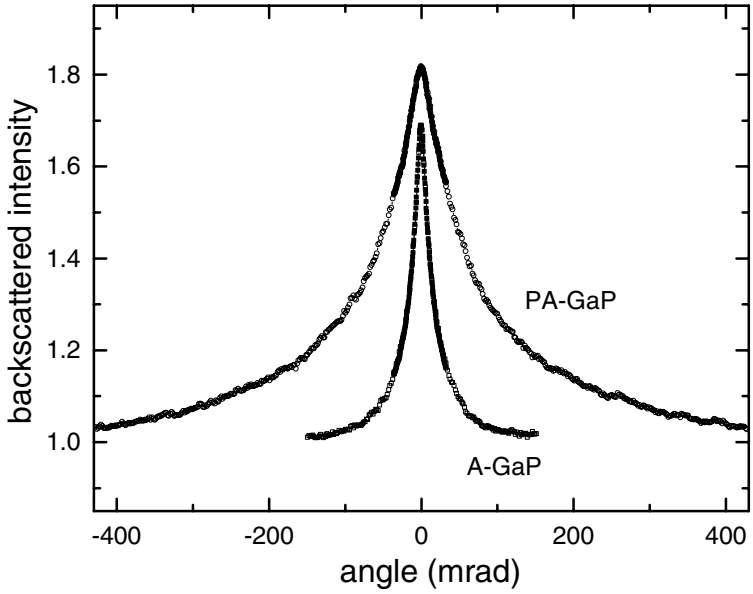

Figure 7.2 The backscattered intensity normalized to the diffuse background as a function of angle for anodically (A-GaP) and photoanodically (PA-GaP) etched GaP, at $\lambda = 685$ nm. From the widths of the cones, incorporating internal reflection corrections, the $k_e\ell$-values are inferred. The narrow cone: A-GaP, $k_e\ell = 10.6 \pm 0.9$. The broad cone: PA-GaP, $k_e\ell = 3.2 \pm 0.4$.

0.4 mrad, enabling precise investigation of the top of the cone. The measurements are performed at $\lambda = 632$, 685, and 780 nm, allowing direct comparison with transmission data from the previous chapter.

7.3 Experimental results

7.3.1 Backscatter cones of A-GaP and PA-GaP

In Fig. 7.2, the backscattered intensities of A-GaP and PA-GaP are shown for $\lambda = 685$ nm; the results are similar for $\lambda = 632$ and 780 nm. The backscattered intensity exhibits a pronounced peak, which arises from constructive interference of time-reversed light scattering paths in the backscattering direction. Short light paths interfere over a considerable range of angles, whereas very long light paths only interfere in exact backscattering. The result is a triangular peak superimposed on the diffuse backscattered intensity [21, 116], known as the enhanced backscatter cone. The width of the cone is determined by the length of the light paths, *i.e.* by the trans-

λ (nm)	$k_e\ell$ (A-GaP)	$k_e\ell$ (PA-GaP)
632	10.3 ± 0.9	3.1 ± 0.4
685	10.6 ± 0.9	3.2 ± 0.4
780	10.8 ± 1.0	4.1 ± 0.5

Table 7.1 The $k_e\ell$-values of anodically (A-GaP) and photoanodically (PA-GaP) etched GaP for λ = 632, 685, and 780 nm, as inferred from the full width at half maximum of the enhanced backscatter cones and using Eq. 7.1. The errors are mainly determined by the estimated error in n_e.

port mean free path. The much broader cone of PA-GaP immediately reflects the stronger scattering of this material. In order to quantitatively determine $k_e\ell$, the inverse measure of scattering efficiency, from these measurements, internal reflection must be taken into account. The diffuse reflection coefficient R of the sample-air interface depends on the effective refractive index of the scattering material n_e [105], giving $R = 0.78 \pm 0.05$ for A-GaP and $R = 0.67 \pm 0.06$ for PA-GaP, see Tab. 6.1. From the full width at half maximum W of the cone the $k_e\ell$-values can be inferred, as [105, 116]

$$k_e\ell \simeq 0.7\, n_e W^{-1}(1-R). \tag{7.1}$$

The $k_e\ell$-values obtained via Eq. 7.1, for λ = 632, 685, and 780 nm, are given in Tab. 7.1. Considering the approximate nature of the internal reflection correction, these values are in good agreement with the transmission results, see Tab. 6.2, establishing PA-GaP as the most strongly scattering material for visible light reported to date.

7.3.2 Filling the pores of PA-GaP with dielectric material

Filling the pores of PA-GaP with 1-dodecanol, which is non-absorbing and has a refractive index of ~ 1.44, lowers the refractive index contrast, resulting in less strong scattering, see Fig. 7.3. This is the first measurement of enhanced backscattering where the effect of refractive index contrast has been investigated for one microscopic scattering realization of the disorder. The alcohol has a convenient melting point of $\sim 26^{\circ}C$ just above room temperature, allowing to fill the samples with liquid and perform the backscatter cone measurements in the solid phase. During the filling procedure the light transmission intensity is monitored, see previous chapter, in order to ensure complete filling. As a result of this filling, the full width at half maximum of the cone narrows by a factor 2.1 ± 0.1, corresponding to an increase in $k_e\ell$ [117]. The observed increase in $k_e\ell$ with a factor of 2.1 ± 0.1

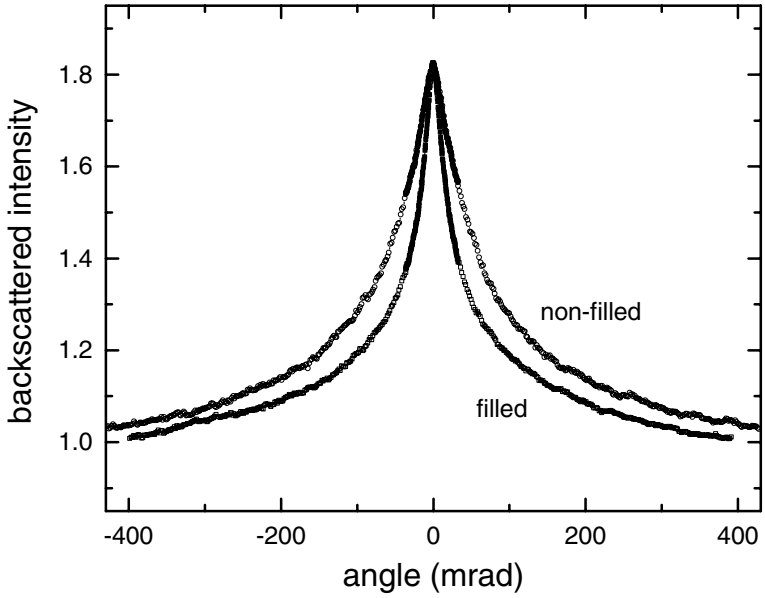

Figure 7.3 The backscattered intensity normalized to the diffuse background as a function of angle for photoanodically etched GaP (PA-GaP) and exactly the same sample filled with 1-dodecanol, for $\lambda = 685$ nm. Due to the decrease in refractive index contrast, the scattering efficiency of filled PA-GaP is lower, reflected by the narrower cone. The cone of non-filled PA-GaP is a factor 2.1 ± 0.1 broader than the filled one.

is in excellent agreement with the increase of transmission upon filling, which is 2.20 ± 0.05, see Fig. 6.9.

7.3.3 Anomalous rounding of the top of the cone

Normally, the top of the enhanced backscatter cone is cusped, resulting from interference of infinitely long light paths. However, close to and in the Anderson localization regime, the top of the backscatter cone is expected to be rounded [23], as especially the long light paths are affected by localization [18, 111]. Inspection of the observed top reveals a clear rounding, see Fig. 7.4. It should be noted that the enhanced backscatter cone can also have a rounded top in the classical regime: absorption [101, 116, 118, 119] and finite sample size [101, 116, 119, 120] present a cut-off on long light paths, which therefore cannot contribute to enhanced backscattering. It is thus essential to study the influence of absorption and finite sample thickness, in order to clearly reveal the presence of Anderson localization.

To investigate this rounding quantitatively, a convenient measure of cone

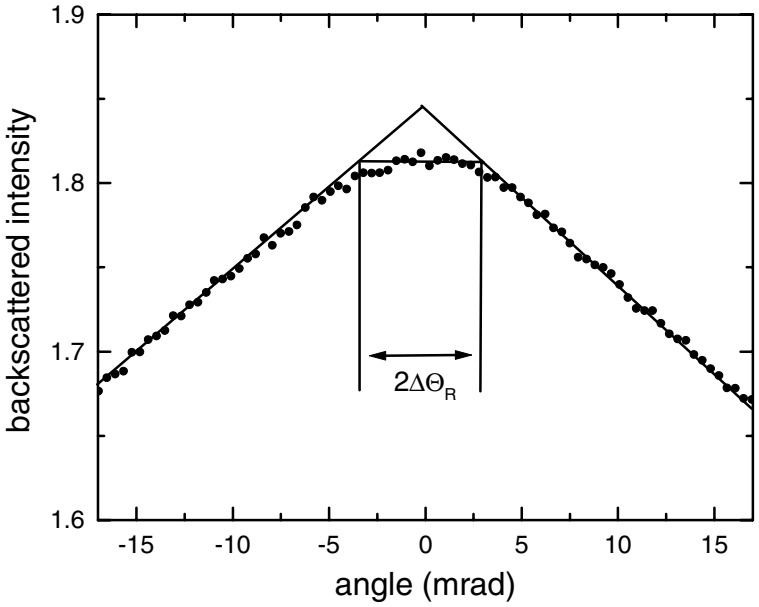

Figure 7.4 The top of the enhanced backscatter cone of a 60 μm-thick photoanodically etched GaP showing a clear rounding, for $\lambda = 685$ nm. $\Delta\Theta_R$ is the measure of cone rounding as defined in the text. Here $\Delta\Theta_R$ is 3.4 ± 0.2 mrad.

rounding is introduced, which is easily extracted from the data. The rounding $\Delta\Theta_R$ is defined as follows: First the wings of the measured enhanced backscatter cone are extrapolated into a triangular cone, representing the cone with no cut-off on long light paths. Then, $2\Delta\Theta_R$ is taken to be the width of the cusped cone at the height of the rounded cone, see Fig. 7.4. This definition is independent of the enhancement factor. In the classical diffusion regime, with absorption length L_a and sample thickness L, small cone roundings ($\Delta\Theta_R \ll W$) can be derived from an explicit formula for the line shape of enhanced backscattering [116]

$$\Delta\Theta_R = \frac{1}{kL_a} \coth\left(\frac{L_e}{L_a}\right). \tag{7.2}$$

Here $k = 2\pi/\lambda$ and $L_e = L + 2z_e$ the effective sample thickness, where z_e is the extrapolation length for a symmetric scattering geometry, see the discussion on z_e in section 6.3.1. For asymmetric geometries, $2z_e$ may be replaced by $(z_{e,1} + z_{e,2})$ in Eq. 7.2. If $L_e \gg L_a$, the rounding is solely determined by absorption: $\Delta\Theta_R = 1/(kL_a)$. Contrary, for $L_e \ll L_a$ the rounding is due to the finite sample size: $\Delta\Theta_R = 1/(kL_e)$. These findings agree with previous derivations [101, 118, 119, 120]. The

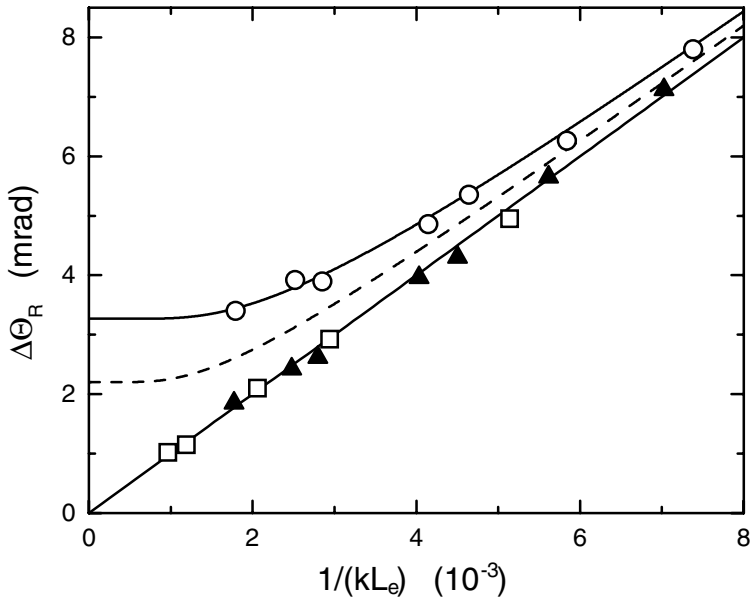

Figure 7.5 The cone roundings $\Delta\Theta_R$ of anodically etched GaP (A-GaP, open squares), photoanodically etched GaP (PA-GaP, open circles), and PA-GaP filled with 1-dodecanol (filled triangles) as a function of inverse effective sample thickness, for λ = 685 nm. The solid straight line is the theoretical prediction from Eq. 7.2 assuming that absorption is negligible ($L_a \gg L_e$), using no adjustable parameters. Only non-filled PA-GaP shows extra rounding for thick samples and is compared to Eq. 7.2, with a tentative absorption length L'_a of $33 \pm 2\,\mu$m (solid curved line). The dashed curve comes from Eq. 7.2 with $L'_a = 48\,\mu$m, the tentative absorption length predicted for filled PA-GaP using diffusion theory and the data for non-filled PA-GaP. Clearly, the dashed curve does not describe the measured cone roundings for PA-GaP filled with 1-dodecanol, excluding absorption as a source for the extra cone rounding of non-filled PA-GaP. The error bars are of the order of the symbol size.

fact that Eq. 7.2 is not symmetric in L_e and L_a reflects the physical difference between path length cut-off due to finite sample size and due to absorption, which are deterministic and probabilistic, respectively [101].

To distinguish the possible mechanisms for cone rounding, enhanced backscatter cones for various sample thicknesses L were measured at λ = 685 nm. The cone roundings $\Delta\Theta_R$ of A-GaP, PA-GaP, and PA-GaP filled with 1-dodecanol are given in Fig. 7.5. Clearly, the cone roundings of A-GaP and filled PA-GaP follow $\Delta\Theta_R = 1/(kL_e)$, and hence can be fully explained by the finite sample thickness. Absorption plays no role for these two types of samples: $L_a \gg L_e$. This is in agreement with transmission measurements, which show no signs of absorption for both

types of material, leading to the conclusion that the (diffuse) absorption length L_a is considerably larger than the thickest samples, that is $L_a \geq 150\ \mu$m for A-GaP and $L_a \geq 80\ \mu$m for PA-GaP, for all three wavelengths.

In contrast, the cone roundings of non-filled PA-GaP do not tend to zero for thick samples, $(1/kL_e) \downarrow 0$. Attempting to interpret this extra cone rounding of PA-GaP as the contribution of absorption, Eq. 7.2 is used to describe the measurements, resulting in a tentative absorption length L'_a of $33 \pm 2\ \mu$m. This contradicts the transmission measurements from which was concluded that $L_a \geq 80\ \mu$m. Moreover, it is also at variance with the observed cone roundings of filled PA-GaP: if the extra cone rounding of non-filled PA-GaP originates from absorption, then filled PA-GaP also absorbs light and hence would likewise show extra cone rounding, which is evidently not the case as the cone roundings of filled PA-GaP follow the straight line in Fig. 7.5. This discrepancy can be made more quantitative using $L_a = \sqrt{\ell_a \ell/3}$ known from diffusion theory [100], where ℓ_a is the material absorption length and ℓ the transport mean free path. Filling increases ℓ (see Fig. 7.3), but leaves ℓ_a unaffected. Consequently, from the tentative absorption length of 33 μm for non-filled PA-GaP, it is found that L'_a for filled PA-GaP would be $\sqrt{2.1} \times 33\ \mu\text{m} \simeq 48\ \mu$m. Comparison of the theoretical curve for this absorption length (Eq. 7.2) with the data for filled PA-GaP shows that an interpretation in terms of absorption fails, see Fig. 7.5. Therefore, it is shown independently that the extra cone rounding for PA-GaP cannot be explained by either absorption or finite sample size.

The effect of extra cone rounding of PA-GaP can be switched off by filling the sample with 1-dodecanol, decreasing the scattering efficiency. Apparently, the extra cone rounding is only observed for the strongest scattering material, closest to the localization transition, and thus the phenomenon is most likely an effect of Anderson localization.

The systematic dependence of the cone roundings on the sample thickness was only studied for λ = 685 nm. However, as can be seen in Fig. 7.5, the cone roundings of the thickest samples alone, already provides information on the presence of extra cone rounding. The cone roundings for the 60 μm-thick PA-GaP and 120 μm-thick A-GaP samples at λ = 632, 685, and 780 nm are presented in Tab. 7.2. Obviously, for all three wavelengths, the cone roundings of A-GaP can be fully explained by the finiteness of the sample thickness; this also holds for the cone rounding of PA-GaP at λ = 780 nm. Extra cone rounding of PA-GaP is observed for both λ = 632 and 685 nm, where the effect is larger for λ = 632 nm. Here, it should be noted that from both the transmission and enhanced backscattering measurements, see Tabs. 6.2 and 7.1, it is known that PA-GaP scatters more efficiently for shorter wavelengths. Thus, if the extra cone rounding originates from Anderson localization, it may come as no surprise that the effect is larger at λ = 632 nm.

	PA-GaP		A-GaP	
λ (nm)	$\Delta\Theta_R$ (mrad)	L_R (μm)	$\Delta\Theta_R$ (mrad)	L_R (μm)
632	4.1 ± 0.3	24 ± 2	0.91 ± 0.14	112 ± 17
685	3.2 ± 0.2	33 ± 2	0.94 ± 0.11	116 ± 13
780	1.9 ± 0.2	65 ± 7	1.01 ± 0.13	123 ± 16

Table 7.2 The cone roundings $\Delta\Theta_R$ and corresponding length scale L_R [$\Delta\Theta_R = 1/(kL_R)$] for the 60 μm-thick PA-GaP and 120 μm-thick A-GaP samples at λ = 632, 685, and 780 nm. The cone roundings of A-GaP at all three wavelengths, and of PA-GaP at 780 nm, originate from the finite sample thickness. For PA-GaP at 632 and 685 nm, extra cone rounding is observed.

7.4 Enhanced backscattering and scaling theory of localization

The scaling theory of localization [111] predicts that the classical diffusion coefficient D_0 is no longer a local quantity, determined by the energy velocity v_e and the transport mean free path ℓ, but instead is length-scale dependent. There exists a coherence length ξ_0 that represents the length scale on which interference effects influence the effective diffusion coefficient. This coherence length diverges upon approaching the localization transition as $\xi_0 = \ell_B^2/(\ell_B - \ell_C)$, where ℓ_B is the Boltzmann mean free path [121] and ℓ_C the critical mean free path. The Boltzmann mean free path is the characteristic mean free path following from the Boltzmann equation [121], and is identical to the transport mean free path in the classical regime. The critical mean free path is related to the Ioffe-Regel criterion [122] for localization: $k_e\ell_C \simeq 1$. Note that in the classical limit, that is $\ell_B \gg \ell_C$, the coherence length ξ_0 equals the Boltzmann mean free path ℓ_B.

For the scale-dependent diffusion coefficient $D(\Lambda)$, where Λ is the length scale under consideration, three regimes can be identified above the transition [111],

$$D(\Lambda) \simeq \begin{cases} D_0 & (\Lambda \leq \ell_B) \\ D_0(\ell_B/\Lambda) & (\ell_B < \Lambda < \xi_0) \\ D_0(\ell_B/\xi_0) & (\Lambda \geq \xi_0). \end{cases} \tag{7.3}$$

This diffusion coefficient is related to the scale-dependent transport mean free path $\ell(\Lambda)$, that is $D(\Lambda) = v_e\ell(\Lambda)/3$. In the localized state of light, below the transition, the diffusion coefficient and hence the transport mean free path is zero for large enough sample thicknesses.

Localization effects can be observed from the scaling behavior of the transmission on sample thickness L. Above the transition, for $\xi_0 > L$, the transport mean

free path is scale-dependent, and hence the total transmission coefficient T reads

$$T \propto \frac{\ell(L)}{L} \simeq \frac{\ell_B^2}{L^2}. \tag{7.4}$$

This $(1/L^2)$-dependence of the transmission is clearly distinct from the classical $(1/L)$-dependence, see Eq. 6.6, and has been reported for very strongly scattering materials [84, 112]. Contrary, for $\xi_0 < L$ and above the transition, the scaling behavior of the transmission on the sample size resumes the classical $(1/L)$-dependence,

$$T \propto \frac{\ell(L)}{L} \simeq \frac{\ell_B(\ell_B/\xi_0)}{L}, \tag{7.5}$$

where $\ell_B(\ell_B/\xi_0)$ is known as the *renormalized* transport mean free path. Below the transition, the transmission decreases exponentially for sample thicknesses larger than the localization length L_{loc} [18], that is

$$T \propto \exp(-L/L_{loc}). \tag{7.6}$$

Localization effects are also expected to be observable in enhanced backscattering [23], as the angular distribution of backscattered light reflects the path length distribution in the scattering medium. The wings of the backscatter cone correspond to short light scattering paths, the top to the long ones. Scaling of the diffusion coefficient, see Eq. 7.3, thus leads to a modified line shape of the backscatter cone.

In the classical diffusion regime, the enhanced backscattering intensity $\gamma_c[q\ell]$ for semi-infinite, non-absorbing media is given by [116]

$$\gamma_c[q\ell] = \frac{3}{2q\ell}\frac{1+q\ell-\exp(-2q\ell\tau_e)}{(1+q\ell)^2}, \tag{7.7}$$

where $q = k|\sin\theta|$ is the transverse wavevector of the scattered light at angle θ, and $\tau_e = (2/3)$ the extrapolation length ratio for zero reflectivity. A simple approach to incorporate the scaling theory of localization in enhanced backscattering, is replacing ℓ in Eq. 7.7 by a q-dependent transport mean free path $\ell(q)$ [23], which follows from Eq. 7.3 and reads

$$\ell(q) \simeq \begin{cases} \ell_B & (q \geq \ell_B^{-1}) \\ \ell_B^2 q & (\ell_B^{-1} > q > \xi_0^{-1}) \\ \ell_B^2/\xi_0 & (q \leq \xi_0). \end{cases} \tag{7.8}$$

The three regimes can be captured in a single function by writing

$$\ell(q) \simeq \frac{\ell_B^2}{\xi_0}\left[\frac{1+q\xi_0}{1+q\ell_B}\right], \tag{7.9}$$

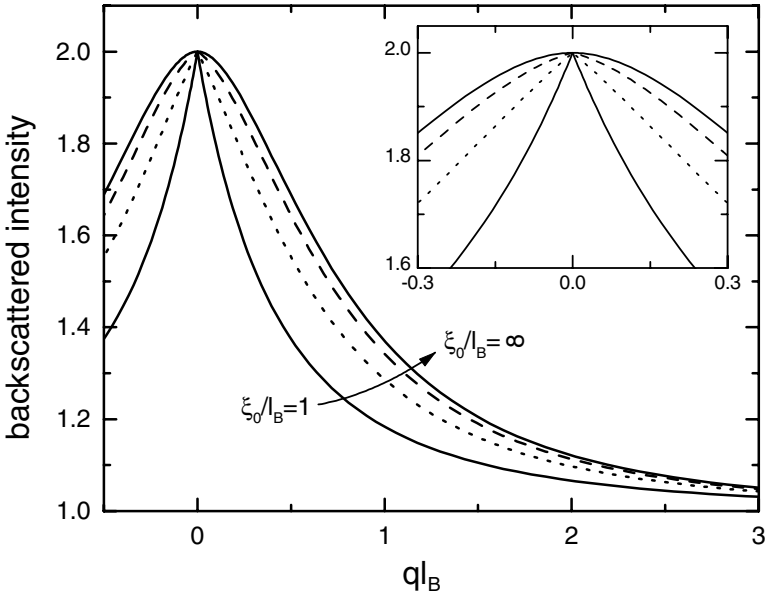

Figure 7.6 The normalized enhanced backscatter cones incorporating a simplified scaling theory of localization as a function of $q\ell_{\rm B}$, for $\xi_0/\ell_{\rm B} = 1, 3, 10$, and ∞. The cusped classical diffusion cone is regained for $\xi_0/\ell_{\rm B} = 1$, whereas at the localization transition ($\xi_0/\ell_{\rm B} = \infty$) the top of the backscatter cone is rounded. The initial slope at the top of the cone is determined by renormalized transport mean free path $\ell_{\rm B}(\ell_{\rm B}/\xi_0)$.

which is the form of $\ell(q)$ that is used in the remainder of this chapter. The modified line shape of the backscatter cone due to localization, $\gamma_c[q\ell(q)]$, is shown in Fig. 7.6, for $\xi_0/\ell_{\rm B} = 1, 3, 10$, and ∞. The slope at zero angle is determined by the renormalized transport mean free path $\ell_{\rm B}(\ell_{\rm B}/\xi_0)$, instead of $\ell_{\rm B}$ [21] ($\xi_0 = \ell_{\rm B}$ in the classical limit). The wings of the backscatter cone are hardly affected by localization, as the corresponding short light scattering paths are not renormalized [111]. Upon approaching localization ($\xi_0/\ell_{\rm B}$ going from 1 to ∞), the top of the cone becomes less cusped and ultimately parabolic (rounded).

7.4.1 Comparison to the experimental results

In the experiments on porous GaP, the predicted weakly cusped cone of a semi-infinite medium for finite ξ_0 is not observed; the measured cones are rounded. In this respect, it should be noted that the $(1/L)$-scaling of the transmission measurements implies that the coherence length ξ_0 is in the order of, or smaller than the thinnest samples, that is $\xi_0 \leq 5$ μm, see Eq. 7.5. However, even a ξ_0 of 5 μm

can lead to a large renormalization of the diffusion constant, as $\ell_B \simeq 0.5\ \mu$m. For $\xi_0/\ell_B = 10$, the top of the backscatter cone is still slightly cusped, see Fig. 7.6, but such a small discontinuity in the slope is experimentally difficult to observe. In the measurements, the cusp is probably blurred by the remnant noise, as also by the finiteness of even the thickest samples [23].

In general, it is remarkable that the linear dependence of the total transmission with inverse sample thickness is observed, see Eq. 6.6 and 7.5, whereas in enhanced backscattering the onset of localization is presumably already detected. It should be stressed that in enhanced backscattering the angular distribution of backscattered light for different sample thicknesses is measured, whereas in total transmission only the thickness is varied. Consequently, transmission measurements give less information on the path length distribution and hence on localization, indicating that enhanced backscattering is the more sensitive probe.

Although qualitatively the presented model for incorporating localization in enhanced backscattering describes the experiment, a quantitative comparison cannot be made. For example, diffuse internal reflection [104, 105] in combination with scaling theory of localization has not yet been studied. As it is essential to consider diffuse internal reflection for a quantitative description of enhanced backscattering in the classical diffusion regime, it is expected to be equally important in the localization regime.

REFERENCES

[1] Lord Rayleigh, Phil. Mag. **41**, 107, 274 (1871); Phil. Mag. **47**, 375 (1899).

[2] H.C. van der Hulst, *Light Scattering by Small Particles*, (Dover, New York, 1981), 1st ed.

[3] D. Pidgeon, Nature **37**, 440 (1888).

[4] R. Wilson, Monthly Notices Roy. Astron. Soc. **111**, 478 (1951); S. Melmore, Observatory **73**, 105 (1953).

[5] M. Minnaert, *De Natuurkunde van 't Vrije Veld; Licht en Kleur in het Landschap*, (Thieme, Zutphen, 1937), 1st ed; later reissued in English: M.G.J. Minnaert, *Light and Color in the Outdoors*, (Springer, New York, 1993).

[6] H. Ghiradella, Hairs, Bristles, and Scales, *Microscopy Anatomy of Invertebrates*, Vol. 11A: Insecta, Ch. 11, (Wiley-Liss, London, 1998).

[7] *Webster's Encyclopedic Unabridged Dictionary of the English Language*, (Random House, New York, 1994).

[8] E. Yablonovitch, Phys. Rev. Lett. **58**, 2059 (1987); E. Yablonovitch and T.J. Gmitter, Phys. Rev. Lett. **63**, 1950 (1989); S. John and T. Quang, Phys. Rev. A **50**, 1764 (1994); see also for overviews: topical issue on *Developement and Applications of Materials Exhibiting Photonic Band Gaps*, J. Opt. Soc. Am. B **10**, 279-413 (1993); *Proceeding of the Photonic Band GaP Materials, Crete, 1995*, edited by C.M. Soukoulis, NATO ASI, Ser. E., Vol. 315 (Kluwer, Dordrecht, 1996).

[9] F. De Martini and G.R. Jacobovitz, Phys. Rev. Lett. **60**, 1711 (1988); Y. Yamamoto and R.E. Slusher, Phys. Today **46** (6), 66 (1993).

[10] G. Nienhuis and C.Th.J. Alkemade, Physica **81C**, 181 (1976).

[11] R. Loudon, *The quantum theory of light*, (Clarendon Press, Oxford, 1973), 1st ed.

[12] C. Kittel, *Introduction to Solid State Physics*, (Wiley, New York, 1976), 5th ed.

[13] S.M. Barnett, B. Huttner, R. Loudon, and R. Matloob, J. Phys. B: At. Mol. Opt. Phys. **29**, 3763 (1996).

[14] C.J.F. Böttcher, *Theory of Electric Polarization*, (Elsevier, Amsterdam, 1973), Vol. I.

[15] L. Onsager, J. Am. Chem. Soc. **58**, 1486 (1936).

[16] P. de Vries and A. Lagendijk, Phys. Rev. Lett. **81**, 1381 (1998).

[17] F.J.P. Schuurmans, D.T.N. de Lang, G.H. Wegdam, R. Sprik, and A. Lagendijk, Phys. Rev. Lett. **80**, 5077 (1998).

[18] P.W. Anderson, Phys. Rev. **109**, 1492 (1958); S. John, Phys. Rev. Lett. **53**, 2169 (1984); P.W. Anderson, Philos. Mag. B **52**, 505 (1985); C.M. Soukoulis, E.N. Economou, G.S. Grest, and M.H. Cohen, Phys. Rev. Lett. **62**, 575 (1989); S. John, Phys. Today **44**(5), 32 (1991).

[19] F.J.P. Schuurmans, D. Vanmaekelbergh, J. van de Lagemaat, and A. Lagendijk, Science **284**, 141 (1999).

[20] F.J.P. Schuurmans, M. Megens, D. Vanmaekelbergh, and A. Lagendijk, Phys. Rev. Lett. **83**, 2183 (1999).
[21] E. Akkermans, P.E. Wolf, and R. Maynard, Phys. Rev. Lett. **56**, 1471 (1986).
[22] Y. Kuga and A. Ishimaru, J. Opt. Soc. Am. A **8**, 831 (1984); M.P. van Albada and A. Lagendijk, Phys. Rev. Lett. **55**, 2692 (1985); P.E. Wolf and G. Maret, Phys. Rev. Lett. **55**, 2696 (1985).
[23] B. Berkovits and M. Kaveh, Phys. Rev. B **36**, 9322 (1987); I. Edrei and M.J. Stephen, Phys. Rev. B **42**, 110 (1990).
[24] J.D. Jackson, *Classical Electrodynamics*, (John Wiley & Sons, New York, 1975), 2nd ed.
[25] A. Lagendijk and B.A. van Tiggelen, Phys. Rep. **270**, 143 (1996).
[26] E. Fermi, Rev. Mod. Phys. **32**, 87 (1932).
[27] P. de Vries, D.V. van Coevorden, and A. Lagendijk, Rev. Mod. Phys. **70**, 447 (1998).
[28] M. Born and E. Wolf, *Principles of Optics*, (Cambridge Univ. Press, Cambridge, 1997), 6th ed.
[29] D.E. Aspnes, Am. J. Phys. **50**, 704 (1982).
[30] C. Tarrio and S.E. Schnatterly, Mod. Phys. Lett. B **5**, 1479 (1991); S.E. Schnatterly and C. Tarrio, Rev. Mod. Phys. **64**, 619 (1992).
[31] O.F. Mossotti, Mem. Soc. Sci. Modena **24**, 49 (1850).
[32] R. Clausius, *Die Mechanische Behandlung der Elektrizität*, (Viewig, Braunchwieg, 1879), 2nd ed.
[33] L. Lorenz, Wiedem. Ann. **11**, 70 (1880).
[34] H.A. Lorentz, Wiedem. Ann. **9**, 641 (1880).
[35] P. Debye, Phys. Z. **13**, 97 (1912).
[36] J. de Goede and P. Mazur, Physica **58**, 568 (1972).
[37] A. Lagendijk, B. Nienhuis, B.A. van Tiggelen, and P. de Vries, Phys. Rev. Lett. **79**, 657 (1997).
[38] B.U. Felderhof, G.W. Ford, and E.G.D. Cohen, J. Stat. Phys. **33**, 241 (1983).
[39] J.C.M. Garnett, Philos. Trans. R. Soc. Lond. **203**, 385 (1904).
[40] D.A.G. Bruggeman, Ann. Physik (Leipz.) **24**, 636 (1935).
[41] W. Lamb, D.M Wood, N.W. Ashcroft, Phys. Rev. B **21**, 2248 (1980).
[42] R. Landauer, Electrical Transport and Optical Properties of Inhomogeneous Media, edited by J.C. Garland and D.B. Tanner, AIP Conf. Proc. No. 40 (AIP, New York, 1978); S. Datta, C.T. Chan, K.M. Ho, C.M. Soukoulis, Phys. Rev. B **48**, 14936 (1993); K. Busch and C.M. Soukoulis, Phys. Rev. Lett. **75**, 3442 (1995).
[43] C.F. Bohren and D.R. Huffman, *Absorption and Scattering of Light by Small Particles*, (Wiley, New York, 1983).
[44] A. Einstein, Z. Physik **18**, 121 (1917).
[45] E.M. Purcell, Phys. Rev. **69**, 681 (1946).
[46] K.H. Drexhage, J. Lumin. **1-2**, 693 (1970); K.H. Drexhage in *Progress in Optics*, edited by E. Wolf, (North-Holland, Amsterdam, 1974), Vol. XII.
[47] P.W. Milonni and P.L. Knight, Opt. Commun. **9**, 119 (1973); D. Kleppner, Phys. Rev. Lett. **47**, 233 (1981).
[48] P. Goy, J.M. Raimond, M. Gross, and S. Haroche, Phys. Rev. Lett. **50**, 1903 (1983);

R.G. Hulet, E.S. Hilfer, and D. Kleppner, Phys. Rev. Lett. **55**, 2137 (1985); W. Jhe, A. Anderson, E.A. Hinds, D. Meschede, L. Moi, and S. Haroche, Phys. Rev. Lett. **58**, 666 (1987); D.J. Heinzen, J.J. Childs, J.E. Thomas, and M.S. Feld, Phys. Rev. Lett. **58**, 1320 (1987); F. De Martini, G. Innocenti, G.R. Jacobovitz, and P. Mataloni, Phys. Rev. Lett. **59**, 2955 (1987).

[49] C.K. Carniglia, L. Mandel, and K.H. Drexhage J. Opt. Soc. Am. **62**, 479 (1972); R.E. Kunz and W. Lukosz, Phys. Rev. B **21**, 4814 (1980); E. Snoeks, A. Lagendijk, and A. Polman, Phys. Rev. Lett. **74**, 2459 (1995).

[50] C.K. Carniglia and L. Mandel, Phys. Rev. D **3**, 280 (1971); H. Khosravi and R Loudon, Proc. R. Soc. London A **433**, 337 (1991).

[51] J.J. Maki, M.S. Malcuit, J.E. Sipe, and R.W. Boyd, Phys. Rev. Lett. **67**, 972 (1991).

[52] R.J. Glauber and M. Lewenstein, Phys. Rev. A **43**, 467 (1991).

[53] J. Knoester and S. Mukamel, Phys. Rev. A **40**, 7065 (1989); S.M. Barnett, B. Huttner, and R. Loudon, Phys. Rev. Lett. **68**, 3698 (1992); S.-T. Ho and P. Kumar, J. Opt. Soc. Am. B **10**, 1620 (1993); G. Juzeliũnas and D.L. Andrews, Phys. Rev. **B** 49, 8751 (1994); P.W. Milonni, J. Mod. Opt. **42**, 1991 (1995); G. Juzeliũnas, Phys. Rev. A **55**, R4015 (1997); C. Cao, W. Long, and H. Cao, Phys. Lett. A **232**, 15 (1997).

[54] G.L.J.A. Rikken and Y.A.R.R Kessener, Phys. Rev. Lett. **74**, 880 (1995).

[55] P. Lavallard, M. Rosenbauer, and T. Gacoin, Phys. Rev. A **54**, 5450 (1996).

[56] K.H. Drexhage, Structure and Properties of Laser Dyes, *Dye Lasers*, Topics in Applied Physics, Vol. I, (Springer-Verlag, Berlin, 1977) ed. F.P. Schäfer, 2nd ed.; U. Brackmann, *Lambdachrome Laser Dyes*, (Lambda Physik, Göttingen, 1994), 2nd ed.

[57] L.C. Thompson, Complexes, *Handbook on the Physics and Chemistry of Rare Earths*, Vol. 3, (North Holland, Amsterdam, 1979), eds. K.A. Gschneider and L.R. Eyring.

[58] W.DeW. Horrocks, Jr. and D.R. Sudnick, J. Am. Chem. Soc. **101**, 334 (1978); W.DeW. Horrocks, Jr. and D.R. Sudnick, Acc. Chem. Res. **14**, 384 (1981).

[59] See for example: M. Gerloch, *Orbitals, terms and states*, (Wiley, New York, 1986); B.H. Bransden and C.J. Joachain, *Physcis of atoms and molecules*, (Longman, Essex, 1991).

[60] B.R. Judd, Phys. Rev. **127**, 750 (1962); G.S. Ofelt, J. Chem. Phys. **37**, 511 (1962).

[61] N. Sabbatini, M. Guardigli, J.-M. Lehn, Coord. Chem. Rev. **123**, 201 (1993).

[62] W.T. Carnall, The absorption and fluorescence spectra of rare earth ions in solution, *Handbook on the Physics and Chemistry of Rare Earths*, Vol. 3, (North Holland, Amsterdam, 1979), eds. K.A. Gschneider and L.R. Eyring.

[63] B. Henderson and G.F. Imbush, *Optical Spectroscopy of Inorganic Solids* (Clarendon Press, Oxford, 1989), 1st ed.

[64] See for example: T.E. Peters, R.G. Pappalardo, and R.B. Hunt, Jr., Lamp phosphers, *Solid State Luminescence, Theory, Materials, and Devices*, (Chapman & Hall, London, 1993), ed. A.H. Kitai; G. Blasse and B.C. Grabmaier, *Luminescent Materials*, (Springer Verlag, Berlin, 1994).

[65] D.L. Dexter, J. Chem. Phys. **21**, 836 (1953); T. Förster, Discuss. Faraday. Soc. **27**, 7 (1959).

[66] Aldrich: Resolve-Al^{TM} EuFOD, europium tris(6,6,7,7,8,8,8-heptafluor-2,2-dimethyl-3,5-octanedionate).
[67] Aldrich: europium tris[3-(heptafluoropropylhydoxymethylene)- (+)-camphorate].
[68] S. Freed and S.I. Weissman, Phys. Rev **60**, 440 (1941); R.E. Kunz and W. Lukosz, Phys. Rev. B **21**, 4814 (1980).
[69] J.M.F. van Dijk and M.F.H. Schuurmans, J. Chem. Phys. **78**, 5317 (1983); M.F.H. Schuurmans and J.M.F. van Dijk, Physica **123B**, 131 (1984).
[70] W. Siebrand, J. Chem. Phys. **46**, 440 (1967).
[71] M.P. Oude Wolbers, F.C.J.M. van Veggel, B.H.M. Snellink-Ruël, J.W. Hofstraat, F.A.J. Geurts, and D.N. Reinhoudt, J. Am. Chem. Soc. **119**, 138 (1997).
[72] J.L. Kropp and M.W. Windsor, J. Chem. Phys. **39**, 2769 (1963); J.L. Kropp and M.W. Windsor, J. Chem. Phys. **42**, 1599 (1965); J.L. Kropp and M.W. Windsor, J. Chem. Phys. **39**, 761 (1966).
[73] The Raman measurements were performed at the Condensed Matter Department of the Debye Instituut, Universiteit Utrecht, by M. van der Voort. The 514.5 nm line of an Argon laser (Spectra Physics, 2060) was used to probe the molecular vibrations. The Raman scattered light was send through a triple stage spectrometer and detected by a liquid N_2 cooled CCD-camera (Princeton Instruments).
[74] W.R. Dawson and J.L. Kropp, J. Opt. Soc. Am. **55**, 822 (1965).
[75] *Landolt-Börnstein, Zahlenwerte und Funktionen, Optische Konstanten*, II Band, 8. Teil (Springer-Verlag, Berlin, 1962), eds. J. Bartels *et al.*
[76] International Union of Pure and Applied Chemistry (IUPAC), *International Thermodynamic Tables of the Fluid State*, Vol. 3: Carbon Dioxide, (Pergamon, Oxford, 1976), eds. S. Angus, B. Armstrong, and K.M. de Reuck.
[77] Y. Lin, R.D. Brauer, K.E. Laintz, and C.M. Wai, Anal. Chem. **65**, 2549 (1993).
[78] H.W.L. Bruckman, A.C. Michels, and N.J. Trappeniers, Physica **139A**, 175 (1986); H. Bruckman, *Light Scattering near the Critical Double Point of the System Neon-Xenon*, Ph.D. thesis, Universiteit van Amsterdam (1989).
[79] R.H.J. Kop and R. Sprik, Rev. Sci. Instrum. **66**, 5459 (1995); R.H.J. Kop, P. de Vries, R. Sprik, and A. Lagendijk, Phys. Rev. Lett. **79**, 4369 (1997); H.J. Kop, *Time-resolved interferometry on metals and disordered systems*, Ph.D. thesis, Universiteit van Amsterdam (1998).
[80] G. Herzberg, *Infrared and Raman Spectra of Polyatomic Molecules*, (Lancaster Press, Lancaster, 1951), 5th ed., p. 535.
[81] This was pointed out by Prof. Dr. A. Meijerink from the Universiteit Utrecht. Furthermore, he noted that for Eu^{3+} ions which mainly luminesce via the $^5D_0 \rightarrow {}^7F_2$ transition, the *radiative* lifetime is approximately 1.5 ms. And hence, he concluded that luminescence quantum efficiency of $Eu(fod)_3$ in CO_2 is higher than 0.9 (90 %), and no water molecules are present.
[82] F. De Martini, M.Marrocco, P. Mataloni, L. Crescentini, and R. Loudon, Phys. Rev. A **43**, 2480 (1991).
[83] B.T. Holland, C.F. Blanford, A. Stein, Science **281**, 538 (1998); J.E.G.J Wijnhoven and W.L. Vos, Science **281**, 802 (1998).
[84] D.S. Wiersma, P. Bartolini, A. Lagendijk, R. Righini, Nature **390**, 671 (1997).

[85] U. Grüning, V. Lehmann, and C.M. Engelhardt, Appl. Phys. Lett. **66**, 3254 (1996); U. Grüning, V. Lehmann, S. Ottow, K. Busch, Appl. Phys. Lett. **68**, 747 (1996).
[86] F. Wooten, *Optical properties of solids*, (Academic Press, New York, 1972), 1st ed.
[87] J.I. Pankove, *Optical processes in semiconductors*, (Dover, New York, 1975); 1st ed.; D.E. Aspnes and A.A. Studna, Phys. Rev. B **27**, 985 (1983); *CRC Handbook of Laser Science and Technology*, Vol. III: Optical Materials, Part 1: Nonlinear Optical Properties/Radiation Damage, (CRC Press, Baco Raton, 1986), ed. M.J. Weber.
[88] J. Gómez Rivas, R. Sprik, C.M. Soukoulis, K. Busch, and A. Lagendijk, accepted for publication in Europhys. Lett.
[89] J. Gómez Rivas has prepared this Ge powder. His graduate research focuses on the preparation and light scattering properties of semiconducting powders, like Si, Ge, GaAs, and ZnTe, which could display Anderson localization.
[90] Philips Research Laboratories (Eindhoven, The Netherlands) is acknowledged for kindly supplying the GaP crystals.
[91] B.D. Chase and D.B. Holt, J. Electrochem. Soc. **119**, 314 (1972).
[92] B.H. Erné, D. Vanmaekelbergh, and J.J. Kelly, Adv. Matter. **7**, 739 (1995); B.H. Erné, *High Quantum Yield III-V Photoanodes*, Ph.D. thesis, Universiteit Utrecht (1995).
[93] F. Iranzo Marín, M.A. Hamstra, and D. Vanmaekelbergh, J. Electrochem. Soc. **143**, 1137 (1996).
[94] S.M. Sze, *Physics of Semiconductor Devices*, (Wiley, New York, 1981), 2nd ed.
[95] C. Zener, Proc. R. Soc. London **145**, 523 (1934).
[96] D. Vanmaekelbergh and W.P. Gomes, J. of Phys. Chem. **94**, 1571 (1990).
[97] D. Vanmaekelbergh and L. van Pieterson, Phys. Rev. Lett. **80**, 821 (1998).
[98] W. Bresser, P. Boolchand, and P. Suranyi, Phys. Rev. Lett. **56**, 2493 (1986).
[99] B.E. Warren, X-ray Diffraction, (Dover, New York, 1990).
[100] A. Ishimaru, Wave Propagation and Scattering in Random Media, Vols. I and II, (Academic, NewYork, 1978); A.Z. Genack, Phys. Rev. Lett. **58**, 2043 (1987).
[101] P. Sheng, Introduction to Wave Scattering, Localization, and Mesoscopic Phenomena, (Academic, San Diego, 1995).
[102] M.P. van Albada, B.A. van Tiggelen, A. Lagendijk, and A. Tip, Phys. Rev. Lett. **66**, 3132 (1991).
[103] D.J. Durian, Phys. Rev. E **50**, 857 (1994).
[104] A. Lagendijk, R. Vreeker, and P. de Vries, Phys. Lett. A **136**, 81 (1989).
[105] J.X. Zhu, D.J. Pine, and D.A. Weitz, Phys. Rev. A **44**, 3948 (1991).
[106] N. Garcia, A.Z. Genack, and A.A. Lisyansky, Phys. Rev. B **46**, 14475 (1992).
[107] P.N. den Outer and A. Lagendijk, Optics Comm. **103**, 169 (1993); P.N. den Outer, *Multiple light scattering in random discrete media, Coherent backscattering and imaging*, Ph.D. thesis, Universiteit van Amsterdam (1995).
[108] D.S. Wiersma, M.P. van Albada, B.A. van Tiggelen, and A. Lagendijk, Phys. Rev. Lett. **74**, 4193 (1995).
[109] S. Feng, C. Kane, P.A. Lee, and A.D. Stone, Phys. Rev. Lett. **61**, 834 (1988); I. Freund, M. Rosenbluh, and S. Feng, Phys. Rev. Lett. **61**, 2328 (1988); N. Garcia and A.Z. Genack, Phys. Rev. Lett. **63**, 1678 (1989); M.P. van Albada, J.F. de Boer,

and A. Lagendijk, Phys. Rev. Lett. **64**, 2787 (1990); A.Z. Genack, N. Garcia, and W. Polkosnik, Phys. Rev. Lett. **65**, 2129 (1990); J.F. de Boer, M.C.W. van Rossum, M.P. van Albada, Th.M. Nieuwenhuizen, and A. Lagendijk, Phys. Rev. Lett. **73**, 2567 (1994).

[110] F. Scheffold and G. Maret, Phys. Rev. Lett. **81**, 5800 (1998).

[111] E. Abrahams, P.W. Anderson, D.C. Licciardello, and T.V. Ramakrishnan, Phys. Rev. Lett. **42**, 673 (1979).

[112] N. Garcia and A.Z. Genack, Phys. Rev. Lett. **66**, 1850 (1991); A.Z. Genack and N. Garcia, Phys. Rev. Lett. **66**, 2064 (1991).

[113] D.S. Wiersma, M.P. van Albada, and A. Lagendijk, Rev. Sci. Instrum. **66**, 5473 (1995); D.S. Wiersma, *Light in strongly scattering amplifying random media*, Ph.D. thesis, Universiteit van Amsterdam (1995).

[114] S. Etemad, R. Thompson, and M.J. Andrejco, Phys. Rev. Lett. **57**, 575 (1986).

[115] The circular polarization channel was not used, as for the large angular range the required quarter-wave plate causes undesired polarization mixing [113].

[116] M.B. van der Mark, M.P. van Albada, and A. Lagendijk, Phys. Rev. B **37**, 3575 (1988); M.B van der Mark, *Propagation of light in disordered media: a search for Anderson localization*, Ph.D. thesis, Universiteit van Amsterdam (1990).

[117] Although the effective refractive index n_e slightly increases upon filling, the decrease in width of the backscatter cone matches the increase in $k_e\ell$, as correspondingly the diffuse reflection coefficient R also increases.

[118] P.E. Wolf, G. Maret, E. Akkermans, and R. Maynard, J. Phys. France **49**, 63 (1988).

[119] S. Etemad, R. Thompson, M.J. Andrejco, S. John, and F.C. MacKintosh, Phys. Rev. Lett. **59**, 1420 (1987).

[120] I. Edrei and M. Kaveh, Phys. Rev. B **35**, 6461 (1987).

[121] Z.Q. Zhang and P. Sheng, Wave Diffusion and Localization isn Random Composites, in *Scattering and Localization of Classical Waves in Random Media*, (World Scientific, Singapore, 1990), ed. P. Sheng; B.A. van Tiggelen, *Multiple Scattering and Localization of Light*, Ph.D. thesis, Universiteit van Amsterdam (1992).

[122] A.F. Ioffe and A.R. Regel, Prog. Semicond. **4**, 237 (1960).

SUMMARY

In this thesis the properties of light in complex dielectrics are described, with the two general topics of "modification of spontaneous emission" and "Anderson localization of light". The first part focuses on the spontaneous emission rate of an excited atom in a dielectric host with variable refractive index, with the aim to identify which local-field correction applies to spontaneous emission. The second part deals with the propagation of visible light in a medium with extremely strong scattering, close to the Anderson localization transition. Both spontaneous emission and scattering of light originate from the complex dynamic optical polarizability, as is shown in chapter 2. This chapter serves as a concise tutorial on the interaction of light with complex dielectrics, in the course of which emphasis is put on the microscopic origin of the macroscopic dielectric function. Several non-standard derivations of the dielectric function, or equivalently the refractive index, including local-field corrections are presented. The local-field correction captures the modification of the local electric field at the site of an atom, or polarizable dipole, in the dielectric due to the surrounding dipoles. A connection is made to the propagation of light in mixtures of dielectrics. Various effective medium theories – like the Lorentz-Lorenz, Maxwell Garnett, and Bruggeman theory – for the average dielectric constant are presented. Scattering of light by such mixtures is shown to be related to the quasi-static dielectric function.

In chapter 3, the spontaneous emission of an impurity atom in an otherwise homogeneous dielectric is considered. Local-field corrections modify the spontaneous emission rate. However, until recently it was unclear which correction should apply. Using the Onsager-Böttcher approach, and identifying substitutional and interstitial impurities, the well-known empty-cavity and Lorentz local-field factors are obtained, respectively. For fluids, the substitutional case is predicted to occur prevalently.

In chapter 4, the criteria for selecting a suitable luminescent system, that is the radiating molecule plus dielectric host, to study local-field effects on spontaneous emission are discussed, resulting in the choice for europium complexes dissolved in alcohols with varying refractive indices. The luminescence quantum efficiency plays an important role in comparing the experimental results to the theory of chapter 3, and is hence considered in more detail. Experimental results are presented on $Eu(hfc)_3$ in (deuterated) methanol, and on $Eu(fod)_3$ in a series of (deuterated) alcohols and mixtures hereof. The hfc-complex turns out to be chemically unstable in

methanol, whereas $Eu(fod)_3$ is stable in alcohols, making the latter more suitable. Unfortunately, small variations in the local environment of $Eu(fod)_3$ complex upon changing the host (alcohol), blur most of the local-field effect on spontaneous emission.

Experiments on the spontaneous emission rate of $Eu(fod)_3$ in dense supercritical CO_2 are presented in chapter 5. The advantage of taking a supercritical gas as the dielectric host, instead of a series of alcohols, is in the variation of the refractive index by only varying the pressure of the gas, which leaves the type of molecules of the host unchanged. The refractive index ranges from 1.00 to 1.27 by increasing the pressure up to 1100 bar. Accordingly, the spontaneous emission rate changes. Local-field effects on spontaneous emission are clearly observed in these experiments. The empty-cavity model is found to apply, settling the discussion on which local-field correction applies to spontaneous emission.

In chapter 6, the method of preparation and the optical transmission properties of new type of strongly scattering material, macroporous gallium phosphide, are reported. A photo-assisted electrochemical etching technique was exploited to fabricate macropores in single crystalline GaP with variable porosity. GaP is ideal for making a strongly photonic material for visible light, as it has a large refractive index of 3.3 and is transparent for sub-bandgap light, that is for wavelengths longer than 550 nm. Scanning electron microscopy and X-ray diffraction experiments confirm that the material consists of three dimensional, interconnected random networks with pore sizes of about 150 nanometers. Optical transmission measurements demonstrate that the non-absorbing, disordered structures strongly scatter light. The photonic strength is controlled by filling the pores with liquids of different refractive index, allowing to investigate the importance of refractive index contrast for the scattering efficiency in the interesting regime of strong scattering. Macroporous GaP filled with air has the highest scattering efficiency for visible light reported to date.

In chapter 7, measurements are described on enhanced backscattering of light off the GaP networks. The most strongly scattering material, photoanodically etched GaP, features anomalous rounding of the top of the backscatter cone. The phenomenon cannot be attributed to finite sample size or absorption and is most likely the onset of Anderson localization of visible light. A simple model of enhanced backscattering incorporating the scaling theory of localization is presented; a comparison to the measurements is made.

SAMENVATTING

De omslag van dit proefschrift laat een zonsopgang aan een Canadees meer zien. Het zonlicht baant zich een weg door de mist die tussen de bomen aan de overkant van het meer hangt. Mist is een verzameling van heel veel kleine waterdruppeltjes, die ieder het licht van de zon verstrooien. Met verstrooien wordt bedoeld dat een deel van het licht dat bij het druppeltje aankomt wordt weerkaatst of afgebogen in een willekeurige richting. Als de mist maar dik genoeg is, dan wordt het licht meerdere keren achter elkaar verstrooid alvorens het ons oog bereikt. Dit wordt meervoudige verstrooiing genoemd, en heeft als resultaat dat het zonlicht *diffuus*, zonder voorkeursrichting, uit de wolk komt. Licht in mist is een goed voorbeeld van "licht in complexe diëlectrica", het onderwerp van dit proefschrift.

Een diëlectricum bestaat uit atomen en/of moleculen en is meestal transparant, oftewel het absorbeert geen licht. De snelheid waarmee het licht door zo'n diëlectrisch medium reist is lager dan in vacuum, daar waar geen atomen zijn. Deze vertraging van het licht wordt beschreven door de *brekingsindex*, die de verhouding van de lichtsnelheid in vacuum ten opzichte van die snelheid in het medium aangeeft. Verschillende diëlectrica kunnen verschillende brekingsindices hebben, afhankelijk van het type atomen (moleculen) waaruit ze bestaan en hun dichtheid. De atomaire oorsprong van de brekingsindex wordt nader toegelicht in hoofdstuk 2.

Met complex wordt bedoeld samengesteld, omvattend. Dat wil zeggen dat een complex diëlectricum is samengesteld uit twee of meerdere diëlectrica. De mistbank is daarvan een voorbeeld, bestaande uit de diëlectrica lucht en water, waarvan de brekingsindices verschillend zijn. Juist dit verschil in brekingsindex zorgt ervoor dat licht verstooid wordt in mist.

In dit proefschrift worden twee onderwerpen die te maken hebben met het gedrag van licht in complexe diëlectrica behandeld: verandering van spontane emissie en Anderson localisatie van licht.

Wat is spontane emissie? Atomen en moleculen kunnen licht absorberen. Ze slaan dan tijdelijk energie uit het lichtveld op om die eventueel later weer in de vorm van licht uit te zenden. Hoe lang het duurt voordat het atoom zijn teveel aan energie weer uitzendt berust op toeval en gebeurt spontaan. Dit verschijnsel wordt dan ook spontane emissie genoemd. Wel is het zo dat ieder atoom zijn eigen karakteristieken heeft. Dit houdt in dat zowel de kleur, oftewel de golflengte, van het spontaan geëmitteerde licht hoort bij het soort atoom, alsook de *gemiddelde* tijd die het duurt tussen het tijdstip van absorptie en emissie. Deze gemiddelde tijd noemt

men de spontane emissie levensduur en kan variëren van zo'n één-miljardste seconde (1 nanoseconde) tot wel enkele minuten. Zoals gezegd is deze levensduur karakteristiek voor een atoom, maar dat wil niet zeggen dat deze niet beïnvloed kan worden. Bijvoorbeeld de levensduur van hetzelfde molecuul in vacuum of in een diëlectricum is al verschillend. De verandering van de spontane emissie levensduur van een atoom in een diëlectricum met gegeven brekingsindex wordt voorspeld door de theorie beschreven in hoofdstuk 3.

De experimenten om deze theorie te toetsen worden uiteen gezet in de hoofdstukken 4 en 5. Een probleem in dit soort experimenten is dat wanneer het atoom energie van het lichtveld heeft geabsorbeerd, het niet altijd zo is dat deze energie ook weer als licht uitgezonden wordt. Het is ook mogelijk dat de opgeslagen energie wordt omgezet in warmte, hetgeen de vergelijking van experiment en theorie een stuk lastiger maakt. Het is dus zaak een combinatie van stralend atoom en diëlectricum te vinden waarin al het geabsorbeerde licht ook weer uitgezonden wordt. In de metingen beschreven in hoofdstuk 4 is het stralend atoom europium en het diëlectrische medium een serie van verschillende soorten alcoholen met variërende brekingsindex. Europium wordt veel gebruikt in tv's en tl-buizen voor het rode licht dat het uitzendt. In dit experiment is het europium atoom ingepakt in een kleine, moleculaire kooi. Dit heet een europium complex. De kooi moet het europium atoom beschermen tegen ongewenste invloeden van het diëlectricum. Het blijkt dat de spontane emissie levensduur van dit europium complex in alcohol niet alleen afhangt van de brekingsindex, maar dat het type alcohol toch ook een rol speelt. Een vergelijking van experiment en theorie was dan ook niet haalbaar. Het was dus nodig een nieuwe methode te bedenken waarmee het mogelijk is de brekingsindex van het diëlectricum te veranderen zonder dat het type molecuul waaruit het diëlectricum bestaat verandert. Het resulteerde in de keuze voor hetzelfde europium complex in nu een dicht gas van koolstof dioxide (CO_2) moleculen als diëlectricum, onder variërende druk. Bij hogere druk is de dichtheid van de CO_2 moleculen hoger en dus ook de brekingsindex, terwijl het soort molecuul onveranderd blijft. De typische stralende levenduur van europium is rond éénduizendste van een seconde (1 milliseconde), en bleek korter te worden naarmate de brekingsindex van het omringende dichte CO_2 gas groter werd. Deze keer kon de vergelijking van experiment en theorie wel gemaakt worden: de spontane emissie levensduur van een atoom in een diëlectricum wordt uitstekend beschreven door de theorie van hoofdstuk 3.

Het tweede deel van het proefschrift gaat over de voorplanting van licht in zeer sterk verstrooiende materialen. De verstrooiingsterkte wordt gekarakteriseerd door de *verstrooiings vrije weglengte*. Deze geeft de gemiddelde afstand aan die het licht aflegt tussen twee verstrooiingen in. In een mistbank zoals te zien op de omslag is

die afstand zo'n tiental meters. Maar wat gebeurt er als het complexe diëlectricum zo sterk strooit dat de verstrooiings vrije weglengte ongeveer één-miljoenste meter (1 micrometer) is, vergelijkbaar met de golflengte van zichtbaar licht? Aan het eind van de vijftiger jaren heeft P.W. Anderson al voorspeld dat golven, en dus ook licht, in een zo'n sterk verstrooiend medium opgesloten worden. Dit verschijnsel noemt men dan ook Anderson localisatie. In deze nieuwe toestand kan licht niet meer voortplanten, hetgeen uit fundamenteel oogpunt zeer interessant is voor natuurkundigen. Maar het bereiken van deze toestand is niet eenvoudig, want het sterk verstrooiende materiaal mag het licht niet absorberen. Wanneer een mengsel van twee transparante diëlectrica zodanig gestructureerd is dat de brekingsindex willekeurig varieert op lengteschalen die vergelijkbaar zijn met de golflengte van het licht, dan strooit dit mengsel het sterkst. Maar om zéér sterke verstrooiing te verkrijgen moet de variatie in de brekingsindex ook nog groot zijn.

In hoofdstuk 6 worden de optische eigenschappen beschreven van een nieuw soort zeer sterk licht verstrooiend materiaal: poreus galliumfosfide (GaP). Dit materiaal is een wanordelijke spons van luchtporiën in GaP; de poriën hebben een afmeting van zo'n 0,15 micrometer, vergelijkbaar met de golflengte van zichtbaar licht. Het is gemaakt via een nieuwe electrochemische etsmethode. GaP heeft een hoge brekingsindex (3,3) en is transparant voor rood licht. Poreus GaP is dan ook het sterkst verstrooiende materiaal voor zichtbaar licht tot nu toe. Het voordeel van een poreus materiaal is dat dit zich, zoals een spons, laat volzuigen met een vloeistof. Deze eigenschap wordt gebruikt om het belang van de grootte van de variatie van de brekingsindex voor de sterkte van verstrooiing aan te tonen. De optische eigenschappen van met vloeistof gevuld poreus GaP zijn anders dan wanneer het materiaal met lucht is gevuld, omdat de variatie in de brekingsindex door de vloeistof wordt verlaagd. Het gevolg is dat het materiaal minder efficiënt licht verstrooit. De invloed van de variatie in de brekingsindex op de sterkte van verstrooiing blijkt veel groter te zijn dan tot nu toe aan de hand van theorieën werd aangenomen. De metingen aan licht dat door het poreuze materiaal is heen gekomen, vertonen geen kenmerken van Anderson localisatie, maar laten wel zien dat deze materialen zeer sterk verstrooien. De verstrooiings vrije weglengte is in poreus GaP minder dan 0,2 micrometer.

In plaats van naar het licht te kijken dat zich een weg door het verstrooiende materiaal heeft heen gebaand (transmissie), is het ook mogelijk metingen te doen aan het licht dat juist terug verstrooid wordt (reflectie). Zeer preciese metingen, zoals die beschreven staan in hoofdstuk 7, van de gereflecteerde licht intensiteit voor veschillende richtingen ten op zichte van het inkomende licht bundel geven aanvullende informatie over de verstrooiings eigenschappen. Deze metingen bevestigen dat poreus GaP zeer sterk licht verstrooit, en wijzen bovendien in de richting van Anderson localisatie van zichtbaar licht.

DANKWOORD

Op de voorkant van dit proefschrift staat slechts één naam. Er zijn echter velen die hebben bijgedragen aan de totstandkoming ervan. Hierbij wil ik deze mensen dan ook graag bedanken.

Allereerst noem ik mijn promoter Ad Lagendijk voor zijn aanstekelijke enthousiasme en de vrijheid die hij me gaf bij de keuze van mijn onderzoeksonderwerpen. Maar misschien wel de belangrijkste bijdrage was zijn sturen van mijn onderzoek op meta-niveau. Rudolf Sprik vormde in de afgelopen jaren een fantastische vraagbaak, die waarschijnlijk antwoord had op al mijn vragen. Gerard Wegdam wil ik bedanken voor zijn originele idee een superkritisch gas te gebruiken als diëlectricum (zie hoodfstuk 5), alsook voor de gezamenlijke discussies over (groeps)sociologie. Voor dit laatste moet Pedro de Vries ook genoemd worden, maar daarnaast ook voor zijn essentiële bijdrage aan hoofdstukken 2 en 3. Mijn "eeuwige" kamergenoot Willem Vos bedank ik onder andere voor die ene fantastische dag in Santa Barbara.

Het deel van dit proefschrift dat over poreus GaP gaat, steunt in belangrijke mate op de samenwerking met de electrochemici uit Utrecht. Daniël Vanmaekelbergh wil ik bedanken voor het hoge tempo waarmee hij nieuwe, leuke ideeën aanvoerde en de daarop volgende, soms onnavolgbare discussies. Jao van de Lagemaat moet zeker genoemd worden voor het vakkundig introduceren van een onbekende in de wereld van electrochemische experimenteren. Petra de Jongh wordt nogmaals bedankt voor het maken van de mooie SEM-plaatjes. En John Kelly zorgde voor het goede klimaat waarin de samenwerking met zijn groep uiteindelijk succesvol werd.

De discussies over stralende levensduren van zeldzame aarden, in het bijzonder europium, die ik samen met Andries Meijerink had, waren zeer waardevol. Ook bedank ik Andries voor ons probeersel om gadolinium luminescentie te meten in verschillende alcoholen.

Diederik Wiersma wil ik bedanken voor de discussie over localisatie, absorptie, halfgeleider poeders, en het malen daarvan.

Hans Regeer wil ik graag noemen voor de goede zorgen voor de lasers, maar ook voor de gesprekken over schaatsen, zweefvliegen, ...

Huib Luigjes en Klaas Prins hebben zeer veel bijgedragen door in eerste instantie hun gascompressor uit te lenen en ons (Dennis en ik) van de daarbij behorende instructies te voorzien, en in tweede instantie voor het kado geven van diezelfde compressor.

Dan zijn we aangekomen bij de technici van zowel de mechanische als electronische werkplaatsen, die absoluut zeer essentieel zijn voor ieder experimenteel onderzoek, zo ook dat van mij. Ik wil graag al diegenen bedanken die mij, meestal ook nog zeer snel, aan allerlei onderdelen hebben geholpen. In het bijzonder noem ik Johan Soede met wie ik het genoegen heb gehad om met drie man (Johan, Dennis en ik) en veel geweld de kop van de gascompressor los te draaien, gebruik makend van zo'n drie meter lange sleutel om maar genoeg hefboom te hebben. Ook de andere Johan, Johan van de Ridder, dient genoemd geworden voor de altijd aanwezige grote glimlach op zijn gezicht en het maken van een fantastische schaatse sliep (samen met Wim).

Bert Zwart en Eddy Inoeng van de glasblazerij stonden altijd klaar om nieuwe ampullen af te pompen en dicht te smelten, als ik weer eens snel tussendoor iets geregeld wilde hebben. Bedankt daarvoor.

Ina Zwart en Ineke Baay wil ik graag bedanken voor de talrijke kleine en minder kleine administratieve klussen die zij voor mij verricht hebben, zodat ik verder kon met de leukere dingen.

Wim Koops is een verhaal apart. Zeer belangrijk was zijn technische ondersteuning, maar misschien nog wel belangrijker was de mens Wim. Verder wil ik Wim ook nog bedanken voor het maken van de al eerder genoemde schaatse sliep, voor de cursus schaatsslijpen, en die ene leuke schaatstocht (samen met Mark).

Die enige student die ik heb mogen begeleiden, Dennis de Lang, wil ik bedanken omdat hij misschien wel heeft gezorgd voor de implus die mijn onderzoek nodig had, door in z'n uppie vele dagen in donkere kelder hele mooie metingen bij elkaar te vergaren.

Alle groepsleden, alsook de waterstof-boys, wil ik bedanken voor de fantastische sfeer die zij creëerde. Ik denk met veel plezier terug aan onze uitjes, discussies, plagerijen en de fameuze Mischa's-"vijf-minuten"-experimentjes. Anouk, Judith, Lydia, Allard, Arnout, Bert, Boris, Carlos, Denis, Dirk, Femius, Frank, Gijs, Henry (Hendrik), Henry (Henk), Jaime, Johannes, Makoto, Mark, Mark, Martijn, Matthias, Meritt, Michiel, Mischa, Pepijn, Peter, Rik en Tom, allen bedankt!

Mijn ouders en "schoon" ouders, bedankt voor de goede zorgen die jullie voor Marjolein en mij hebben gehad. Marjolein, wat ik hier ook schrijf, het komt in geen geval in de buurt bij wat ik voor je voel. Ik weet nu dat we het halen, allebei een boekje. Ga je mee op vakantie?

Frank